



VCU

Virginia Commonwealth University
VCU Scholars Compass

Theses and Dissertations

Graduate School

2018

Use of Surface Enhanced Raman Spectroscopy for the Detection of Bioactive Lipids

Christopher M. Ohlhaber

Follow this and additional works at: <https://scholarscompass.vcu.edu/etd>



Part of the [Materials Chemistry Commons](#)

© The Author

Downloaded from

<https://scholarscompass.vcu.edu/etd/5551>

This Thesis is brought to you for free and open access by the Graduate School at VCU Scholars Compass. It has been accepted for inclusion in Theses and Dissertations by an authorized administrator of VCU Scholars Compass. For more information, please contact libcompass@vcu.edu.

Use of Surface Enhanced Raman Spectroscopy for the Detection of Bioactive Lipids

A thesis submitted in partial fulfillment of the requirements for the degree of Master of Science
in Chemistry at Virginia Commonwealth University.

By

Christopher Michael Ohlhaber

B.S. Chemistry, College of William and Mary, January 2017

Advisor: Indika U. Arachchige, PhD.

Director of Graduate Recruitment and Associate Professor

Department of Chemistry

Virginia Commonwealth University

Richmond, Virginia

June, 2018

Acknowledgement

I would like to take this opportunity to thank all the inspirations in my life and toward my research. First, as a “good little Catholic boy” I would like to thank God, the Father almighty for making the heavens and, for the sake of science, the earths which we study. I would also like to thank my advisors over the years. Of course, my mother for giving birth to me and giving me half of her DNA and my father for providing the other half of my genetic code. Poor folks, having to raise a little terror like me! My brother taught me perseverance by holding me down as a kid and making me work to break free of his grip while he was a far larger individual than myself when he was being a bully, so I guess I should thank him for teaching the stubborn perseverance that was needed to get anywhere on a project where all my collaborators were rather pessimistic from the get go. I would also like to thank Erwin Rudolf Josef Alexander Schrödinger and his adorable little kitty cat for showing the importance of analogies and sleep deprivation in science. I feel compelled to thank the authors of the Heisenberg Dog paper, who should be commended for introducing me to innuendos in hard sciences.¹ I am obligated to thank my wonderful girlfriend as well for making faces at me while I was writing this document and keeping me from losing my mind while I do something that I am only looking at as a check in the box, seeing as it keeps me from doing real science. Besides, my data is being published in a real journal article, so who cares if this thesis gets published since no one is likely to read it after I get my degree. Honestly, no one other than my advisor is likely to read it even before then. Anyways, she kept me from getting stressed out while simultaneously I had four professors squabbling who would turn to me and yell “publish.” Her support has made this a much more enjoyable experience. Lastly, I would like to thank Chris Ferrie, author of Goodnight Lab, for his example on entertaining scientific writing. If you are still reading this, quit wasting your time and get to my data! Go on. Time to look at the real data, not just the mildly amusing anecdotal waste of time before the science. This section is only here as a formality and to see who (if anyone) on my thesis committee is thoroughly reading this document. If you did read this, kudos to you. If not, no hard feelings, I am obviously not upset seeing as I have already expressed my disdain for writing a thesis on data already published in a journal that will be much more accessible, so use your time more wisely than perusing my data in a less pretty format than the wonderful people at ACS Applied Nanomaterials already did.

Table of Contents

i.	Title Page	i.
ii.	Acknowledgements	ii.
iii.	Table of Contents	iii.
iv.	List of Abbreviations and Symbols	iv.
v.	List of Figures, Schemes and Tables	vi.
vi.	Abstract	ix.
1.	Chapter 1: Introduction	1.
	1.1 Nanomaterials	2.
	1.2 Band Gaps	4.
	1.3 Nanoparticles in Medicine	6.
	1.4 Non-medical Nanoparticle Applications	9.
	1.5 Surface Enhanced Raman Spectroscopy	10.
	1.6 Hypertension, Preeclampsia and Lipids	12.
	1.7 Challenges of Surface Enhanced Raman Spectroscopy	16.
	1.8 Current Detection Methods	19.
	1.9 Surface Enhanced Raman Spectroscopy Substrates	23.
	1.10 Thesis Statement	25.
2.	Chapter 2: Experiment Section	28.
	2.1 Raman Spectroscopy and Surface Enhanced Raman Spectroscopy	28.
	2.2 Ultraviolet-Visible-Near Infrared Spectroscopy	32.
	2.3 Nanoscale Imaging and Microscopy	33.
3.	Chapter 3: Initial Studies- Thiols, Thromboxane and Prostaglandin	36.

3.1 Substrate and Acquisition Parameters	36.
3.2 Materials	38.
3.3 Synthesis of Octanethiol-Functionalized Au Nanoparticle Thin Films	39.
3.4 Substrate Durability Testing	41.
3.5 Acquisition parameters of Raman and SERS Spectra of Lipids	42.
3.6 Spherical Silver Nanoparticle as SERS Substrates Outcomes	42.
3.7 Citrate-Coated Silver Platelets as SERS Substrates	46.
3.8 Peak Assignment and Lipid Stability	51.
4. Excerpt from Submitted Manuscript and Nanoplatelet Data	53.
4.1 Experimental Section	53.
4.1.1 Materials	53.
4.1.2 Synthesis of Citrate-Capped Ag Nanoplatelets	53.
4.1.3 Fabrication of SERS Substrates.	54.
4.1.4 Physical Characterization of Ag Nanoplatelets and SERS Data Collection	54.
4.1.5 SERS and Raman Data Collection.	55
4.2 Results and Discussion	56.
4.2.1 SERS Substrate Design and Thin Film Fabrication	56.
4.2.2 Pure Lipid Spectra of 20-HETE, AA, EPA, and DHA.	63.
5. Conclusions	76.
6. References	79.
7. Biosketch	107.

List of Abbreviations and Symbols

Abbreviation/symbol	Meaning
°C	Degrees Centigrade
μL	Microliter
μM	Micromolar
μM	Micrometer
20-HETE	20-Hydroxyeicosatetraenoic acid
6-keto	6-keto prostaglandin f _{1α}
AA	Arachidonic Acid
ACS	American Chemical Society
Ag	Silver
AgNO₃	Silver Nitrate
Al	Aluminum
Au	Gold
cm	Centimeter
COO	Carboxylate
COOH	Carboxylic Acid
cryo-STEM	Cryogenic Scanning Transmission Electron Microscopy
Cu	Copper
CYP450	Cytochrome P450
CYP4A11	Cytochrome P450 4A11

CYP4F2

Leukotriene-B(4) Omega-Hydroxylase 1 Enzyme

DC	Direct Current
DHA	Docosahexaenoic Acid
DHHS	US Department of Health and Human Services
DNA	Deoxyribonucleic Acid
EETs	Epoxyeicosatrienoic Acids
EMR	Electromagnetic Radiation
EPA	Eicosapentaenoic Acid
Et al.	Et alla (plurality of other authors)
eV	Electron Volts
GSH	Glutathione
h	Hour(s)
HAuCl₄	Chloroauric Acid
Hg	Mercury
HOMOs	Highest Occupied Molecular Orbitals
IR	Infrared/ Infrared Spectroscopy
LC	Liquid Chromatography
LSPR	Localized Surface Plasmon Resonance
LOD	Lowest Limit of Detection
LUMOs	Lowest Unoccupied Molecular Orbitals
min	Minute(s)
mL	Milliliter
mL	Milliliter

mM	Millimolar
mm	Millimeter
MS	Mass Spectrometry
MW	Molecular Weight
Na	Sodium
NaBH₄	Sodium Borohydride
NCC	Nano Characterization Core
ng	Nanogram
NIH	National Institute of Health
NIR	Near-infrared
nm	Nanometer
nM	Nanomolar
NMR	Nuclear Magnetic Resonance
NO₃	Nitrate
NP	Nanoparticle
NPs	Nanoparticles
OH	Hydroxyl group
pM	Picomolar
PSS	Poly(styrenesulfonate)
RF	Radio Frequency
SA	Surface Area
SE-HPLC	Size Exclusion High Performance Liquid Chromatography
SEM	Scanning Electron Microscope/ Microscopy

SERS	Surface Enhanced Raman Spectroscopy
STDs	Sexually Transmitted Diseases
TEM	Transmission Electron Microscope/ Microscopy
TXB2	Thromboxane B2
UV	Ultraviolet
UV-Vis	Ultraviolet-Visible-Near Infrared Absorption Spectroscopy
V	Volume
VCU	Virginia Commonwealth University
μW	Microwatt
Zn	Zinc
Ω	Ohm

List of Figures

Figure Number	Description	Page Number
Figure 1.1	Demonstration of surface area to volume ratio effects	2
Figure 1.2	Bandgaps and size effects of quantum dots	4
Figure 1.3	Direct and Indirect Bandgaps	6
Figure 1.4	Valence and Conduction Bands of Insulators, Semiconductors and Conductors	7
Figure 1.5	Diagram of Thermo-therapeutic Nanoparticles	8
Figure 1.6	Diagram Comparing Size of Nanoparticles and Visible Light	10
Figure 1.7	Diagram of Localized Surface Plasmon Resonance	11
Figure 1.8	Structure of the Lipid 20-Hydroxyeicosatetraenoic Acid	13
Figure 1.9	Structure of the Lipid 6-keto prostaglandin $f_{1\alpha}$	14
Table 1.1	Table of Laser Dissociation and Bond Energies	18
Figure 1.10	Illustration of Orientation of Analytes in SERS	18
Figure 1.11	Micelle of Arachidonic Acid	29
Figure 1.12	Block Diagram of LC-MS	21
Figure 1.13	Comparison of Au NP vs Ag Nanoplatelet Enhancement	24
Figure 2.1	Diagram of Raman Spectrometer Instrumentation	29
Figure 2.2	Diagram of an Energy Well	30
Figure 2.3	Diagram of Localized Surface Plasmon Resonance	31
Figure 2.3	Diagram of UV-Vis Instrumentation	32
Table 2.1	Table of De Broglie Wavelengths of Electron Beams	34
Figure 3.1	Diagram of the Tunable Plasmon Frequencies of Au and Ag and Laser Wavelengths Available	37
Figure 3.2	Physical Characterization of Au NPs	38
Scheme 3.1	Synthetic Scheme of Au NPs	39
Figure 3.3	Burning Study of Platelet Substrate	41
Figure 3.4	SERS Spectra of 6-Keto on Au NPs	44
Figure 3.5	SERS Spectra of TXB2 on Au NPs	45
Figure 3.6	SERS Spectra of 6-Keto on Ag Nanoplatelets	46
Figure 3.7	SERS Spectra of TXB2 on Ag Nanoplatelets	48
Figure 3.8	SERS Spectra of 20-HETE on Ag Nanoplatelets	49
Figure 3.9	Burning Study of 20-HETE on Ag Nanoplatelets	51
Scheme 4.1	Scheme of Ag Nanoplatelet Synthesis and SERS	56
Figure 4.1	Raman Spectrum of Substrate	59
Figure 4.2	SEM Image	60
Figure 4.3	Photographs of Substrate Slides	60
Figure 4.4	Physical Characterization of Substrate	61
Figure 4.5	TEM images of Nanoplatelets	62
Figure 4.6	Raman Spectra of Lipids	65
Table 4.1	Prominent Peaks of Raman Spectra	66

Table 4.2	Quantitative Analysis of Peaks	69
Figure 4.7	SERS Spectra of Lipids	70
Figure 4.8	20-HETE and AA Mixing Study Spectra	72
Figure 4.9	20-HETE and DHA Mixing Study Spectra	73
Figure 4.10	20-HETE and EPA Mixing Study Spectra	74
Figure 4.11	Mixing Study of “Synthetic Plasma”	75

Abstract

The detection and analysis of lipids in biological matrices for clinical applications poses many challenges, but rapid and reliable detection will prove invaluable for clinical diagnosis. Herein, we report the application of drop-casted Ag nanoplatelets as surface enhanced Raman scattering (SERS) substrates for qualitative detection of 20-hydroxyeicosatetraenoic acid (20-HETE), which is a potential biomarker for diagnosis of hypertensive disorders. Biomarker peaks of 20-HETE can be reliably detected and differentiated from those of the structurally similar lipids (arachidonic acid, eicosapentaenoic acid, and docosahexaenoic acid) commonly found in human blood, even 1 pM concentrations. Additionally, one study mixed 20-HETE with three structurally similar lipids at concentrations several orders of magnitude greater than the target lipid and 20-HETE could still be detected under these conditions. These experiments demonstrate the viability of SERS for the rapid and reliable detection of endogenous bioactive lipids, which has significant clinical impact in enabling point of care diagnostics.

Key Words: 20-HETE, SERS, lipid, detection, Raman, silver, nanoplatelet, enhancement

Chapter 1: Introduction

Nanomaterials have gained increasing interest over the last two decades, since they were mentioned by President Bill Clinton in 2000 at an address on scientific policy at Caltech.² At the time, it was fascinating to the non-science community that such small materials could be made and worked with, even if they could not fully comprehend the size of the particles nor the magnitude of the effects that they would have in everyday life. Nanomaterials quickly became an important asset in consumer electronics, energy generation, storage and delivery, medicine and industry. The interest in these materials are derived from the unique properties that they exhibit. Materials from 1-100 nanometers are classified as nanomaterials.³ This small, but highly varied class of materials includes semiconductors, sensors, biomaterials, catalysts and magnetic nanoparticles (NPs). Small variations in the size, morphology and composition can make immense differences in the characteristics of these particles.⁴

1.1 Nanomaterials

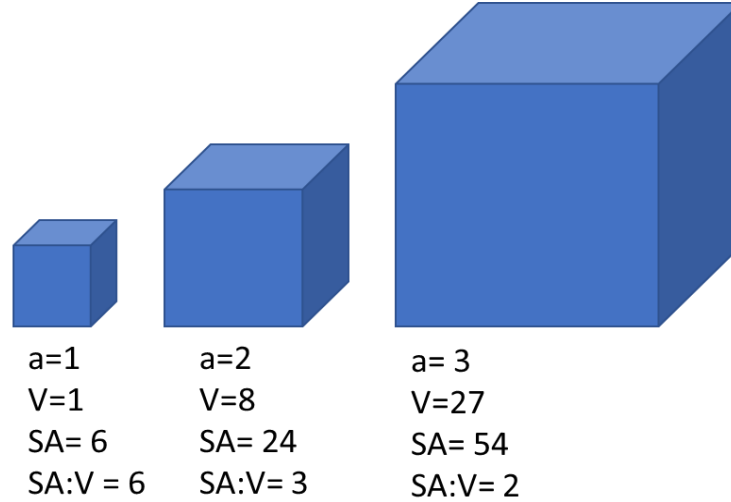


Figure 1.1 Demonstration of surface area to volume ratio effects, where a = edge length, V = volume and SA = surface area. As the volume of a regular three dimensional shape increases, the surface area to volume ratio decreases.

The phrase “bigger is better” is used quite often, however it does not always hold true with materials. NPs derive many of their unique physical and chemical properties from size related effects. NPs have inherently high surface area to volume ratios.⁴⁻⁶ Most reactions occur at the surface of a material, leading the increased surface of nanostructures to improve catalytic activity.^{7,8} The surface atoms are more strained than core atoms in a nanomaterial, which leads to lower melting points for smaller nanoparticles.^{9,10} This high surface strain also leads to the tendency of nanoparticles to aggregate, leading to many nanoparticles created by chemical methods having capping agents to stabilize the particles.^{11,12} Many other interesting properties of nanotechnology are derived from quantum physics. NPs are small enough that some Newtonian physics does not apply, and instead quantum mechanical properties are observed.^{13,14} One of the most important quantum properties seen in nanoscience is quantum

confinement. When a particle is smaller than the bohr radius of the material it is made of, it is said to be quantum confined.¹⁵⁻¹⁷ A quantum confined particle will have a large bandgap than the bulk material.^{18,19} The energy of the bandgap will be size dependant, leading to the development of quantum dots, luminescent quantum confined NPs that are more efficient than their bulk counterparts at light absorption and emission.¹⁸⁻²⁰ This efficiency is derived from an effect known as quantum confinement. When the Bohr radius of a particle is smaller than the exciton of the material it is made from, the energetics of the particle are changed,^{15,17} The system is considered quantum confined when the particle is below the de Broglie wavelength of an electron (also referred to as the exciton Bohr radius) for that material, making its excitations more energetically demanding than a bulk material, or even non-quantum confined nanoparticles.^{21,22} Below the excitation Bohr radius, the emission of a particle will blueshift because the discrete energy levels will be further separated

Taking into account the three dimensional particle in a box model, one can begin to further understand the quantum confinement effect.^{23,24} As the volume of a spherical particle, approximated as a three dimensional potential well, is squeezed to a smaller radius, it increases the energy of the system, as represented by the equation:

$$E_{n_x, n_y, n_z} = \frac{\hbar^2 \pi^2}{2m} \left[\left(\frac{n_x}{L_x} \right)^2 + \left(\frac{n_y}{L_y} \right)^2 + \left(\frac{n_z}{L_z} \right)^2 \right]^{25}$$

Nanospheres have three dimensions of confinement while nanowires and nanorods with the longitudinal radius below the de Broglie wavelength have two dimensions of excitation.²⁶⁻²⁸ As the radius of any of these dimensions is decreased, the denominator of one of the terms on the right side of the equation will be decreased, increasing the energy of the excitation. This principle dictates why quantum dots are desirable for solar cell applications, in which a more energetic absorption and emission will often shift the wavelength into regions of the

electromagnetic spectrum that are more intensely emitted by the sun, further increasing the energetic efficiency of these particles.²⁸⁻³²

1.2 Bandgaps

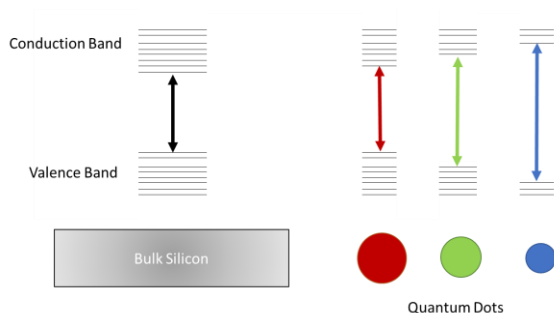


Figure 1.2 Band gap effects of quantum dots, where the blue quantum dot is quantum confined, resulting in the largest tuned bandgap. As particles decrease in size, the band gap increases. There is a large bandgap increase when a particle is quantum confined by the particle's radius becoming smaller than the Bohr radius of that material, as represented by the large band gap increase between the green and blue quantum dots above.

The properties of NPs are largely dependent on the elements that they are composed of. The element will not only determine the Bohr radius of the nanoparticles, but will also determine the electrical properties of the particles.^{18,30,33} There are three electrically relevant classifications for materials: conductors, semiconductors and insulators.³⁴ These classifications are determined by the bandgap of the material, or amount of energy that is required to excite an electron from the valence band to the conduction band.^{35,36} The valence band is formed by the overlay of the discrete highest occupied molecular orbitals (HOMOs) of the material while the conduction band is formed by the overlap of the lowest unoccupied molecular orbitals (LUMOs).^{13,32,37} This bandgap will determine characteristic properties of a material, such as the electrical resistance and emission wavelength of the particles.³⁸ Insulators have a bandgap

greater than 4 eV, semiconductors have between a 0.5 and 4 eV bandgap and conductors have less than a 0.5 eV bandgap.^{32,39} In a conductor, the valence band and conduction band overlap, allowing the electrons to freely flow from one band to the other, resulting in low electrical resistance and high conduction materials. Semiconductors can have two different transitions: direct and indirect band gaps.^{18,32,40,41} In a direct bandgap semiconductor, both the momenta of the lowest energy position in the conduction band and highest energy section of the valence band align, allowing for facile transitions of electrons when they are exposed to photons of the proper energy.^{18,32,40,41} Indirect bandgap materials require the momentum of the electron to change in going from the valence to the conduction band because the local extrema are not in the same momentum.⁴²⁻⁴⁵ This process requires both an excitation photon and a photon to change the momentum of the electron in order for an electron to move from one band to the other.⁴²⁻⁴⁵ Because of the requirement for this second photon, indirect bandgap semiconductors are less efficient than direct bandgap semiconductors.^{45,46}

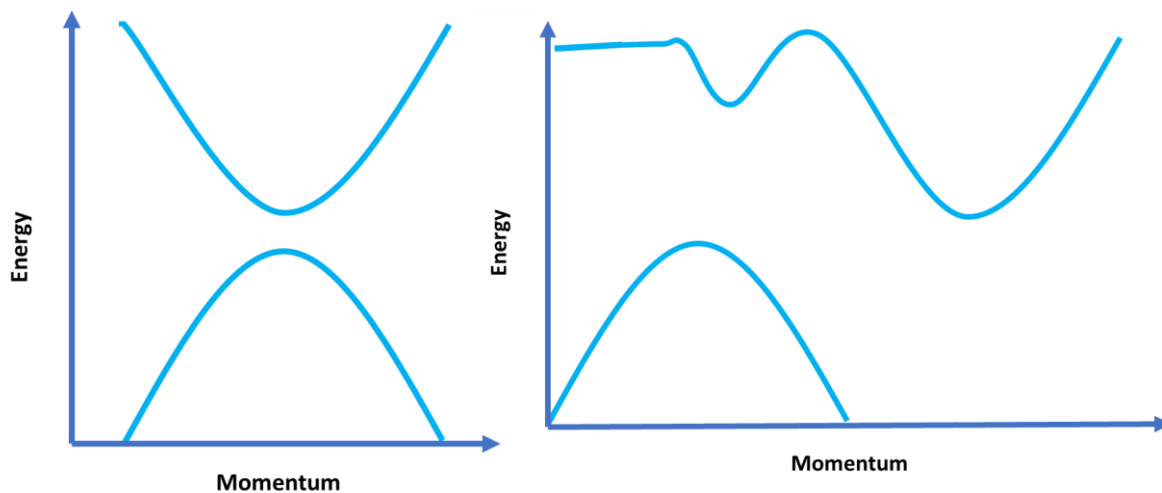


Figure 1.3 Direct (left) and Indirect (right) bandgaps. In a direct bandgap, the smallest energy difference between the valence and conduction bands is in the same momentum. In an indirect bandgap, the bandgap is the least energetically different at two different momenta, making electronic excitation less efficient due to the requirement for the momentum change.

1.3 Nanoparticles in Medicine

Medicine has taken interest in nanoparticles for several therapeutic mechanisms, including the use of magnetic NPs and thermotherapeutic particles.⁴⁷⁻⁴⁹ Magnetic NPs have been used in Germany for several experiments involving targeting specific regions of the body for drug delivery or thermotherapeutics.^{48,50-52} A properly engineered magnetic field can contain a large number of the particles to a particular region of the body, allowing for more localized therapy. If the NPs are used for drug delivery, they will be held to the region of the body until the drug has had enough time to be released.^{3,51} If it is instead used for thermotherapeutics, the particle

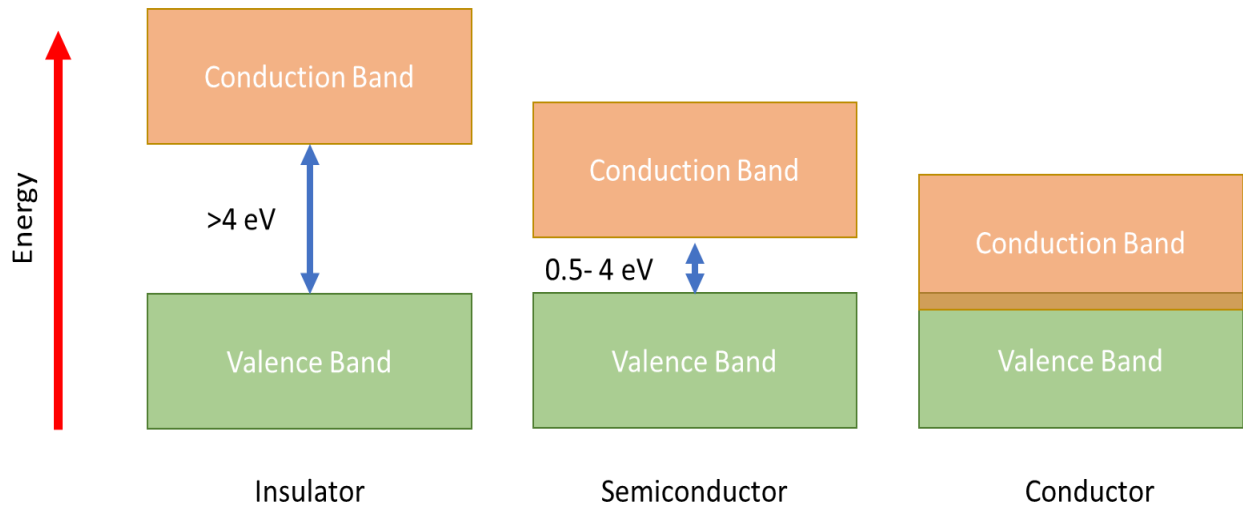


Figure 1.4 The band gaps of insulators (left), semiconductors (middle) and conductors (right) are displayed with a graphical representation of the valence and conduction bands. Insulators have a large band gap, reducing the probability of transitions from the valence to the conduction band. Semiconductors have a smaller bandgap, making excitation more probable. The bands of a conductor overlap, causing a high probability of transition from the valence to the conduction band.

concentration will be increased within the field, increasing the effectiveness of the therapy. In thermotherapeutics, nanoparticles are designed to heat up after exposure to radiation of a wavelength that is not normally harmful to biological samples.^{47,49-51} By causing a localized heating of the afflicted cells through targeted exposure of radiation from a laser, the particles will be heated above 40° C and held long enough to kill the cells in that region.⁴⁸ This allows for a high degree of target discrimination within the desired region, giving rise to the ability to kill a tumor without harming the healthy cells surrounding it. These particles can be combined with

quantum dots for imaging and drug delivery NPs to further increase the power of NPs for cancer treatments.⁴⁸

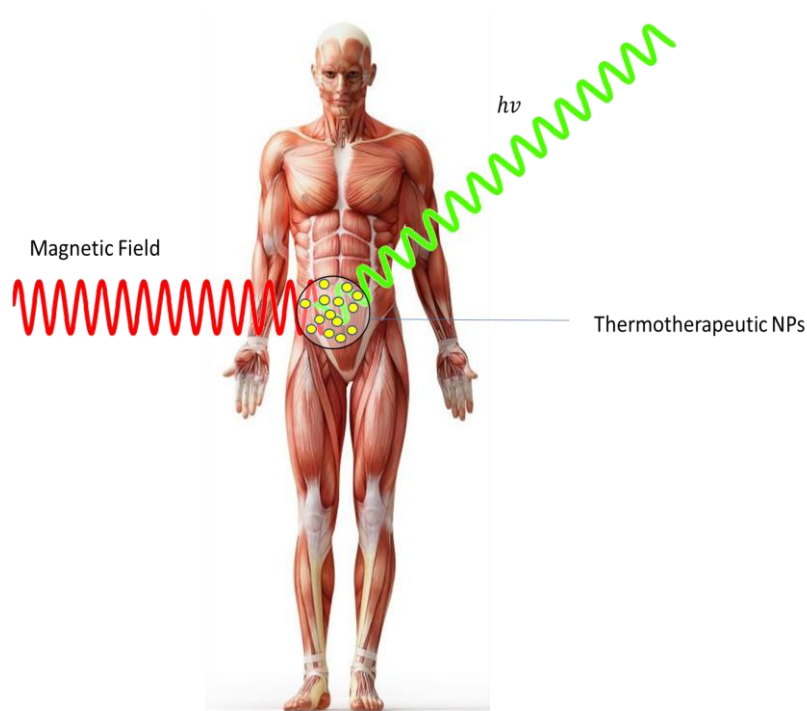


Figure 1.5 Magnetic thermotherapeutic nanoparticles being used for regionally selective cancer therapy. These NPs are designed to allow a magnetic field to hold the particles in place (magnetic) and can be heated up by exposure to an excitation source, such as an IR laser, creating an area specific cancer therapy.

As sensors, nanomaterials have become famous for their low limits of detection, specificity and biocompatibility.⁵³ The highly energetic surface of atoms of NPs make them more photoactive, increasing their detectibility.⁴⁹ This small size also allows greater motion of the particles. Diffusion rates in fluids are drag dependant, making a greater number of small particles more advantageous than a small number of large sensors.⁵⁴⁻⁵⁶ The increased surface

area also means a greater number of collisions between the sensor particles and potential analytes. This drastically decreases the lower limit of detection (LOD) of these materials, lending them to highly active imaging media.⁵⁵⁻⁵⁸ In more traditional sensors, nanowires allow for smaller devices to be made, giving rise to more specific detection, as well as the ability to link multiple sensors into a single device that is still small enough to detect biological activity without interfering in normal function.

1.4 Non-medical Nanoparticle Applications

Nanoparticle use is not limited to the nanoscale. In many new and investigational materials, nanoparticles are being incorporated into currently existing bulk materials to change their properties.³ Similarly to alloying or doping, adding a small amount of one material to a large amount of another can introduce characteristics of both materials.⁵⁹⁻⁶¹ Nanoparticles can be used to change the electrical conductivity, melting point, strength or reactivity of a material. Nanoparticles have also been used because of their optical properties for millennia, tracing roots back to ancient artwork where they were used as pigments.^{62,63} Famously, metal nanoparticles were used to make stained glass, which can be observed in decadent cathedrals throughout Europe.^{64,65} More recently, it has been discovered that nanoparticles interact with light by doing more than just absorbing and emitting wavelengths that are aesthetically pleasing. It has been discovered that the numerous light interactions of nanoparticles make them ideal for sensing applications.

1.5 Surface Enhanced Raman Spectroscopy



Figure 1.6 Size comparison of 532 nm light to 100 nm nanoparticle. Because the wavelength is greater than the size of the particle, that wavelength would not be able to be used for particle imaging. It can, however, impart energy on the particle, inducing effects such as LSPR.

The small size also changes the color of these particles. Since even at 100 nm, nanoparticles are smaller than the wavelength of the visible and UV spectrum, light interactions with nanoparticles do not produce the same visible color effects that bulk materials exhibit.^{3,52,66} Gold's signature color in the bulk is lost in the nanoscale, replaced by purple and red colored nanoparticles. This effect is due to the localized surface plasmon resonance (LSPR),⁶⁷ The LSPR is derived from an oscillation of the electron cloud of plasmonic metal nanoparticles that are being stimulated by light.⁶⁸ This oscillation of electrons creates an electric field, which will have a magnetic field that is orthogonal to it.⁶⁷⁻⁶⁹ The resultant fields of this plasmon oscillation can induce a surface enhancement effect in Raman Spectroscopy (discussed later in this chapter) by changing the polarizability of any analytes.^{8,54,70,71}

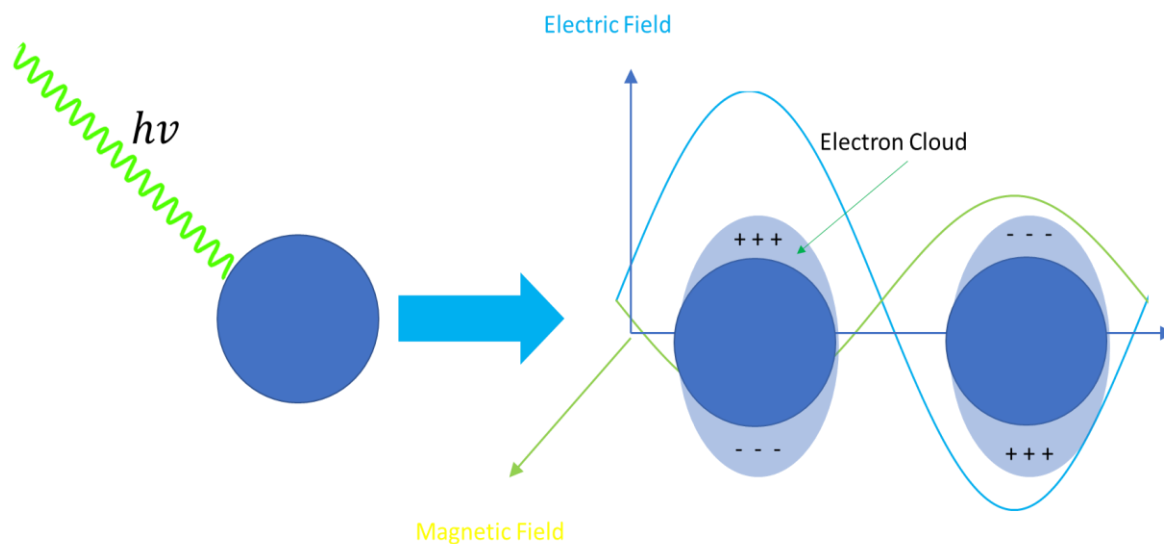


Figure 1.7 Simplified diagram of localized surface plasmon resonance. When excitation energy of the proper frequency (in this case, light) interacts with the nanoparticle, it causes oscillation of the electron cloud. Since the magnetic field is perpendicular to the electric field created by the oscillation, it causes the magnetic field to shift as well.

The study of interactions between electromagnetic radiation and matter, known as spectroscopy, has provided insight into chemical and physical properties of materials and systems for centuries. There are four common electromagnetic interactions with matter: reflection, transmission, absorption and scattering.⁷²⁻⁷⁸ In reflection, light bounces from a surface without changing the wavelength.⁷⁶⁻⁸¹ Some of the energy of the incident light is lost to inelastically if the reflectance of the surface is less than absolute, which can be approached but has not been reached.^{79,81} Diffuse reflection spectroscopy can be used to learn what wavelengths a solid absorbs by seeing which wavelengths are reflected, and therefore not observed. Absorption is the transfer of energy of a photon to become internal energy of the absorber.^{76,77}

Absorption, such as UV-visible absorption spectroscopy can be used to determine the concentration of solutions, observe charge transfer effects and observe organic reactions, which will change absorption based on changes in pH, conjugation of the system and solution polarity.^{20,74,82,83} Transmission is the ability of a wavelength to pass through an object or solution without being absorbed.^{78,84-87} It is typically coupled with absorption spectroscopy techniques as a complementary mode, representing similar data in an inverse manner, showing high intensity in transmission mode where low intensity is shown in absorption mode.⁸⁸ Scattering involves the deviation of the emission from the straight-line trajectory that it was initially on, causing bending of the light.^{26,70,73,74,78,89} Some modes of scattering change the wavelength of the light while others do not. A common spectroscopy technique based around measuring scattering is Raman Spectroscopy. Numerous SERS studies can be found showing increased sensitivity using rhodamine as an analyte, however practical applications of this technology are still few and far between.^{54,71,90-93} Though some studies have been done with DNA, showing the viability of using SERS to detect complex biomolecules, no known studies have successfully used SERS for medical diagnosis.^{33,38-42} Several review papers from 2005 onward projected that SERS would be usable for clinical diagnosis, but no known studies have been reported hitherto.⁴³⁻⁴⁶ Lipid studies have been done with Raman and SERS imaging, however it has not been used as a point of care device for diagnosis.

1.6 Hypertension, Preeclampsia and Lipids

One medical condition that would be hypothetically easy to detect with SERS would be hypertension. Several lipid metabolites are linked closely to hypertensive disorders by inducing vasoconstriction.¹⁰²⁻¹⁰⁵ Specifically, the cytochrome P450 facilitated arachidonic acid cascade has been shown to induce hypertension through the creation of epoxyeicosatrienoic acids (EETs)

and their counterparts, the hydroxy epoxyeicosatrienoic acid derivatives (HETEs) are known biomarkers of hypertensive disorders.¹⁰⁶⁻¹¹³ One specific HETE derivative, 20-hydroxyeicosatetraenoic acid (20-HETE) has been well studied as a biomarker for hypertension.^{107,108,113} 20-HETE (structure shown in Figure 1.9) is differentiated from other HETEs by having a terminal hydroxyl group (the 20th carbon position), while all other HETEs will have a terminal-CH₃ and a different substitution of the hydroxyl group. The significance of 20-HETE, combined with the difference in functional groups between it and other EETs and HETEs makes it an ideal metabolite for study by SERS analysis with a final goal of clinical diagnosis of hypertensive disorders.

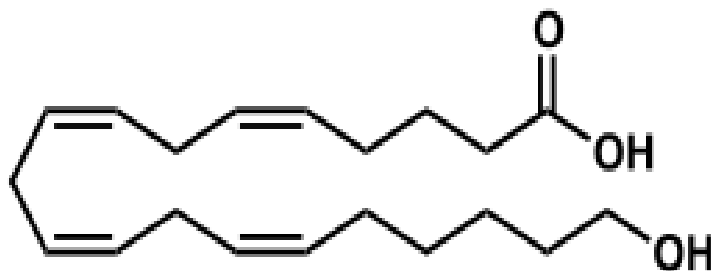


Figure 1.8 Molecular structure of 20-hydroxyeicosatetraenoic acid (20-HETE), the primary biomarker for preeclampsia as determined by MCV and the primary analytical target for the studies of this thesis.

Early preeclampsia detection is of utmost significance. It has been identified as the most common of the severe birthing complications. In 2005, an article in *Science* claimed that around 2.5-3% of pregnancies result in preeclampsia or eclampsia.¹¹⁴ In 2016, in the journal of *Pregnancy Hypertension*, it was reported that in the US, 49% of pregnancies result in a hypertensive condition.¹¹⁵ Of those hypertensive pregnancies in the US, 25.8% were preeclampsia.¹¹⁵ This statistics mean that over the course of 11 years, the rate of preeclampsia

has increased from 2.5% to 12.64%, a 405% increase. The Journal of Maternal-Fetal & Neonatal Medicine suggested a 5% worldwide preeclampsia rate in 2018, suggesting a 100% increase worldwide during the same time period.¹¹⁶ Within the same month, International Journal of Reproduction, Contraception, Obstetrics and Gynecology suggested a 7-10% rate of preeclampsia in US pregnancies.¹¹⁷ Regardless of the statistics that are used, there is a general trend toward an increase in preeclampsia's prevalence and due to its high mortality rate, early detection of the condition is desirable for the sake of preventing still births and maternal suffering and death.¹¹⁴

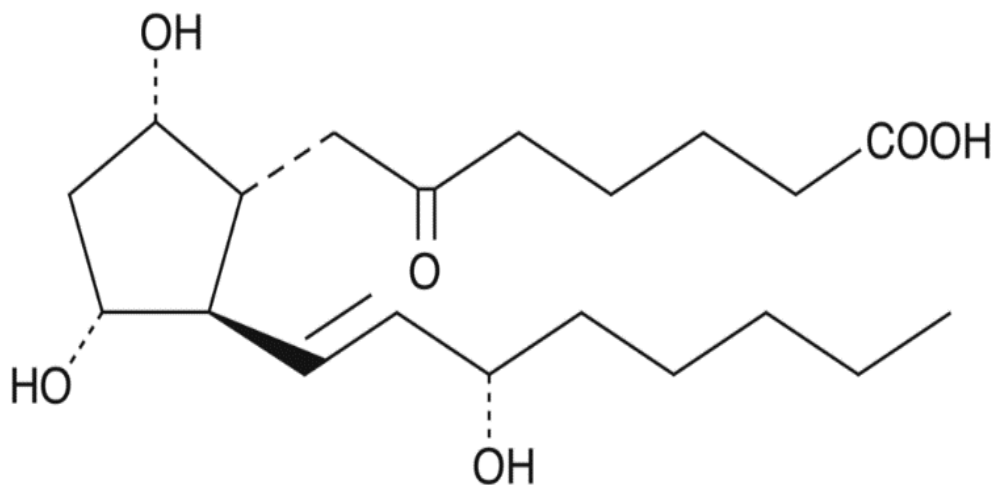


Figure 1.9 Structure of 6-keto prostaglandin $f_{1\alpha}$ (6-keto). This lipid is a powerful vasodilator found in high abundance in women with proper lipid balance during pregnancy and in seminal fluid.

A possible explanation for the increased prevalence of the birthing complication with the highest mortality rate in the western world was given in June 2016 by Mayoral-Andrade *et al.*¹¹⁸ The authors suggest that 6-keto prostaglandin $f_{1\alpha}$ (6-keto), the original target given by the

Medical College of Virginia for this project, is directly correlated to onset of this hypertensive disorder. Like many prostaglandins, is a vasodilator.¹¹⁹ This lipid is found in high concentrations in seminal fluid and known to increase vaginal and uterine blood flow in coitus.¹²⁰ It is also known well that the human body rejects foreign bodily fluids and tissues, including the womb reacting to reject seminal fluid until it becomes accustomed to the presence of a particular composition of seminal fluid, causing immune responses, including vasoconstriction, upon initial exposure to the RNA and protein composition of a particular man's semen.¹²¹⁻¹²⁴ Upon increased exposure to the RNA and protein composition of a particular seminal fluid mixture, the immunoresponse decreases.^{122,125} When this immune response decreases, the effect of 6-keto is more prevalent, causing decreased blood pressure post-coitus.¹²⁶ Mayoral-Andrade *et al.* suggest that the increase in preeclampsia is derived from an increased use of barrier method contraceptives decreasing the amount of exposure that the average woman has to seminal fluid of her partner prior to conception, leading to blood pressure complications due to immunoresponse of the expectant mother and insufficient vasodilation from the 6-keto content of the father's seminal fluid.¹¹⁸ They conclude that with increased prevalence of the use of barrier method contraceptives to prevent the spread of STDs and pregnancy, there is a direct increase of the risk of preeclampsia.

Later studies have suggested that 6-keto may not be the leading lipid of concern in preeclampsia, nor the most viable target molecule for diagnostic detection. Figure 1.9 shows a molecule of 20-HETE) This lipid has shown recent ties to hypertensive conditions and has been suggested to be a major contributor to the vasoconstriction and hypertension.^{113,127,128} For this reason, in the majority of studies shown in this thesis, 20-HETE will be the target lipid for detection. On top of the biological significance as a vasoconstrictor in pregnant women, the

research shown in chapter 3 of this thesis will demonstrate the ability to selectively detect this lipid, even when it is in a mixture with other lipids, which are all at far greater concentrations, making it a viable diagnostic target.

Early detection and diagnosis of preeclampsia is essential for the health of both the mother and developing child. If detected before symptoms present. It is possible to put the mother on a baby aspirin regimen that would prevent hypertension from setting in. Preventing hypertension prevents stress on the uterus and fetus, which can lead to birth defects. Preeclampsia, at late stages, will also cause seizures in both the mother and the offspring, which lead to further damage to both the mother and child from convulsions and insufficient oxygen flow to the brain.

Currently, the symptoms of preeclampsia can be mitigated, however it is often too late to act quickly enough to alleviate all symptoms, nor early enough to prevent them entirely. Currently, this birthing complication is only able to be diagnosed after symptoms have presented themselves, mostly in the form of regular blood pressure checks. However, the pharmacological changes that occur in the mother's body theoretically begin to occur at conception, generating the possibility of designing an assay capable of detection and diagnosis prior to the onset of symptoms. Many of the more stable biomolecules involved in this condition are lipids found in human blood and urine, leading to the investigation into detecting these lipids before detriment to the mother and offspring occur.

1.7 Challenges of Surface Enhanced Raman Spectroscopy

SERS of lipids provides challenges beyond the similarities of molecules.^{48,49} Lipids are flexible molecules, allowing for variability in how they can lay on the substrate, and therefore

which functional groups are found in the hot spot of the nanoparticles (see Figure 1.11 for illustrated example)¹³¹. Furthermore, lipids easily burn, forming amorphous carbon peaks in their spectra. The facile burning of lipids arises not only from the flexibility of the molecules allowing for substantial amounts of energy to be imparted in a localized area, but also from the energetics of the photons of the excitation source (in the studies associated with this thesis, a 532.1 nm laser). The energy of less than two photons per bond is necessary to induce dissociation.^{72,132} Even if only one thousandth of a percent of the energy of a photon were able to be converted to bond breaking, there would still be the possibility of breaking ten thousand molecules per second with the nine-microwatt beam energy at the focused area of observation, using the one hundred times optical objective from this experiment. The semi-conjugated systems of many EETs and HETEs will provide resonance stabilization, however even this can be overcome by the massive number of photons emitted by the excitation laser.^{103,113,133,134} Moreover, silver nanoparticles are photoactive catalysts, resulting in the substrate increasing the number of dissociative events. Still more complications in detecting lipids arise from lipid interactions in polar solvents.^{129,135-137} In water and ethanol, micelles often form due to the entropic favorability of exposing the polar head to the solvent while protecting the nonpolar tails of the lipids. The nonpolar tails will interact with one another, reducing the systemic energy and increasing stability. The formation of micelles will also result in aggregates of lipids, reducing the chances of lipids being in the observed area, reducing the chances of uniform detection.^{106,138,139}

Table 1.1 Bond enthalpies and energetics of bond breaking using 532.11nm excitation lasers for common organic bonds.

Bond	Bond Enthalpy (kJ/mol)	Energy (J/bond/molecule)	Photons of 532.11nm light per bond
C-C	348	5.78E-19	1.55
C-H	413	6.85E-19	1.83
C-O	358	5.61E-19	1.50

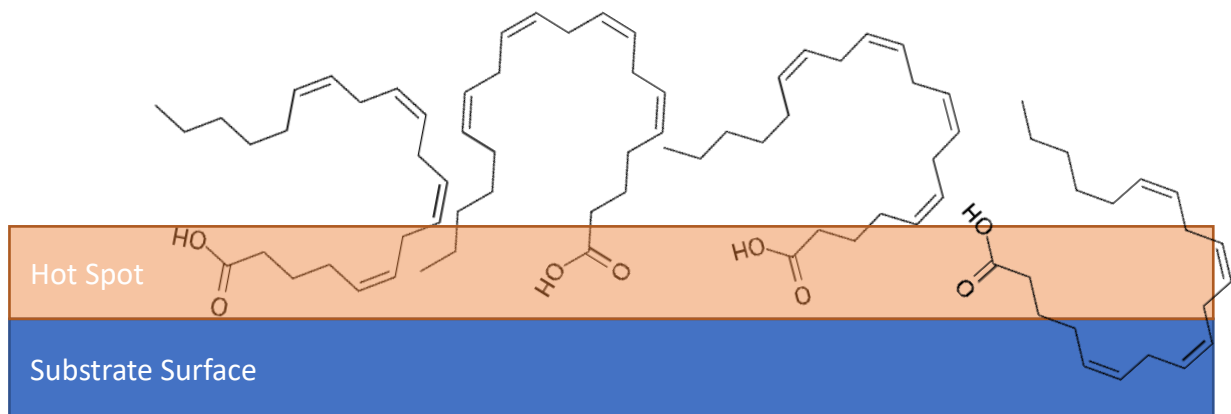


Figure 1.10 Illustrated example of the variability of functional groups found in the plasmonic hot spot, based on the assumption that one functional group will serve as a pivot point for interaction with the substrate surface, in this case the carboxylic acid.

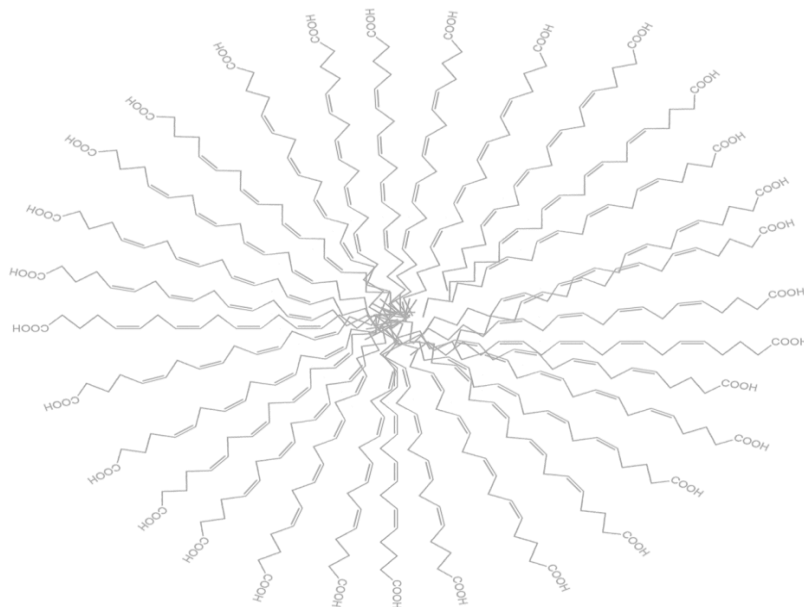


Figure 1.11 Micelle formed from arachidonic acid. Because of solvent interactions, it is believed that AA forms micelles in ethanol solution at high concentrations, because it would be energetically favorable to have all of the non-polar tails of the lipid interacting with each other rather than the ethanol while the carboxylic acid heads would still interact with the ethanol.

1.8 Current Detection Methods

Although SERS comes with its own unique challenges, it shows promise for clinical applications, filling a void created by the weaknesses of other analytical techniques. The rapid detection, low limit of detection, high sensitivity, mechanical simplicity and ease of use give SERS a competitive edge in the world of modern medicine.

Currently, many diagnosis are made with liquid chromatography coupled with mass Spectrometry (LC-MS).^{94,140,141} LC-MS is the coupling of two separate analytical techniques. LC uses a high pressure column that separates the analytes by a chemical or property that the column is designed to exploit.^{142,143} These properties range from pH sensitivity to functional groups present on the molecules to the size of the analyte particles.¹⁴⁴ The column then uses a mass spectrometer as a detector and second dimension of data collection. The mass spectrometers used in LC-MS typically have an electrospray ionization source.¹⁴⁵⁻¹⁴⁷ This works by having a highly charged needle will transfer an electron to the analyte molecules as they pass through the tip.¹⁴⁵⁻¹⁴⁷ The solvent will not be ionized and is easily extracted before getting to the mass analyzer.¹⁴⁸ Most of the time, the MS analyzer associated with one of these systems would either be a quadrupole (quad) or a triple quad system.^{149,150} A quad works by generating an electromagnetic field that will allow only analytes of a certain mass to charge ratio to remain within the field and all others will be ejected from the field before they can pass through the quad.^{151,152} To achieve this, field, typically two opposing poles will have an RF current running through them while the other two have DC currents.^{151,152} If a triple quad option is used, the first quad system is employed, the first cell can be used as an initial mass analyzer, the second as a collision cell to induce molecular dissociation and the third as a post collision cell mass analyzer, to glean further information about the functionality of the analytes.^{152,153}

Though LC-MS is a powerful technique, it has many drawbacks for clinical applications. The first and most prevalent complication with liquid chromatography is biofouling.^{142,154} When looking at blood samples, clotting, aggregation of hemoglobin and infectious globs can clog the pores of the column, increasing pressure, reducing flow and decreasing the efficiency for peak separation.¹⁴² To avoid this from causing issues with data collection, Many components of

biological fluids are also difficult to separate because they have similar chemical properties in regards to polarity and chemical interactions.¹⁵⁴ Additionally, the column must be flushed to remove any previous samples to prevent contamination with future samples.¹⁵⁴ Furthermore, maintenance of these systems requires scrupulous care to ensure proper separation, with particular attention having to be paid to the pump system and the inlet.¹⁵⁵ Additionally, there are

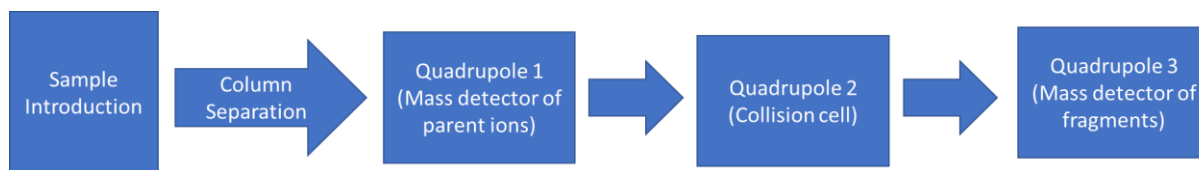


Figure 1.12 Block diagram of a liquid chromatography-mass spectrometry (LC-MS)

instrument set to daughter ion mode, in which the liquid chromatography column is used for separation of analytes, the first quadrupole detects the mass of non-fragmented ions introduced to the MS, the middle quadrupole is used as a collision cell to fragment the ions to glean information about functional groups present in it and the last quadrupole detects the fragmented ion masses by measuring the charge to weight ratio of ions that are not ejected from the electromagnetic field of the quadrupole.

vast quantities of solvents that are washed through the system, often requiring expensive disposal options to be used due to the nature of biological fluids and the organic solvents required for proper separation.¹⁴⁹

Even if the LC does not interfere with the sample, mass spectrometry (MS) has complications of its own, both the sample introduction mechanism and detector limit the utility of MS in clinical settings. Firstly, the substance being studied must be able to be ionized in a reproducible manner without damaging it.^{156,157} Electrospray ionization can ionize many

analytes, however some biological molecules will be dissociated by ionization.^{146,158} Others will not have a consistent amount of charge added to them by this method.¹⁵⁹ Moreover, the lower limit of detection of a typical LC-MS system, though it is theoretically able to detect a single molecule, in all reality is typically around 100 ng/ mL.¹⁶⁰ The key analyte studied in this research is found at approximately 28 ng/mL in a preeclamptic pregnant woman, and would need to be able to detected at even lower concentrations for possible detection before symptoms present.^{108,112,134} Furthermore, quantitation with MS requires a mixture between precise calculation and artful guessing of the bounds of peaks in order to integrate the area under the curve, and often requires the use of an internal standard. Lastly, and most importantly, LC-MS cannot be used because many of the lipids found in human plasma have the same molecular weight and functional groups, making absolute identification by this method highly improbable.¹⁶¹

Aside from LC-MS, few other analytical tools are viable for lipid analysis. Common techniques like infrared spectroscopy (IR) or nuclear magnetic resonance (NMR) require a pure sample.¹⁶² GC-MS does not allow detection of non-volatile substances.¹⁴¹ UV-Vis spectroscopy does not have the necessary resolution to differentiate one class of lipids from another, let alone various substitutions of isomers.⁸³ Though cryogenic scanning tunneling electron microscopy (cryo-STEM) is close to having the resolution needed to differentiate one lipid from another, it is an imaging technique that would require vast quantities of time to look at a large enough sample to make concentration calculations.¹⁶³ Florescence spectroscopy, though sensitive enough to detect at the necessary LOD, does not have the resolving power nor the specificity needed to differentiate lipids and would only be helpful in detecting florescent lipids.¹⁶⁴ Electrophoretic separation and detection techniques require differences in electrical potential of the analyte, and

thus would not have the separatory ability necessary for lipid analysis.¹⁶⁵ Though many techniques exist, they all present insurmountable challenges for this clinical application. Herein, this thesis will discuss the viability of detecting 20-HETE, a metabolite believed to play a key role in hypertensive disorders (including preeclampsia), via surface enhanced Raman spectroscopy (SERS) down to 1 pM concentrations, even when mixed with other lipids at orders of magnitude higher concentrations, showing the preliminary clinical viability of SERS for medical diagnosis.

1.9 Surface Enhanced Raman Spectroscopy Substrates

Selection of an adequate SERS substrate must consider several factors. The main considerations are the nanoparticle material, nanoparticle shape, plasmon resonance of particles, deposition method employed and capping agent selection (when applicable).¹⁶⁶ Herein, this section will discuss the reasons why the final substrate used for this research were drop-cast silver nanoplatelets capped with trisodium citrate.

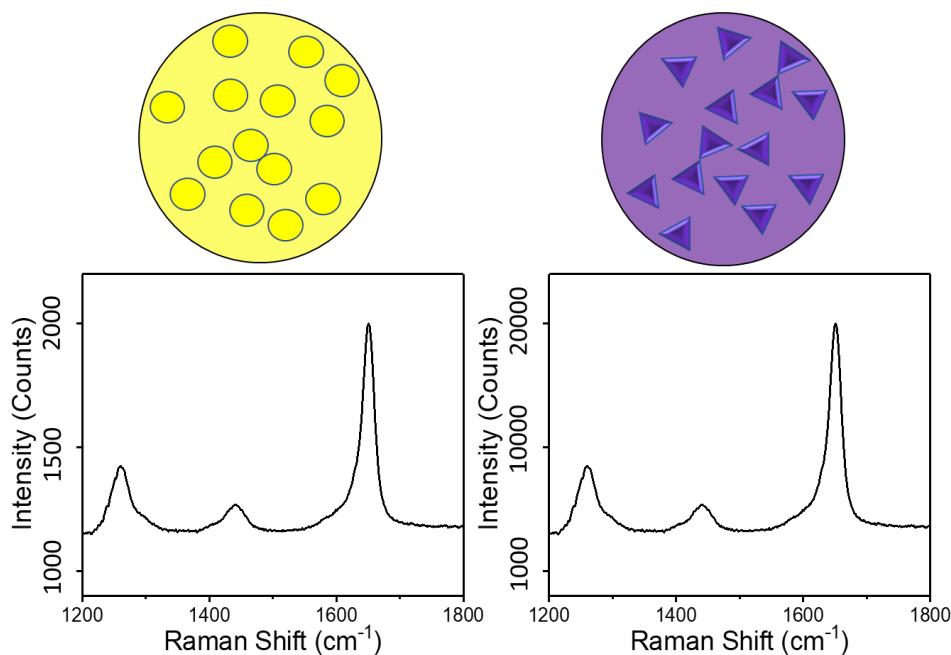


Figure 1.13 Difference in intensity of peaks between thiol coated Au NPs (left) and citrate coated Ag nanoplatelets (right), *ceteris paribus*. The citrate coated Ag nanoplatelets provide greater enhancement, resulting in a far higher absolute intensity of the Raman signal, as compared to the thiol coated Au NPs, which was unexpected due to expected lipid-thiol interactions and lipid-citrate repulsion.

Initial experiments of the research presented here used isotropic non-polar gold nanoparticles. Later, silver nanoplatelets with a polar capping ligand were used to increase the enhancement factor, decreasing the lowest limit of detection of the system.¹⁶⁷ Though there were no longer lipid-aliphatic interactions, the vertices focused the LSPR, increasing the strength of the localized magnetic field at the corners and enhancing the overall signal of the substrate, through what is referred to as the plasmonic antennae effect.^{133,133,168,169} The absolute intensity of a 1 pM concentration of a lipid was only 1137 counts above the baseline with round nanoparticles while it was 17942 with platelet nanoparticles. Both particle substrates had a peak

absorbance in their UV-Vis spectrum that matched the wavelength of the excitation laser. The laser power was the same and the collection parameters were identical. Other than the particles used for the substrate, everything else in these experiments was run identically.

Nanoparticle substrates can be fabricated through several methods. Substrates can be developed most uniformly through a method known as lithography. In lithography, a gradient is used to allow light to interact with only certain regions of a plate covered in the substrate material (*i.e.* silver, gold...).¹⁷⁰ This causes particle formation only where the light is allowed to shine.^{171,172} This method requires expensive specialized equipment, and therefore was not used. Spin coating can deposit thin layers of particles that are still randomly distributed, but relatively evenly dispersed.¹⁷³ Challenges with this method include even deposition of substrate, which often requires utilization of a low volatility organic solvent for rapid evaporation without cracking.¹⁷⁴ A bigger problem for SERS, is that an additional compound must be introduced.¹⁷³ This compound, usually a silane, serves to attach the particles to the slide (typically glass, quartz or aluminum).¹⁶⁶ It adds more interference to the SERS spectrum because more functional groups will be found within the system's focal depth that are also located within the plasmonic hot spot of the nanoparticles.¹⁷⁵ This method does not guarantee uniform enhancement, adds spectral interferences and requires specialized equipment. A third, more facile and less precise method of slide fabrication is through drop casting¹⁷⁶. A drop cast substrate is made by simple deposition of the substrate solution onto the desired slide and allowing the solvent to evaporate either naturally, through reduced pressure or by increased temperature.¹⁰¹ Drying under vacuum conditions quickens the process compared to natural evaporation and prevents particle deformation that can result from thermally induced evaporation.¹⁷⁷ This substrate preparation method was used in all studies herein mentioned in this research.

1.10 Thesis Statement

Herein lies the thesis research and goals. Two main goals were developed for this research, in conjunction with the funding from the National Institute of Child Health and Human Development /NIH/DHHS (1U01HD087198-01). These goals were (Goal 1) to develop a substrate capable of 1 pM detection of lipid biomarkers associated with preeclampsia and (Goal 2) to demonstrate the viability of using SERS as a diagnostic clinical tool for medical conditions involving deviations from normal lipid levels in bodily fluids.

Goal 1 was pursued by first establishing the proper metal to be employed in developing the substrate. Though gold was initially used due its plasmon absorbance around the wavelength of the excitation source, later silver was used to allow for greater nanoparticle growth, which allowed tuning of the plasmon to the laser wavelength. Next, the shape of the particles was selected. Initially, gold nanospheres were used because of the ease of making monodisperse gold particles of this shape in a low volatility organic solvent. Later, platelets were selected, because their sharp edges took advantage of the antennae effect, generating stronger plasmonic hot spots, which resulted in increased signal enhancement. Originally, 1-octanethiol was used as a capping ligand, with the hypothesis that the aliphatic chain of the organic capping ligand would interact with the nonpolar regions of the lipid, allowing for more uniform placement of functional groups in plasmonic hot spots. Eventually, citrate was used due to limitations of silver platelet ligand exchange and maintenance of a clean region of the spectrum of the substrate, allowing for facile detection of the characteristic peaks of the biomarker lipid (20-HETE). Lastly, drop casting was employed for the sake of rapid synthesis of slides, allowing large volumes of data to be gathered during the short span of this research.

Goal 2 was accomplished by looking at lipids in progressively more complex systems. Initially, solid lipids were studied with Raman spectroscopy to establish a reference spectrum and allow for analysis of functional group activity at the surface of the substrate. Next, lipid solutions of a single lipid in pure ethanol were analyzed with SERS substrates to study the effects of concentration on the signals. After that, lipids were mixed to ensure that the desired lipid could be identified in various concentration ratios, ranging from a 1:1 ratio of the biomarker to competitor lipid to a 1:1000 ratio. Lastly, a “synthetic plasma” was developed by mixing the biomarker lipid with three competitor lipids to establish that the biomarker could still be identified in biologically relevant concentrations.

Chapter 2: Experimental

2.1 Raman Spectroscopy and Surface Enhanced Raman Spectroscopy

The primary technique for lipid analysis in this study was Surface Enhanced Raman Spectroscopy (SERS). SERS is a modification of Raman Spectroscopy. Raman spectroscopy is a fingerprinting technique used to take rovibrational measurements of analytes that are deposited in the solid state or dissolved in solutions.¹⁷⁸ The Raman effect, discovered by C. V. Raman in 1928, is derived from an inelastic scattering event causing wavelength shifting of monochromatic source light due to energy being imparted by the light on the rotational and vibrational modes of the analyte, inducing scattered light with a different wavelength than the incident light.¹⁷⁹ There are three kinds of light scattering observed in nature: Raleigh scattering, Stokes scattering and anti-Stokes scattering.²⁶ Raleigh scattering is the most common scattering event, which occurs when a vibrational mode is excited to a virtual state and comes back down to the initial state.^{180,181} This results in excitation and emission wavelengths of the scattered light resulting in no change of wavelength, and thus does not provide any spectroscopically useful data.²⁶ The other two categories of scattering, Stokes and anti-Stokes scattering are sometimes lumped together into the category of Raman scattering, even though they are distinctly different scattering events.¹⁸² Both can provide useful Raman spectroscopy data. In a Stokes scattering event, excitation occurs from an initial excitation state to the virtual state and returns to a higher state than the initial state, resulting in a red shift due to energy being absorbed by the analyte,^{26,182,183} increasing the wavelength and decreasing the frequency and energy of the scattered light.¹⁸² In Anti-stokes scattering, as one can deduce, the opposite phenomenon occurs. A scattering event occurs with an electron from an excited energy state, goes to a virtual state and upon relaxation, induces a blue shift by returning to a lower energy state than the initial

state.¹⁸² As the Maxwell- Boltzmann distribution or an energy well diagram would suggest (shown in Figure 6), Stokes scattering is more common than anti-stokes scattering because starting in a lower energy state is more common, making this form of scattering more commonly accessible than the excited vibrational states that are required for anti-stokes scattering.¹⁸⁴ As a result of this effect, stokes scattering, which results in positive wavenumber measurements, lends itself to greater intensity spectra.¹⁸² Though anti-stokes scattering results in less intense signals, it also results in a large reduction in laser induced fluorescence.¹⁸³ Highly fluorescent analytes can have up to fourteen orders of magnitude greater fluorescent intensity than the Raman scattering intensity.¹⁸⁵ However, since the matrices studied during my tenure at VCU were only minimally fluorescent , the increased intensity of Stokes spectra were desirable in order to decrease the LOD.^{28,186}

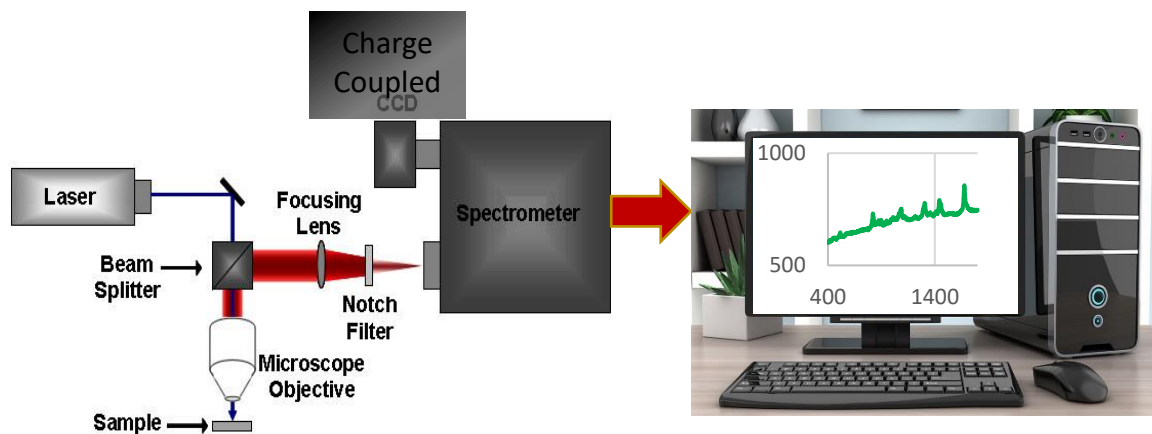


Figure 2.1 Raman spectrometer instrumentation.

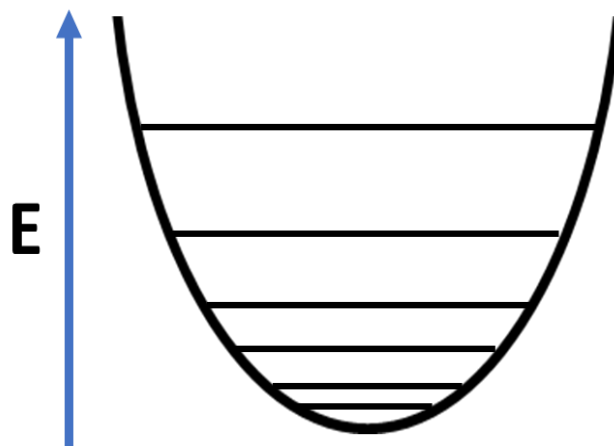


Figure 2.2 Vibrational energy well diagram

To further increase the signal of Raman spectra, plasmonic nanostructures are employed to make a substrate which increases the scattering efficiency of the system. This technique is known as Surface Enhanced Raman Spectroscopy (SERS).^{185,187,188} A localized surface plasmon resonance (LSPR) is induced on the roughened surface of select metal nanostructures, resulting in enhancement of scattering efficiency.^{185,189,190} A graphic of how an LSPR works is shown in Figure 7. Plasmonic metals must possess a small positive imaginary dielectric constant and a negative value for the real function of the complex number.¹³⁻¹⁵ This limits the metals that are used to typically silver and gold, however there are reports of copper, aluminum, lithium, sodium, indium, zinc, platinum, tantalum and cadmium being used to produce plasmonic effects for SERS.¹⁹³⁻¹⁹⁷ A plasmonic structure that is oriented perpendicularly to the excitation source that is in resonance with the substrate will induce an electromagnetic field that enhances photon excitation, increasing the frequency of scattering events, and therefore increasing the intensity of a Raman signal.¹⁹⁸ Because of this, roughened surfaces tend to make better SERS substrates.^{133,198} Additionally, roughened surfaces can act as antennas, creating a focusing effect

of the LSPR to generate more intense plasmonic “hot spots” with more focused magnetic fields.^{133,169,195} These “hot spots” arise from displacement of charge density from the equilibrium state of the surface of the nanoparticles, inducing an oscillation, which on point surfaces will cause interference patterns of magnetic fields as the electronic charge traverses the nanoparticle.^{24–27}

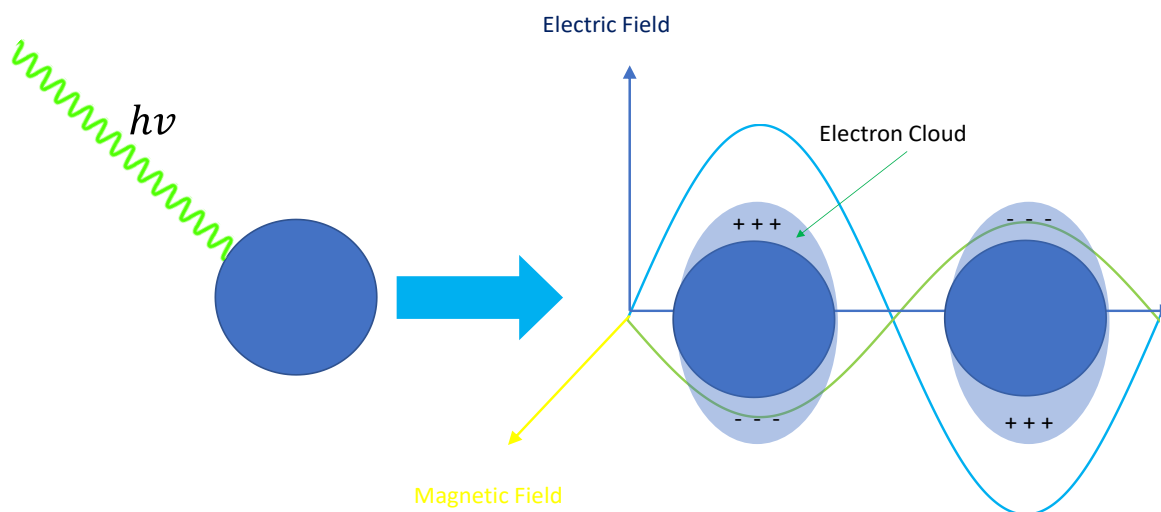


Figure 2.3 Diagram of localized surface plasmon resonance.

There is an additional cause of Raman enhancement that was not observed in these studies. A charge transfer mechanism can also enhance Raman scattering if chemical adhesion of the analyte to the plasmonic structure is present.^{89,90,203} Electrons are transferred at double the wavelength of the inherent electronic exciton of the absorbed analyte.²⁰⁴ Since most organic molecules have inherent excitations in the ultraviolet (UV) range, this transition is often most efficiently with a visible excitation source.^{203,205} This method of enhancement was not likely utilized in the studies discussed in this thesis because it requires a chemical bond between the substrate and adsorbate.

2.2 Ultraviolet-Visible-Near Infrared Spectroscopy

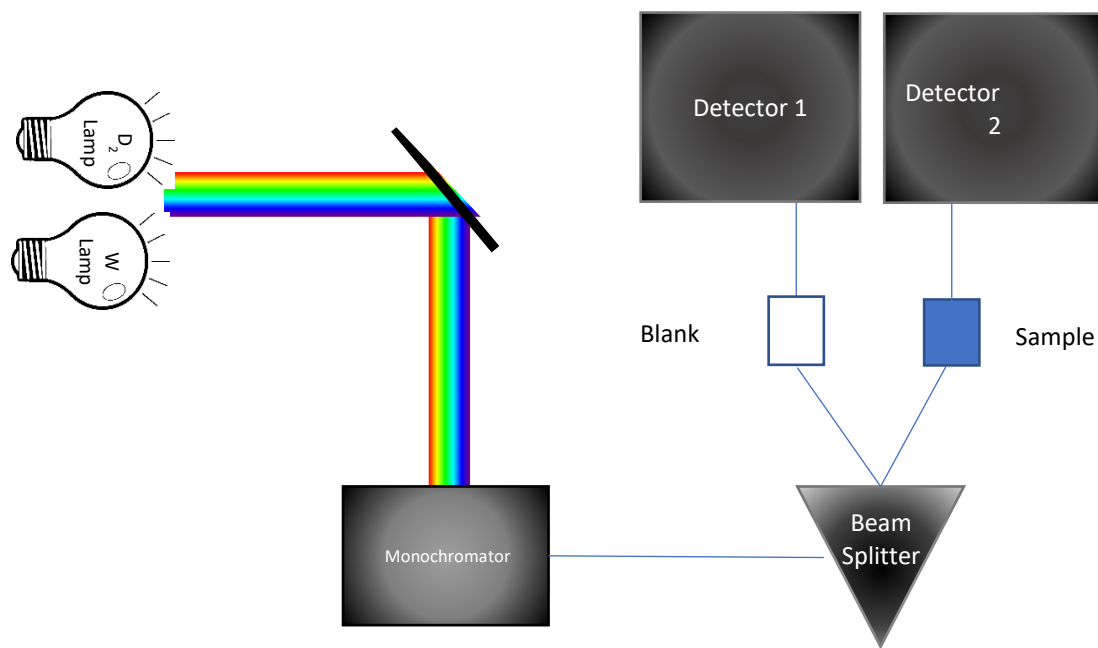


Figure 2.4 UV-Vis operational schematic.

Another key instrument for this study was ultraviolet-visible absorption spectroscopy (UV-Vis).^{82,83} UV-Vis operates by shining light through a grating and scanning the frequency of light passing through a sample to determine the absorbance at a given wavelength range. A typical system for a dual path UV-Vis spectrometer is displayed in Scheme 2.2.

Many UV-Vis spectrometers use multiple lamps to ensure full coverage of the full spectrum of desired analysis.^{82,206} In this case, a deuterium lamp was used as a UV source and a tungsten lamp was used as the visible light lamp.²⁰⁶ This broadband of light is then passed through a monochromator and swept through the desired wavelengths. The beam is split. One part of the beam is passed through a blank or reference sample. This sample is used to consider

any absorption by the cuvette, solvents or solvates other than the desired analyte. Additionally, it allows for correction of power fluctuations from the source. The other beam is passed through the desired sample and transmitted light is measured, allowing the absorbed light to be quantified at each measured wavelength.

2.3 Nanoscale Microscopy and Imagine

The third and final characterization technique used for the studies that will follow was Transmission Electron Microscopy (TEM). In 1931, Ernst Ruska and Max Knoll designed the first electron microscope, earning the Nobel Prize for Physics in 1986 for developing the first TEM, an instrument capable of imaging objects smaller than what could be probed with visible light. The diffraction limit of an imaging technique is the smallest difference between features that can be seen with the given source for the imaging. It is determined by several factors, such as the diameter of the detector, angular separation of observed features and the wavelength of the electromagnetic radiation (EMR) used to take the image. The most constraining factor of a given system will determine the minimum size that will be visible with a system. With modern imaging devices, the wavelength of the probing EMR is typically the limiting factor. Since visible microscopes rely on the wavelength range visible to the human eye from approximately 390-700 nm, 390 nm is the smallest sized structure that it can probe. Since nanostructures are definitionally less than 100 nm, another technique using a small wavelength had to be developed.

Energy (keV)	Wavelengths of e ⁻ beam (pm)
100	3.7 014
120	3.3492
200	2.0589
300	1.9687
1250 (most powerful electron microscope presently in existence)	0.73571

Table 2.1 Energy and De Broglie wavelengths of electron beams.

Transmission electron microscopes use a high energy electron beam to minimize the wavelength of the probing source and increase the resolution of the device. The greater the voltage of an electron beam is, the smaller the wavelength of the electrons will be. Table 2.1 shows the minimum resolution achievable with various voltages of electron beams. This size corresponds to the De Broglie wavelength of the electron at that energy, given by the equation: $\lambda [pm] = hc/pv$ where $\lambda [pm]$ is the wavelength in picometers, h is Plank's constant, c is the speed of light and pv is the relativistic kinetic energy. The electron microscopes used for this study used 120 keV beams. The theoretical minimum size that can be probed will, of course, be pixelated with the minimum wavelength representing the smallest pixel size that can be shown, making the effective minimum size larger than this wavelength.

The electrons are focused into a beam by electromagnetic lenses, reducing multiple scattering events and increasing cohesion of the beam. The instrument works under a high vacuum to decrease interference, interactions of the beam with gas molecules and degradation under the high energy beam. As the beam contacts an object, primarily the analyte, electrons will interact with the shell electrons of the substance being observed. Electronic detectors have replaced the electron sensitive plates that were originally used in conjunction with films for images.

Images gathered by transmission electron microscopy in this research served several purposes. They showed the morphology, or shape, of the particles. It also allowed for sizing of particles. Lastly, the homogeneity or heterogeneity of an imaged sample could be determined for a sample to glean the importance of the shape, size and uniformity of particles.

Particles are prepared on carbon grids by depositing a small aliquot (10 μL) of a dilute particle solution. This grid was then thoroughly dried, initially at ambient pressure to reduce damage done to the grid and aggregation of particles. Later, the grids were placed under vacuum to ensure that all solvent was evaporated from the grid, preventing issues with the instrument's vacuum or interference and noise in the image due to electron beam interactions with the solvent.

Two important imaging techniques for nanotechnology are scanning electron microscopy (SEM) and atomic force microscopy (AFM). SEMs operate by scanning a focused beam of electrons across the surface, allowing for images of thin films, shown in chapter 4 of this thesis. Detectors around the instrument chamber show images derived from the effects of electrons from the beam interacting with the atoms. These detectors detect back scattered electrons, secondary electrons, characteristic x-rays, cathodoluminescence and transmitted electrons. This technique can image objects down to 1nm. In order to reduce interferences, the imaging chamber is under vacuum. AFM is a high-resolution technique that (in tapping mode) determines a depth profile of a given area by seeing how far down the tip of the probe has to travel before making contact and subtracting that distance from how far down the probe tip goes to the lowest point in the scanned area. These depths are then represented by a color spectrum which shows a two-dimensional image of the surface.

Chapter 3: Initial Studies- Thiol, Thromboxane and Prostaglandin

3.1 Substrate and Acquisition Parameters

Initial studies done before I joined the project (the National Institute of Child Health and Human Development /NIH/DHHS (1U01HD087198-01)), included the choice of the laser wavelength for this study (determined by the VCU Department of Physics) and target analytes (determined by the Medical Campus of Virginia) were set as 6-keto prostaglandin- $f_{1\alpha}$ (6-keto) and Thromboxane B₂ (TXB₂) and soon after shifted to targeting 20-Hydroxyeicosatetraenoic Acid (20-HETE). A 532.11 nm diode laser was used for this study because it had the greatest molecular absorption cross section of the lasers available for Raman studies on the Monroe Park Campus. Though a 785 nm laser would decrease the luminescent background of the analyte, the molecular cross section at this wavelength is nearly non-existent, because C-C, C=C, O-H, C=O, C-O and C-H bonds have strong absorbances in the UV region of the visible spectrum, lending the target lipids to better scattering efficiencies with a green laser than a red or NIR laser.

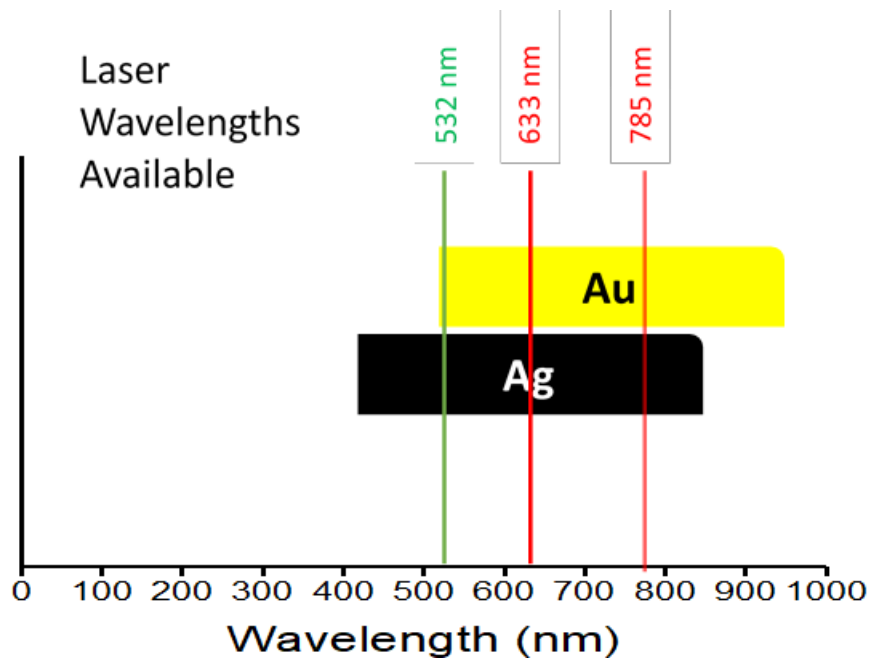


Figure 3.1 Tunable plasmon range of silver and gold and laser wavelengths available for Raman Spectrometers on the VCU Monroe Park Campus.

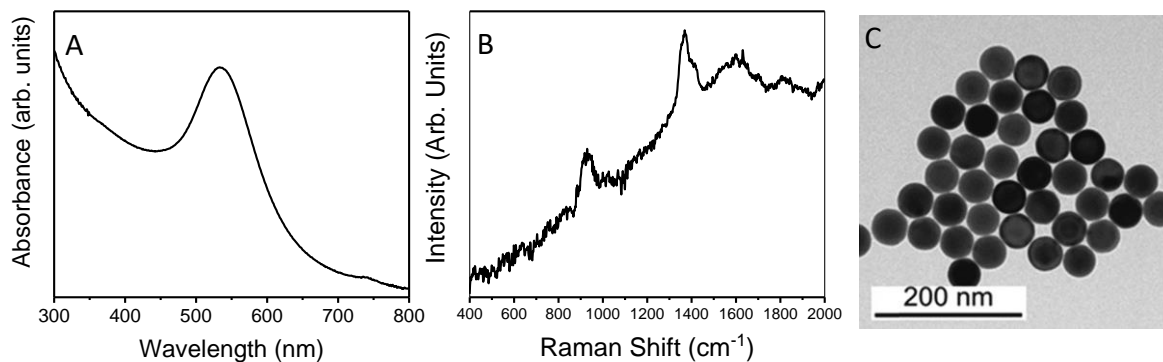


Figure 3.2 (A) UV-Vis spectrum with 530 nm plasmon, (B) Raman spectrum with multiple interfering functional groups which would make lipid detection less definitive and (C) TEM image of glutathione capped gold nanoparticles, used to determine a 30nm average particle size and that the synthesis produced homogenous particles.

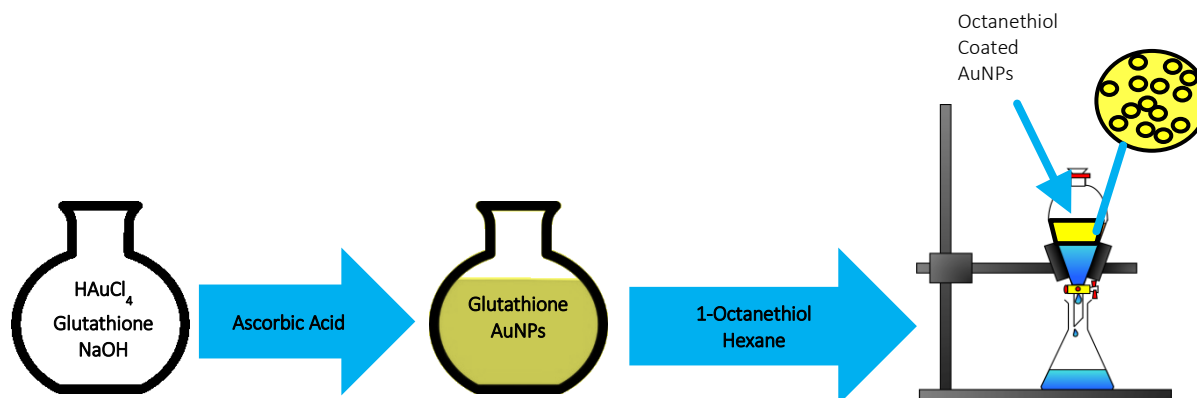
Due to the laser choice, the initial studies indicated that it was best to use of gold nanoparticles capped with glutathione with a peak absorbance at 530 nm (see Figure 3.2 A). These particles showed major Raman peaks from 950-990 cm^{-1} and 1280-1420 cm^{-1} (Figure 3.2 B). To ensure the right absorbance, these particles were grown to approximately 30 nm (see Figure 3.2 C).

3.2 Materials

Octanethiol, L-glutathione (GSH) reduced 98%, Poly(sodium-p-styrenesulfonate) (PSSS, MW = 70K), citric acid, trisodium salt dihydrate (99%), L(+)-ascorbic acid (99%) was purchased from Sigma-Aldrich. Sodium borohydride (NaBH_4) 98% and chloroauric acid (HAuCl_4) 99.999% were purchased from Strem Chemicals. Sodium hydroxide (NaOH), ethanol (99.8%, extra dry, AcroSeal™), methanol (99+%, extra pure) and acetone (ACS grade) were purchased from Fisher

Scientific. 16 M Ω milli-Q filtered water was used in all syntheses. All chemicals were used as received without further purification.

3.3 Synthesis of Octanethiol-Functionalized Au Nanoparticle Thin Films



Scheme 3.1 Synthesis of AuNPs.

The glutathione coated Au NPs were produced by employing a literature method with significant modification to scale up the synthesis.¹ In a typical reaction, 3 mL of 10 mM HAuCl₄ and 300 μ L of 10 mM GSH were added to 50 mL of ice cold milli-Q water. Then, 10 mL of 0.1 M NaOH was added to adjust the pH \sim 12 that resulted in a color change from colorless to pale yellow suggesting the formation of Au NPs. Finally, 3.6 mL of 10 mM ascorbic acid was slowly added at a rate of 0.5 mL min⁻¹ to produce a yellow-brown solution of Au NPs. This reaction is repeated multiple times to produce significant amount of Au NPs. As-prepared Au NPs were purified and concentrated using centrifuge filtration to produce 3 mM Au NP solution. The centrifuge filters (Sartorius, Vivaspin 20 mL MW 30000) filled with ternary NP sol was centrifuged at 3500g for 7–8 min to reduce the volume to 2–3 mL. The concentrated sols were then mixed with 5–10 mL of milli- Ω water and centrifuged to remove the residual byproducts (Na, NO₃⁻, OH⁻, and unreacted thiolates).

The concentrated particle solution is then added to a clean round bottom flask with 2-propanol (10 mL), octanethiol (0.400 mL), and hexane (25 mL). The flask is sealed with a rubber septum and stirred at max speed for 6 h. The contents of the flask are then sonicated and poured into a separatory funnel. The bottom (water and 2-propanol) layer is removed and discarded. The top layer (hexane and octanethiol coated round silver nanoparticles) is collected and centrifuged. The particles are driven to the bottom of the centrifuge tube. All but 2.5 mL of the hexane layer is decanted and discarded. The remainder of the contents of the centrifuge tube are sonicated to re-suspend the nanoparticles. As-synthesized octanethiol-coated Au NPs were drop casted onto glass slides. Each slide is coated by 10 aliquots of 10 μ L of hexane suspension. Between each additional aliquot, the previous addition is allowed to evaporate. The centrifuge tube is sonicated before each transfer of the suspension from the tube to the slides.

3.4 Substrate Durability Testing

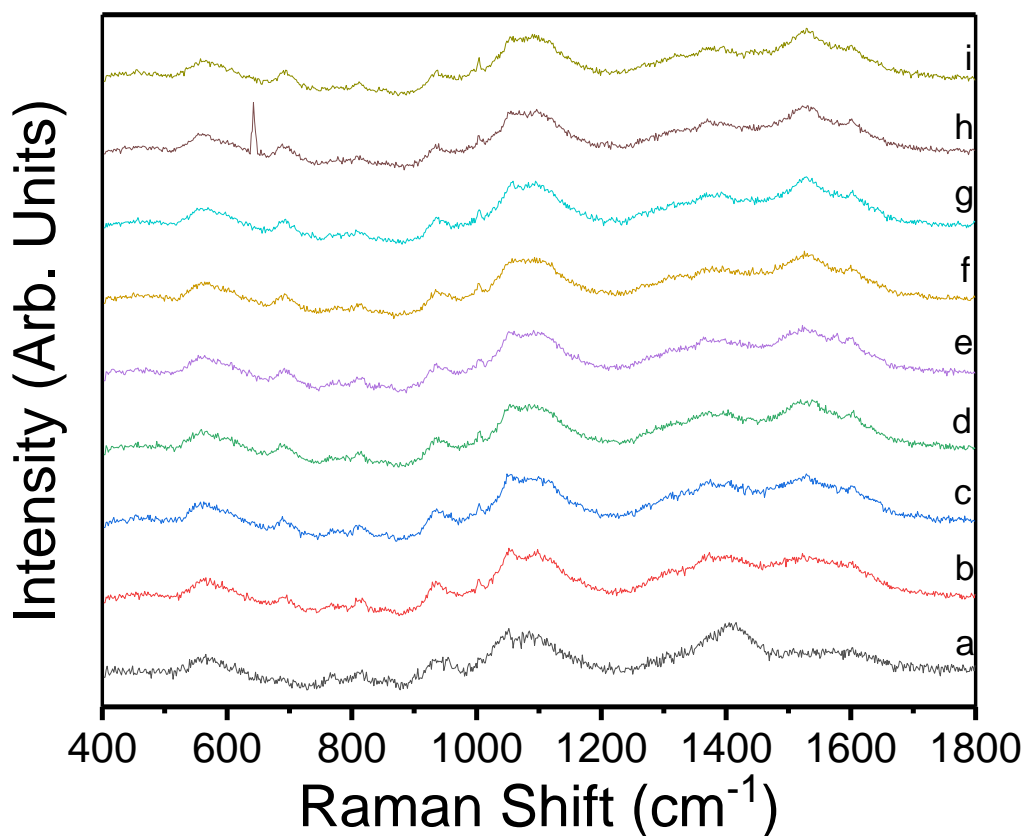


Figure 3.3 Burning study of platelet substrate. In this study, a 532.11nm laser emitting at 20 μW was shined on the substrate to test stability of the substrate under the laser at (a) 1 min, (b) 12 min, (c) 18 min, (d) 24 min, (e) 30 min, (f) 42 min, (g) 48 min, (h) 54 min, (i) 60 min

To ensure that any peaks observed during lipid analysis were not due to degradation of the substrate, the substrate was thoroughly tested (Figure 3.3). The substrate, without any added analytes, was tested for ten sets of six-minute collection times, comprised of twenty collection periods of thirty seconds each. The laser was set to 100 μW , ten times the power used for lipid SERS data acquisition. It should be noted that in Figure 3.3 Spectrum h, a spike at 642 cm^{-1} is due to a solar flare. Data is not shown for 6 min or 36 min points because they contained too many

solar flare peaks to provide useful data. At 1035 cm^{-1} , there is peak diminishment, suggest dissociation of oxygen from the citrate capping ligand. In later 20-HETE studies, this was important observation supported the assignment of the 1029 cm^{-1} to 20-HETE, and not the substrate, because this peak could be seen growing in intensity and sharpening when the lipid was present, while it broadened and decreased in intensity when only the substrate was present. Peak growth at 1518 and 1606 cm^{-1} are due to the growth of amorphous carbon, due to laser induced dissociation of carbon elements of the substrate.

3.5 Acquisition parameters of Raman and SERS Spectra of Lipids

Raman spectra involving lipids were recorded on a Horiba LabRam HR Evolution Confocal Raman Spectrometer equipped with a 532 nm laser. Dilute solutions of (1 mM to 1 pM) lipids were produced in ethanol and 10 μL of lipid solution was dropped onto as-prepared Ag nanoparticle thin films. Lipid solution was dried under ambient conditions prior to spectra acquisition. For all measurements, SERS spectra were acquired with a fixed laser power of 10 μJ , 100X objective, spot size of 2.5 microns, receiving slit width of 200 μm , and 20 second acquisition times and 20 acquisitions, totaling 400 seconds of acquisition per spectrum. No smoothing, baseline correction or any other manipulations were done on any of the data presented.

3.6 Spherical Silver Nanoparticle as SERS Substrates Final Outcomes

Initially, spherical Au nanoparticles coated with octanethiol were utilized to detect 6-keto prostaglandin- $f_1\alpha$ (6 Keto) and Thromboxane (TXB2). It is assumed that hydrophobic octanethiol coating will allow the hydrophobic lipids to better interact with the SERS substrates, and consequently produce optimal signal enhancement. To differentiate Raman peaks of octanethiol

and lipids, we have primarily focused on the 1600-800 cm^{-1} region of the SERS spectrum, which shows no peaks corresponding to SERS substrate and only the highest intensity peaks characteristic of lipids that can be assigned to C=C or C=O vibrations.¹²⁹

Figure 11 shows the Raman spectrum of 6-keto prostaglandin-f1 α along with SERS spectra of different dilutions of 6-keto prostaglandin-f1 α recorded with octanethiol-coated Ag nanoparticle thin films. The highest intense peak at 1679 cm^{-1} in the pure 6-keto is shifted to 1627 cm^{-1} , which is typical for SERS measurements. The SERS spectra recorded at 1 mM and 1 μM solutions are highly reproducible and consistently showed characteristic C=C or C=O bond vibrations at 1627-1633 cm^{-1} . With 1 mM solution (and higher concentrations), decomposition 6-keto prostaglandin-f1 α and production of amorphous carbon was characterized by a doublet observed at 1500-1535 cm^{-1} . However, decomposition of lipid is less evident in 1 μM and 1 nM solutions. SERS spectra recorded from $\sim 1 \text{ cm}^2$ region of lipid droplet show consistent data, suggesting high reproducibility for SERS analysis of 6-keto with spherical Au nanoparticles. It should also be noted that attempts to detect 1 nM and 1 pM 6-keto with octanethiol-coated Au nanoparticles were unsuccessful. Thus, the lower limit of detection (LOD) of 6-keto with octanethiol-coated Ag nanoparticle films is likely in the range of 1 μM – 1 nM.

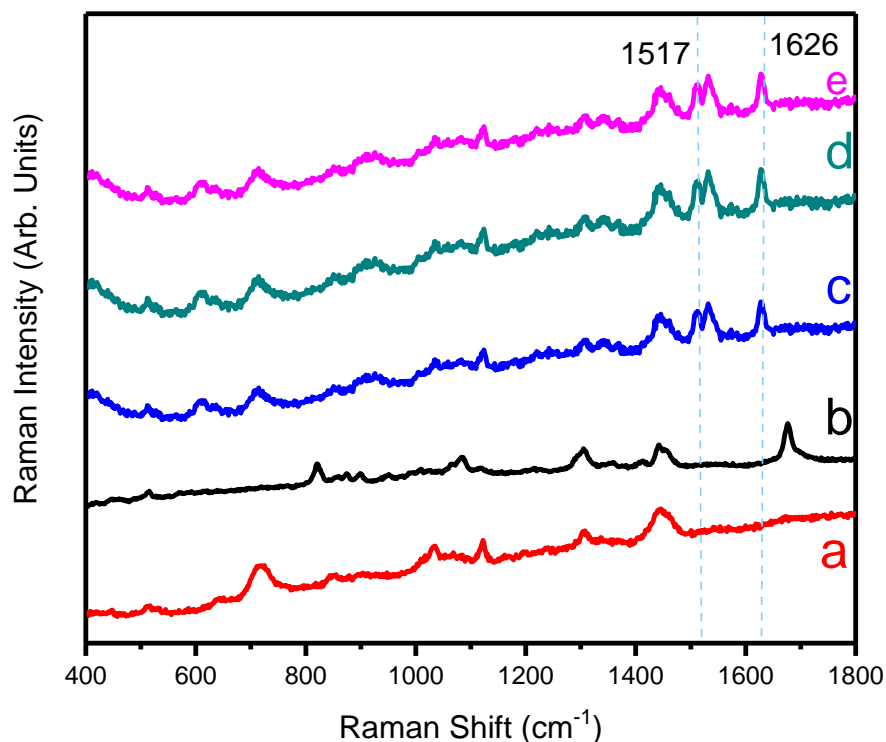


Figure 3.4 (a) Raman spectrum of pure **6-keto prostaglandin-f1a** along with SERS spectra of **6-keto prostaglandin-f1a** acquired with 10 μL aliquots of (b) 1 mM, (c) 1 μM , and (e) 1 nM dilutions. Octanethiol-coated Au nanoparticle films were used as SERS substrates.

Figure 3.4 shows the Raman spectrum of TXB2 along with SERS spectra of different dilutions of TXB2 recorded with octanethiol-coated Au nanoparticles. Pure TXB2 shows a characteristic high intensity doublet at 1656 cm^{-1} and 1691 cm^{-1} . This signal is apparently shifted to 1633 cm^{-1} in the SERS spectra of TXB2 similar to that observed with 6-keto prostaglandin-f1a spectrum (Figure 11). SERS spectra recorded from 1 mM and 1 μM . TXB2 (Figure 12) solutions consistently showed characteristic TXB2 peak at 1633 cm^{-1} suggesting high reproducibility of measurements. It should be noted that characteristic TXB2 peak (1633 cm^{-1}) is slightly shifted away from that of 6-keto (1627 cm^{-1}), which may help with selective analysis of both lipid.

Nonetheless, 1 nM dilutions of TXB2 is undetectable with octanethiol-coated Ag nanoparticle films. While the decomposition of TXB2 is observed at 1 mM concentrations, no such destruction is noted at low concentrations (1 μ M and 1 nM dilutions). Because of this study, it can be concluded that limit of detection of TXB2 with octanethiol-coated Ag nanoparticle films is in the range of 1 μ M to 1 nM.

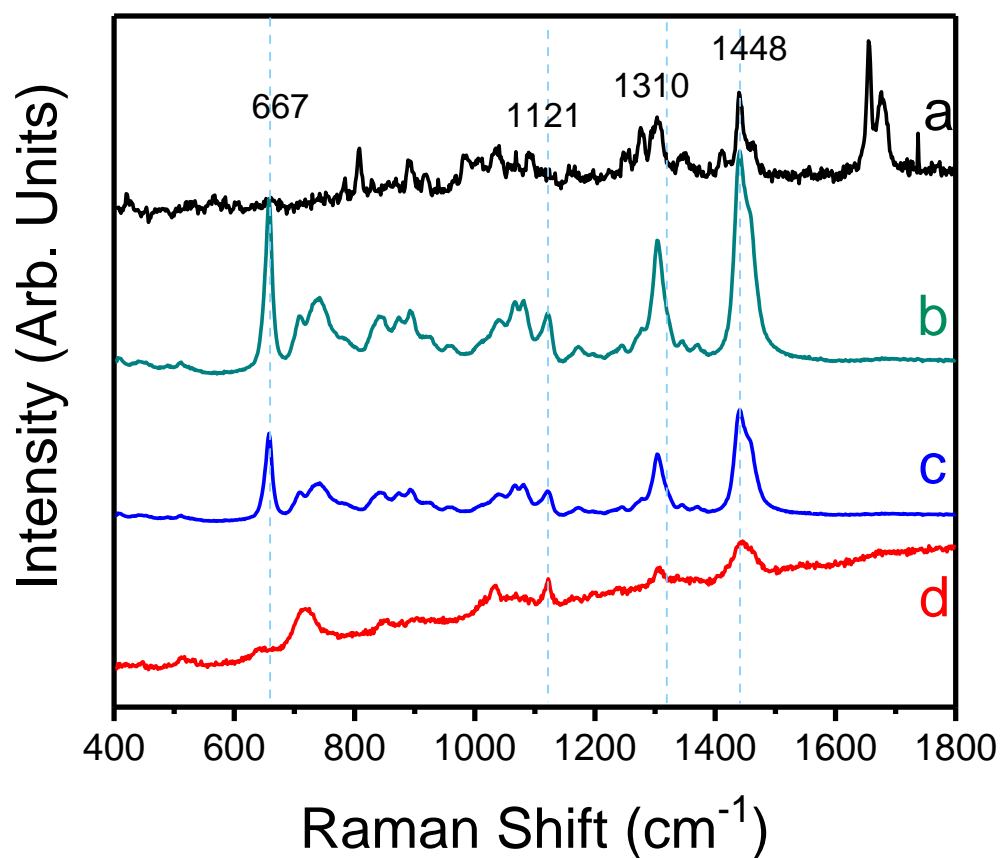


Figure 3.5 (a) Raman spectrum of pure **Thromboxane B2** along with SERS spectra of **Thromboxane B2** acquired with 10 μ L aliquots of (b) 1 mM, (c) 1 μ M, and (e) 1 nM dilutions. Octanethiol-coated Au nanoparticle films were used as SERS substrates.

3.7 Citrate-Coated Silver Platelets as SERS Substrates

It has been shown that Ag nanostructures with high degree of pointy surfaces and faceted structures can produce increased number of plasmonic hot spots for optimum SERS signal enhancement. As such, to further increase the SERS detection capability of targeted lipids, citrate-coated Ag nanoplatelets were also produced. Figure 13-15 show the SERS spectra of different dilutions of 6-keto, 20-HETE, and TXB2 recorded with citrate-coated Ag platelets, respectively. SERS spectra of 6-keto display characteristic C=C or C=O bond vibrations (observed in pure compound at 1679 cm^{-1}) at 1600 cm^{-1} (Figure 3). In addition, significant enhancement of a new peak at 1060 cm^{-1} is noted with different dilutions of lipids. While the 1060 cm^{-1} peak can originate from both lipid and the Ag substrate, time-dependent SERS spectra collected on lipid and only the substrate indicate that 1060 cm^{-1} peak is characteristic to 6-keto prostaglandin- $f1\alpha$ and can be used as a biomarker. With Ag nanoplatelets, detection of 6-keto down to 1 pM level was noted both with 1600 cm^{-1} and 1060 cm^{-1} Raman vibrations. It should be noted that SERS signal intensity of characteristic 6-Keto peaks are significantly higher at 1 nM dilutions in comparison to 1 pM dilutions. It is possible that at high concentration of lipids, crystal growth can happen leading to segregation, limiting the homogeneous distribution of analyte on the SERS substrate. SERS spectra recorded from 1 pM 6-keto on different days and times consistently produced characteristic biomarkers (1600 cm^{-1} and 1060 cm^{-1}), suggesting high reproducibility of the analysis.

On the contrary, SERS spectra of 20-HETE recorded with Ag nanoplatelets show three prominent vibrations (1000 cm^{-1} , 1060 cm^{-1} , and $\sim 1600\text{ cm}^{-1}$) that can be used for selective analysis of 20-HETE (Figure 3.5). These characteristic peaks are visible in from 1 mM to 1 pM dilutions of 20-HETE dilutions and Raman spectral maps collected from a lipid drop area of $\sim 1\text{ cm}^2$. It is important note that SERS signal intensity of 1 pM 20-HETE is higher than that of 1 nM 20-HETE.

Reproducible results were obtained from 1 pM dilutions of targeted lipids on different days and time intervals.

Although 6-keto and 20-HETE exhibit high sensitivity and selectivity for SERS detection with citrated-coated Ag nanoplatelets, attempts to detect similar dilutions of TXB2 were unsuccessful. SERS spectra of different dilutions of TXB2 recorded with citrate-coated Ag platelets exhibit no characteristic peaks that can be confidently assigned to TXB2. Thus, we intend to utilize other high efficiency SERS substrates such as Ag hollow NPs, dendritic structures and nanorods in the future for selective analysis/detection of TXB2.

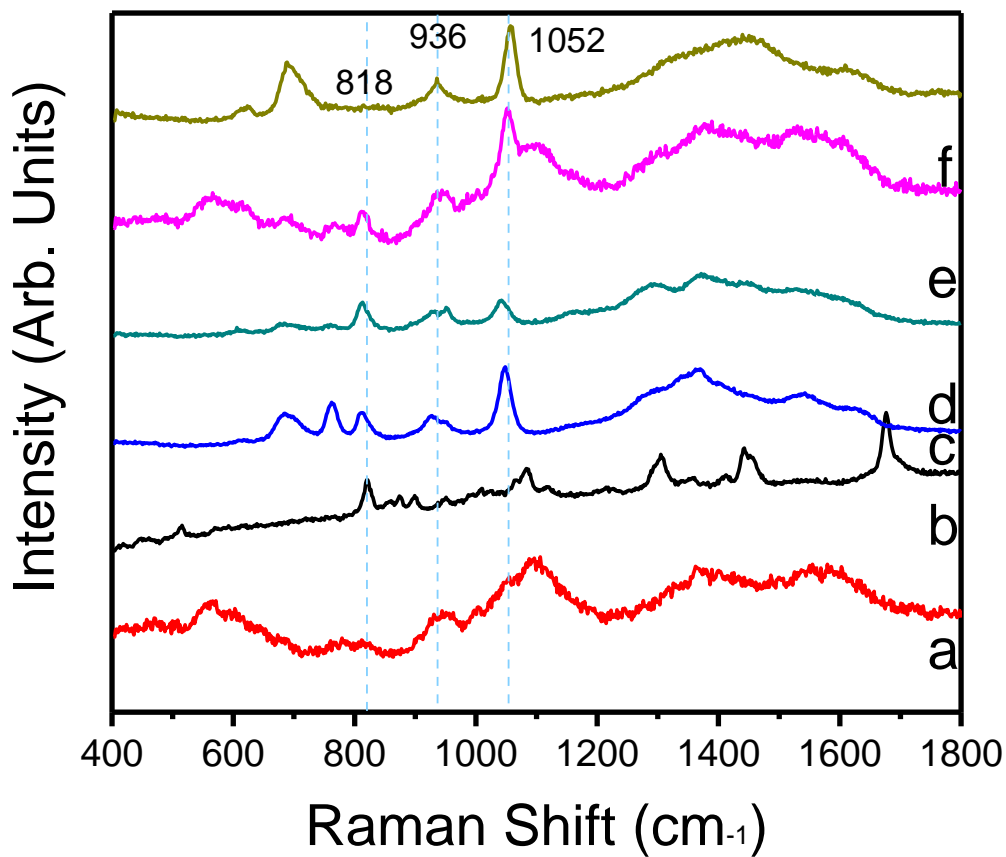


Figure 3.6 (a) Raman spectrum of pure **6-keto prostaglandin-f1a** along with SERS spectra of **6-keto prostaglandin-f1a** acquired with 10 μ L aliquots of (b) 1 mM, (c) 1 μ M, (d) 1 nM, and (e) 1 pM dilutions. Thin films of citrate-coated Ag nanoplatelets were used as the SERS substrates.

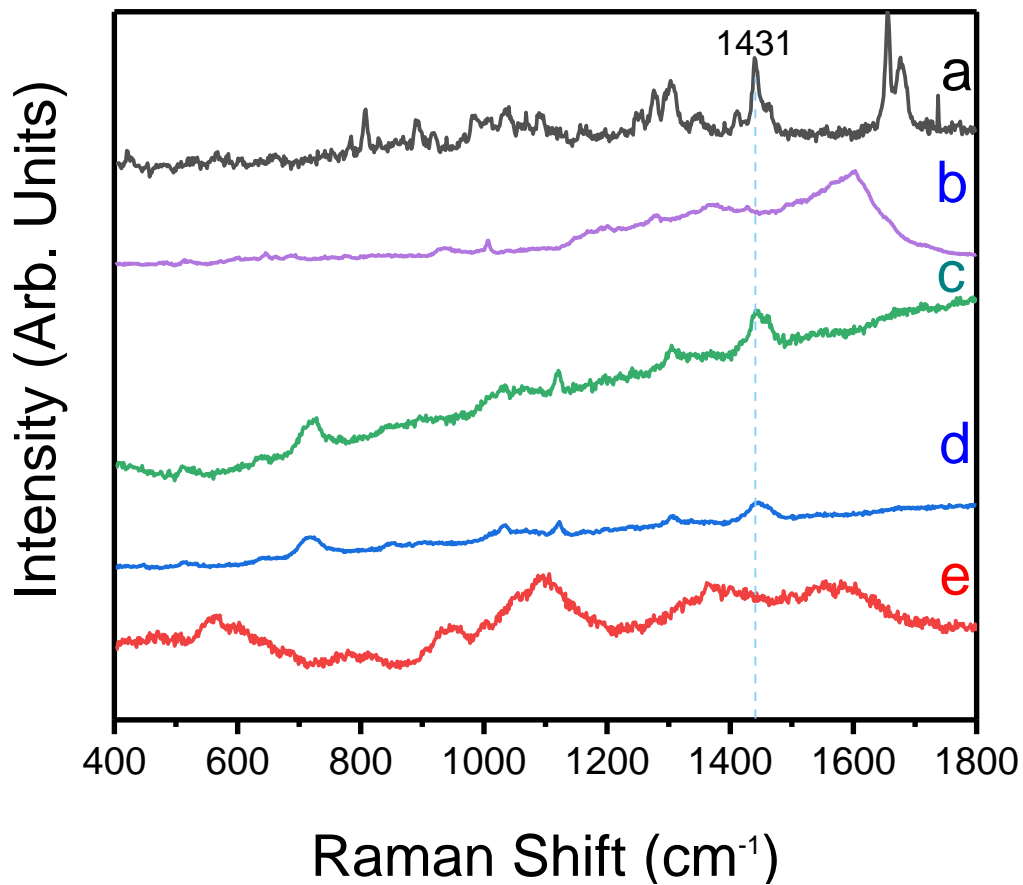


Figure 3.7 (a) Raman spectrum of TXB2 (pure compound) along with SERS spectra of **TXB2** acquired with 10 μL aliquots of (b) 1 mM, (c) 1 μM dilutions. Thin films of citrate-coated Ag nanoplatelets were used as the SERS substrates.

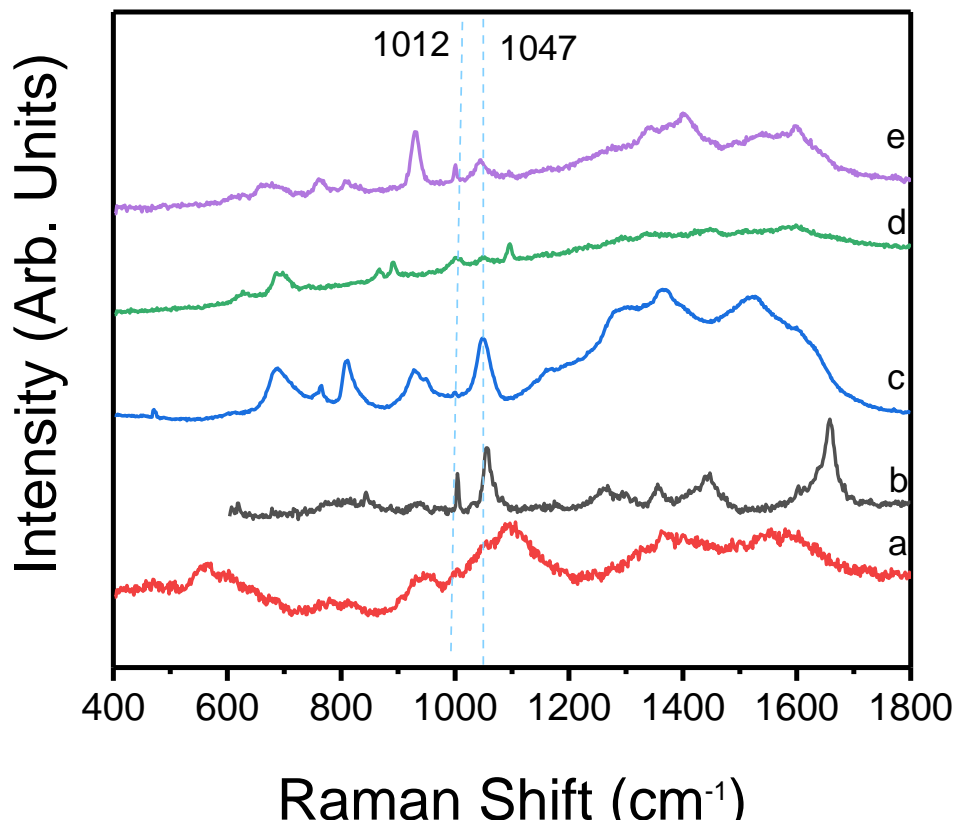


Figure 3.8 (a) Raman spectrum of 20-HETE (pure compound) along with SERS spectra of **20-HETE** acquired with 10 μL aliquots of (b) 1 mM, (c) 1 μM , (d) 1 nM, and (e) 1 pM dilutions. Thin films of citrate-coated Ag nanoplatelets were used as the SERS substrates.

3.8 Peak Assignment and Lipid Stability

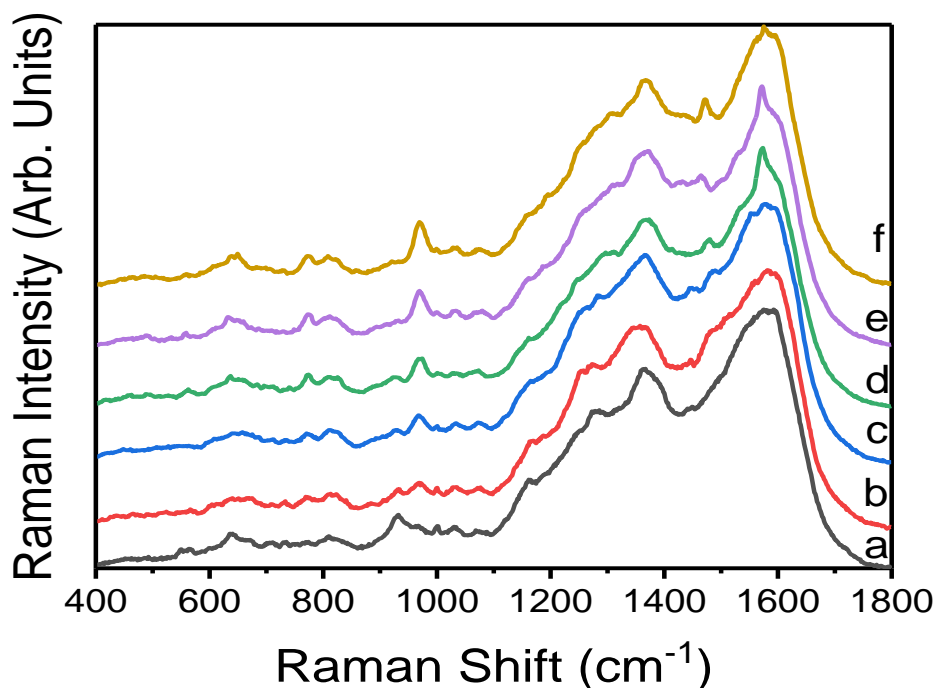


Figure 3.9 The 20-HETE burning study was done on citrate covered triangular silver nanoplatelets, with spectra recorded at the following time intervals: (a) 400s, (b) 800s, (c) 1700s, (d) 2600s, (e) 3500s and (f) 4400s.

In addition to the concentration gradient of 20-HETE done at NCC, a burning study on this lipid was completed as well, for more than one hour of lipid burning. This study (Figure 3.9) was done using the 532.11 nm diode laser with spectra displayed at the following collection times: 400s, 800s, 1700s, 2600s, 3500s and 4400s. These spectra were collected at NCC on the LabRam EvoHR, which showed peaks shifted as compared to the LabRam HR500 used for later studies. In later studies, the peaks referred to as having 1000, 1029 and 1080 cm⁻¹ shifts are found at 1008, 1032 and 1072 cm⁻¹ respectively in this study. This study showed the stability of the 1000 and 1029 cm⁻¹ peaks at 3500s, a longer period of laser exposure than any lipid SERS

studies that were used for concentration gradients of mixing studies found in Chapter 4 of this thesis. The prominent peaks at 976 cm^{-1} and 1450 cm^{-1} in this study were not observed on the physics instrument. The growth of the 1450 cm^{-1} peaks is believed to be broadened in the physics instrument. This peak is attributable to a C-H vibration band in 20-HETE. This may be growing due to dissociation of double bonds in the hydrophobic chain of the lipid, increasing the prevalence of the C-H vibrations. The loss of the shoulder around 1130 cm^{-1} may be due to C-C bond cleavage. The stability of this lipid indicated that there was a possibility of burning other lipids and being left with 20-HETE, making long acquisition periods desirable for this lipid. A TXB2 burning study was also done, but will not be presented in this thesis because it is a very noisy spectrum and though burning was evident due to amorphous carbon growth, but information on other peaks could not be gleaned from this study. The largest takeaway from this study was that 20-HETE is more stable than at least some of the eicosanoids, possibly allowing an avenue of differentiating 20-HETE from them in mixtures. This was not investigated further.

Chapter 4: Applications of Surface Enhanced Raman Scattering Towards the Detection of the Bioactive Lipid: 20-HETE

(Adapted from my publication in ACS Applied Nanomaterials,

DOI: 10.1021/acsanm.8b00840²⁰⁷)

4.1 Experimental Section

4.1.1 Materials. All lipids used in this investigation were purchased from Cayman Chemical Company. Absolute ethanol (200 proof), hydrogen peroxide (30%, stabilized ACS grade), sulfuric acid (ACS grade), poly(styrene sulfonate) (97%, MW=70,000), sodium hydroxide, ethanol (99.8%, extra dry, AcroSeal™), methanol (99+%, extra pure), acetone (ACS grade) and premium glass microscope slides were purchased from Fisher Scientific. Trisodium citrate (99%) was purchased from Acros Organics. L(+)-ascorbic acid (99%) was purchased from Sigma-Aldrich. Sodium borohydride (99.99%) and silver nitrate (99.99%) were purchased from Strem Chemicals. Aluminum pans were purchased from TA Instruments. Milli-Q filtered (EMD Millipore, 18 MΩ) water was used in all syntheses. All chemicals were used as received without further purification.

4.1.2 Synthesis of Citrate-Capped Ag Triangular Nanoplatelets. Ag triangular nanoplatelets were produced in a two-stage synthesis reported by Aherne *et al.*¹⁶⁷ In the first stage, a precursor Ag seed solution is produced by mixing 5.00 mL of trisodium citrate (10 mM), 1.0 mL of sodium borohydride (10 mM), and 0.250 mL poly(styrene sulfonate) (10 mM) in a round bottom flask using a magnetic stirrer. Then, a syringe pump is used to add 5.0 mL of silver nitrate (0.5 mM) at a rate of 2 mL/min to the above mixture. The Ag triangular nanoplatelets were then produced by adding 1.6 mL of seed solution, 1.2 mL of ascorbic acid (10 mM) and 50 mL of deionized water to a round bottom flask with continuous stirring. A syringe pump is used to add 7.50 mL of silver nitrate (0.5 mM) at a rate of 2.5 mL/min. Thirty seconds after the last of the silver nitrate is pumped

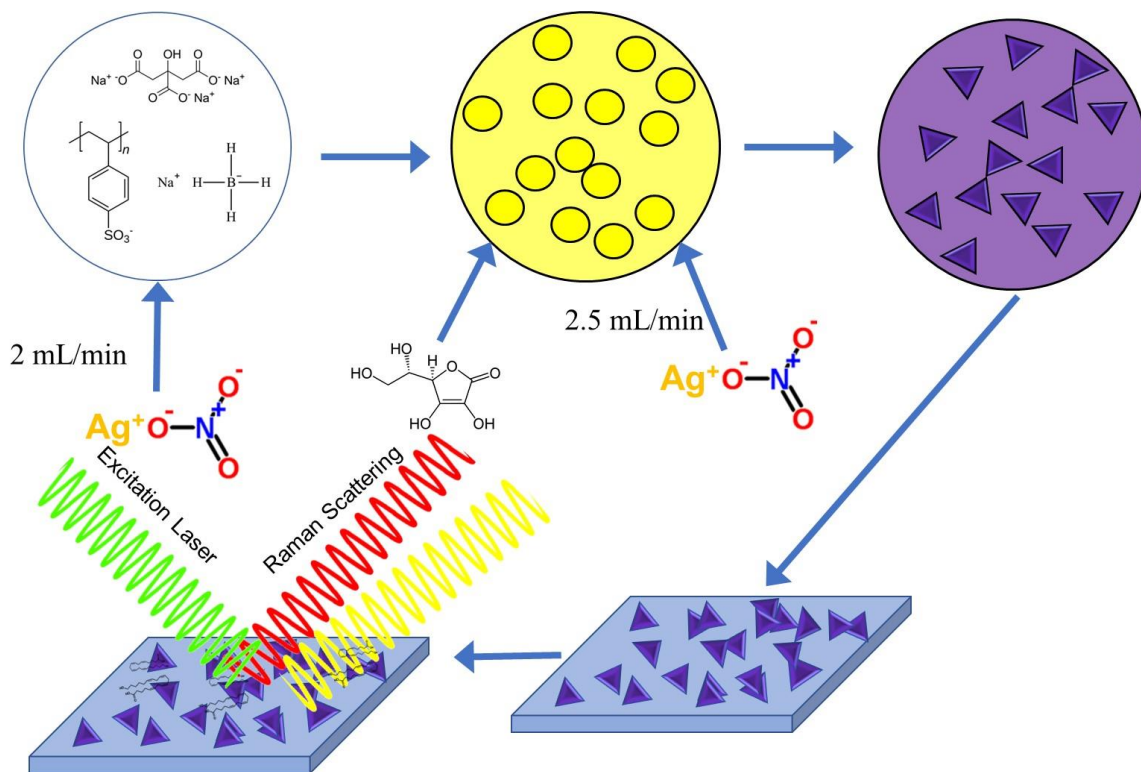
into the vessel, 1.00 mL of 10 mM trisodium citrate is added to the reaction mixture, to ensure full growth of silver platelets and complete surface passivation with the citrate ligands. The solution is then centrifugally filtered to concentrate it to fifty times the native concentration. The visibly purple triangular nanoplatelet solution exhibit a peak of plasmonic absorption at 532 nm with a full width at half max no greater than 70 nm.

4.1.3 Fabrication of SERS Substrates. Glass slides for SERS substrate deposition were carefully cleaned in piranha solution (3:1 concentrated sulfuric acid and 30% hydrogen peroxide), which will destroy any organics found on the glass or its coatings via submersive bath for a minimum of 1 h. *Caution: Piranha solution should be handled with extreme care. It is a very caustic solution and produces caustic vapors upon the initial mixing of sulfuric acid and hydrogen peroxide, and such should only be used in a properly functioning hood while the user is wearing proper personal protective equipment, including thick gloves, a lab coat, and goggles.* Cleaned slides were carefully rinsed in three cycles of adding 100 mL of deionized water to a clean beaker containing the slides and sonicated for 10 min. of sonication. Rinsed slides were then dried in an oven at 130° C for 2 h. The dried slides were then used to drop cast the Ag triangular nanoplatelet solution. After dropping 1 drop of Ag solution, substrates were placed in a vacuum oven and held at -20 mm Hg for 1 h at 25°C. This procedure was repeated five times to have a sufficiently thick layer of Ag platelets. Drop-casted Ag slides were then stored in the vacuum oven at 25°C to reduce oxidation until a maximum of one day before use.

4.1.4 Physical Characterization of Ag Triangular Nanoplatelets. X-ray diffraction patterns (XRD) of Ag samples were recorded using PANalytical powder X-ray diffractometer equipped with a Cu K α radiation. A Nicolet 670 FT-IR instrument equipped with a single-reflection diamond ATR was used to record the infrared (IR) spectra of samples. Transmission electron micrographs (TEM)

were recorded using a Zeiss Model Libra 120 microscope operating at an accelerating voltage of 120 kV. Solution UV-visible absorption spectra of Ag NPs were recorded using a Cary 6000i UV-vis-near IR spectrophotometer in the double beam mode. The reflectance spectra of Ag NPs were acquired using a diffuse reflectance accessory attached to the UV-vis-near IR spectrophotometer using a BaSO₄ background holder and converted to absorption using the Kubelka-Munk remission function.²⁰⁸ A Hitachi SU-70 scanning electron microscope (SEM) and MFD-3D Asylum Research Atomic Force Microscope were used to record SEM and AFM images of Ag nanoplatelets, respectively.

4.1.5 SERS and Raman Data Collection. The SERS analysis of lipids was performed by placing two aliquots of 5.00 μL of analyte dispersed in ethanol on SERS substrate, approximately 0.25 cm each edge on the x-axis and centered on the y-axis, ensuring coverage of the full slide. Raman spectra were collected on pure lipids that were dissolved in ethanol and deposited on aluminum pans. After deposition, 5 min. drying time under ambient air was allowed for the ethanol to evaporate. On humid days, additional drying time was allowed if the characteristic 880 cm^{-1} peak of ethanol was present after the first spectrum was collected. Special care was taken to use only clean gloves and tweezers when moving slides and to avoid all forms of contamination, including breathing on or near the substrate. Raman spectra were collected for 1800 seconds whereas SERS spectra were collected for 900 seconds. All spectra were collected using a Horiba LabRam HR 500 spectrometer equipped with a liquid nitrogen cooled CCD detector and a 532.11 nm diode laser running with LabSpec 4.0 software. For all samples, the grating was set to 800, with a 100 μm slit and 50 μm aperture hole laser power was set to 8 μW and a 100x objective, making a 4.5 μm^2 focused beam spot.



Scheme 4.1. A schematic illustration of the synthesis of Ag triangular nanoplatelets for SERS detection of bioactive lipids.

4.2 Results and Discussion

4.2.1 SERS Substrate Design and Thin Film Fabrication. Fabrication of a suitable plasmonic substrate is of utmost importance for the enhancement of specific SERS signals of an analyte leading to qualitative detection and possibly quantification. Because of their high stability and simplicity of morphological control, Au and Ag nanostructures are commonly used plasmonic metals for SERS application.¹⁸⁷ In this study, elemental Ag was selected as the plasmonic substrate because of its LSPR can be conveniently tuned to match the absorption at the wavelength of the laser excitation (532.11 nm). It is well known that the anisotropic growth of Au and Ag particles

red shifts the LSPR maxima, thus changing the peak maxima of plasmonic absorbance. For instance, Au nanospheres show a plasmon peak at 520 nm.^{209,210} Growth of Au nanospheres into rods, triangles, and dendrites causes the LSPR to red shift past the 532.11 nm excitation, because the plasmon is largely determined by the longest edge length of the nanostructure.⁷³ Minimal anisotropic growth of Au NPs results in red shifting of LSPR past the targeted laser excitation, reducing the SERS signal enhancement with the given laser by minimizing the absorption cross section at that wavelength.^{210,211} In contrast, the 410 nm plasmon of Ag NPs allows for substantial red shifts in LSPR, as a function of nanoparticle anisotropy, thus allowing the LSPR maxima to be tuned to targeted laser excitation (~532 nm).

Another consideration in designing an appropriate SERS substrate is the shape of the plasmonic NPs. The particle shape plays two important roles: tuning of the plasmon and optimization of the plasmonic hot spots. In this study, Ag triangular nanoplatelets were investigated as SERS substrates for lipid analysis. This shape was chosen due to the plasmonic antenna effect.²⁰⁰ The sharper the angles of the particle are, the greater the ability of the particles to focus the enhancement and form more intense Raman hot spots.²⁰⁰ Triangular platelets, in being the regular polygon with the fewest faces, have the greatest antennae effect because it is the only regular three dimensional structure with angles sharper than right angles. Though not all particles in this synthesis had sharp angles, they still provide greater enhancement than spherical Ag NPs do.

A final consideration for SERS study is the intermolecular interactions of the surface functionality of Ag triangular nanoplatelets with the analyte of interest. It is believed that surfactant ligands may help the lipids to be positioned in the plasmonic hot spots of the platelets, while not providing any Raman peaks within the region of the spectrum where the characteristic peaks of

the target lipids are found, so that lipids of interest can be detected unambiguously.¹⁰⁰ Though it is not possible to select a capping ligand without any signal, it is possible to select one that does not interfere with the desired analyte. Additionally, this investigation requires that the 20-HETE biomarker peaks selected to have Raman shifts that are different from the other structurally similar lipids found in blood and plasma. Figure 4.1 shows a Raman spectrum of the substrate. Most lipids have polar heads with long non-polar tails. This leaves two options for selecting a ligand. A non-polar ligand, such as a long aliphatic chain, should interact with the tail of the lipid, causing a large portion of the lipid to be in contact with the plasmonic NPs, theoretically enhancing a greater number of peaks.¹³⁵ The other option is to use a polar capping ligand, such as citrate.²¹² By making a polar surface on the triangular nanoplatelets, the polar head of the lipid should interact with the particle. It was believed that the interactions with the polar head would limit the number of physical arrangements of the lipid on the surface, resulting in more constant and stronger relative enhancement for a limited number of SERS peaks.²¹³ With the goal of attaining the lowest possible LOD, the polar ligands appeared to be a more sensible choice, thus citrate was selected. Citrate is also water soluble, allowing for more environmentally friendly synthesis than nonpolar ligands, which require the use of harsh organic solvents. Figure 4.4E shows a representative TEM image of Ag nanoplatelets with face-centered cubic crystal structure that show a solution-state LSPR maxima at 532 nm with a full width at half maxima no greater than 70 nm (Figure 4.4B). More TEM Images are found in Figure 4.5. In contrast, the drop-casted Ag nanoplatelets show a broader plasmonic resonance from 350-750 nm owing to agglomeration of the particles (Figure 4.4C). TEM images of as-synthesized Ag NPs suggest triangular morphology of platelets with an average edge length of ~40-70 nm (Figure 4.4E). In addition, a few oblong-shaped platelets with rounded

edges and a spherical Ag NPs (10-20 nm) from seed solutions were often observed in as-synthesized samples.

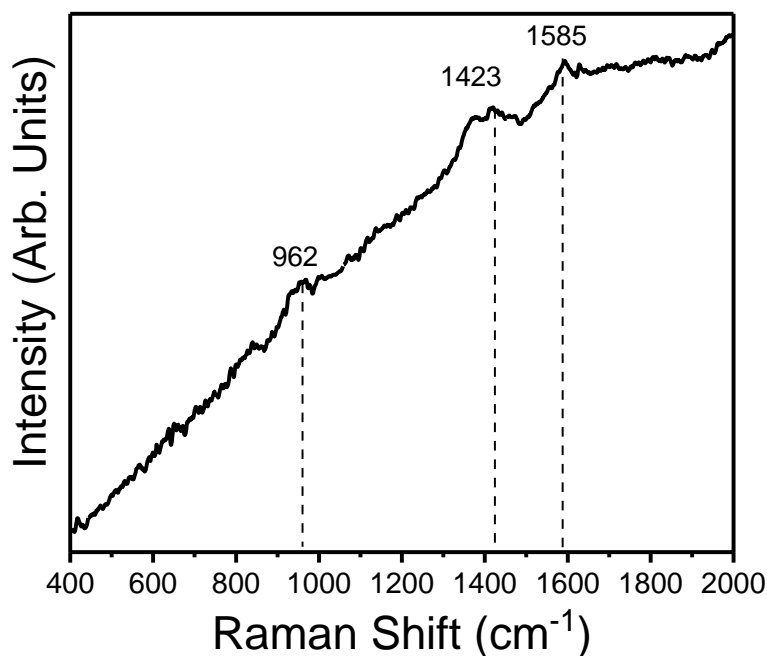


Figure 4.1. Representative SERS spectrum of the Ag nanoplatelet substrate deposited on glass showing that the region between 1000-1100 cm^{-1} does not interfere with 20-HETE peaks in this region of the spectrum.

The morphology and radial distribution of Ag NPs on glass substrates were investigated using AFM and SEM. AFM images show the flat nature of Ag nanoplatelets on the base and top of the particles and an average thickness of 40 nm (Figure 4.4E). Conversely, the SEM images of the Ag NPs deposited on a silicon wafer indicate heterogeneous distribution of the particles and significant variances in thickness of large aggregates on the surface, shown in Figure 4.2. Despite the non-uniformity, SERS were reasonably consistent both in terms of spectral peaks position and

relative peak intensity. Additionally, non-magnified, 10x and 100x visible microscope images show the heterogeneity of the drop-casted substrate (Figure 4.3). The lines and splotches on the slide show aggregates of Ag NPs. The irregularity of the surface is due to the nature of drying high surface tension solvents, such as water, which do not deposit particles homogenously.

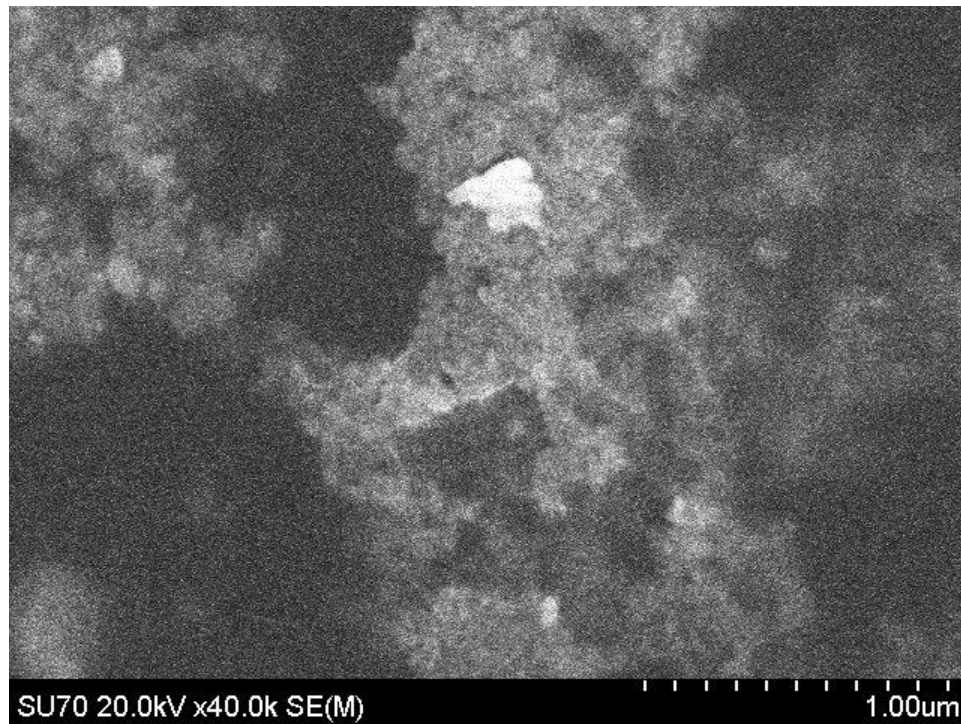


Figure 4.2. SEM image of the Ag nanoplatelet substrate show polydispersity and aggregation of nanoparticles.



Figure 4.3. Photographs showing visible images of drop-cased Ag nanoplatelet substrate with (A) 1X, (B) 10X, and (C) 100X magnification showing randomly distributed and aggregated particles. Despite polydispersity and aggregation on the surface of the coverslip, the Intensity of UV-Vis transmission spectra maintained the same pattern and within 10% transmission for any given wavelength, determined by 5 collected spectra on visible different spots.

A SERS spectrum of the Ag nanoplatelet substrate is shown in Figure 4.1. Ag nanoplatelets show distinct SERS peaks at 962 , 1423 and 1585 cm^{-1} , which can be attributed to surfactants used in NP synthesis. Nonetheless, no peaks were detected in the $1000\text{-}1100\text{ cm}^{-1}$ region of the substrate, where characteristic peaks of targeted lipids are expected to be present. Consistent with SERS spectra, FTIR spectra (Figure 4.4D) of Ag NPs suggest the presence of citrate, and PSS ligands on the surface, which were used as the structure directing to produce triangular Ag platelets.

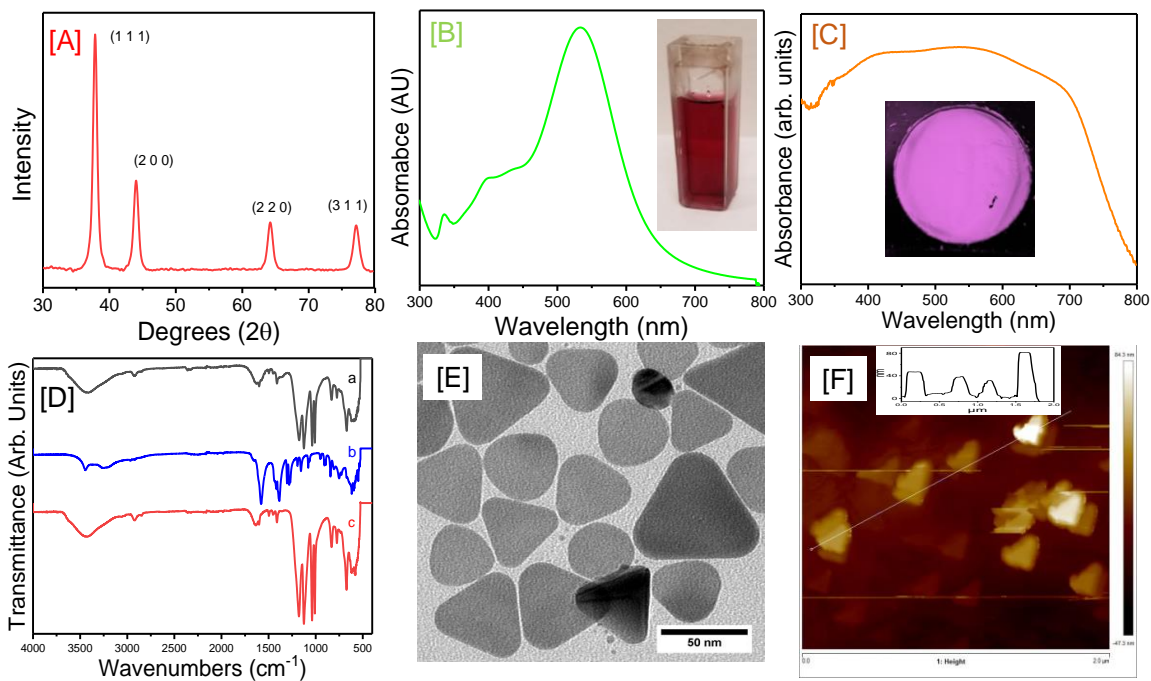


Figure 4.4. (A) Powder XRD pattern, (B) Solution-state and (C) solid-state UV-Visible absorbance spectra and (D) FT- IR spectra of (a) Ag nanoplatelets along with (b) trisodium citrate and (c) poly(styrenesulfonate) surfactants used in the synthesis Ag particles. (E) A representative TEM image of Ag nanoplatelets used in the SERS detection of bioactive lipids. (F) An AFM image of Ag nanoplatelets drop-casted on glass substrates including depth profile.

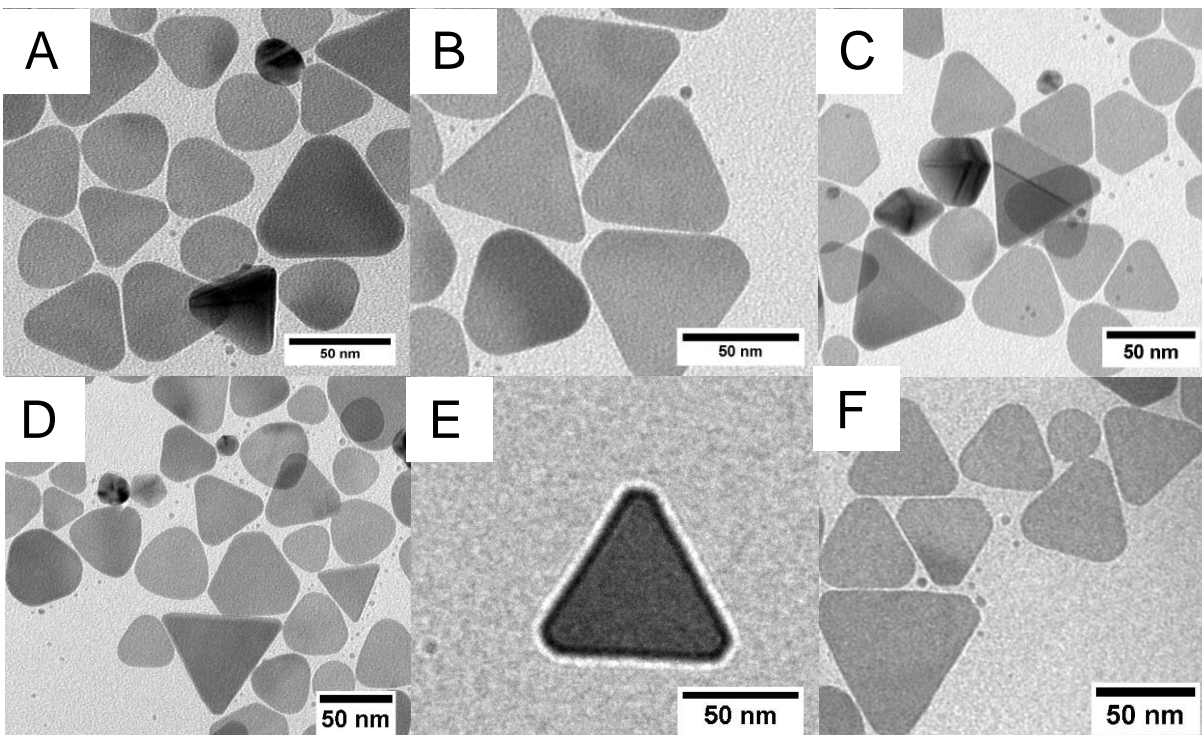


Figure 4.5. TEM Image of triangular Ag nanoplatelets used in the SERS detection of bio-active lipids. Highlights of these images include (A) a representative distribution of triangles with sharp corners, rounded corners and amorphous platelets, (B) similar sized triangular platelets with a narrow size distribution, (C) several sharp colored shapes, (D) three nice triangles with sharp angles, (E) a single platelet of ideal size and (F) a good distribution of particles with varying sizes but consistent shape.

4.2.2 Pure Lipid Spectra of 20-HETE, AA, EPA, and DHA. The normal Raman spectra of pure 20-HETE and selected other lipids obtained by drop-casting a concentrated solution of lipid dissolved in absolute ethanol on aluminum pans are shown in Figure 4.6. These spectra were used as reference patterns for the SERS studies and to identify characteristic molecular vibrations of each lipid without enhancement. Though SERS can cause shifting of peaks, the normal Raman

spectra provide a clear indication, where characteristic peaks of each lipids are expected to occur in the corresponding SERS patterns. Additionally, these spectra indicate which lipids exhibit peaks that could interfere with the target analyte (*i.e.* 20-HETE). It is important to note that Raman spectra of AA, DHA, and EPA show no peaks in the 990-1200 cm^{-1} region (Figure 4.6 B-D). In contrast, 20-HETE exhibits three characteristic peaks at 1000, 1029, and 1080 cm^{-1} , which are believed to be derived from the $\beta_{(\text{C-H})}$ stretch, enabling its selective detection in the presence of other lipid interferents (Figure 4.6A). Since AA, DHA, and EPA have such similar chemical structures, their vibrational spectra are also very similar in nature. With a high enough resolution instrument, these peaks can be differentiated, despite similar vibrational frequencies. The broadening of peaks in the 830-967 cm^{-1} region should allow for these lipids to be detected by decreasing the width of the associated peaks. The peak at 864 cm^{-1} for AA and 840 cm^{-1} for EPA, which are attributed to carboxylic acid (C-O) vibration will not likely be distinguishable. However, the 956 cm^{-1} peak that is believed to originate from the $\beta_{(\text{C-H})}$ vibration of EPA should allow the lipids to be distinguished. DHA has a prominent peak at 830 cm^{-1} that is likely derived from $\beta_{(\text{C-H})}$ vibration, which should distinguish it from the other three lipids. Though this study did not focus on the discernment of all these lipids and focused on 20-HETE, it should be possible for all four lipids to be distinguished in a mixture based on the peaks. The locations of all prominent peaks and their proposed assignments are reported in Table 1. All peak assignments are based on the data provided in a recent review by Czamara *et. al.*¹²⁹

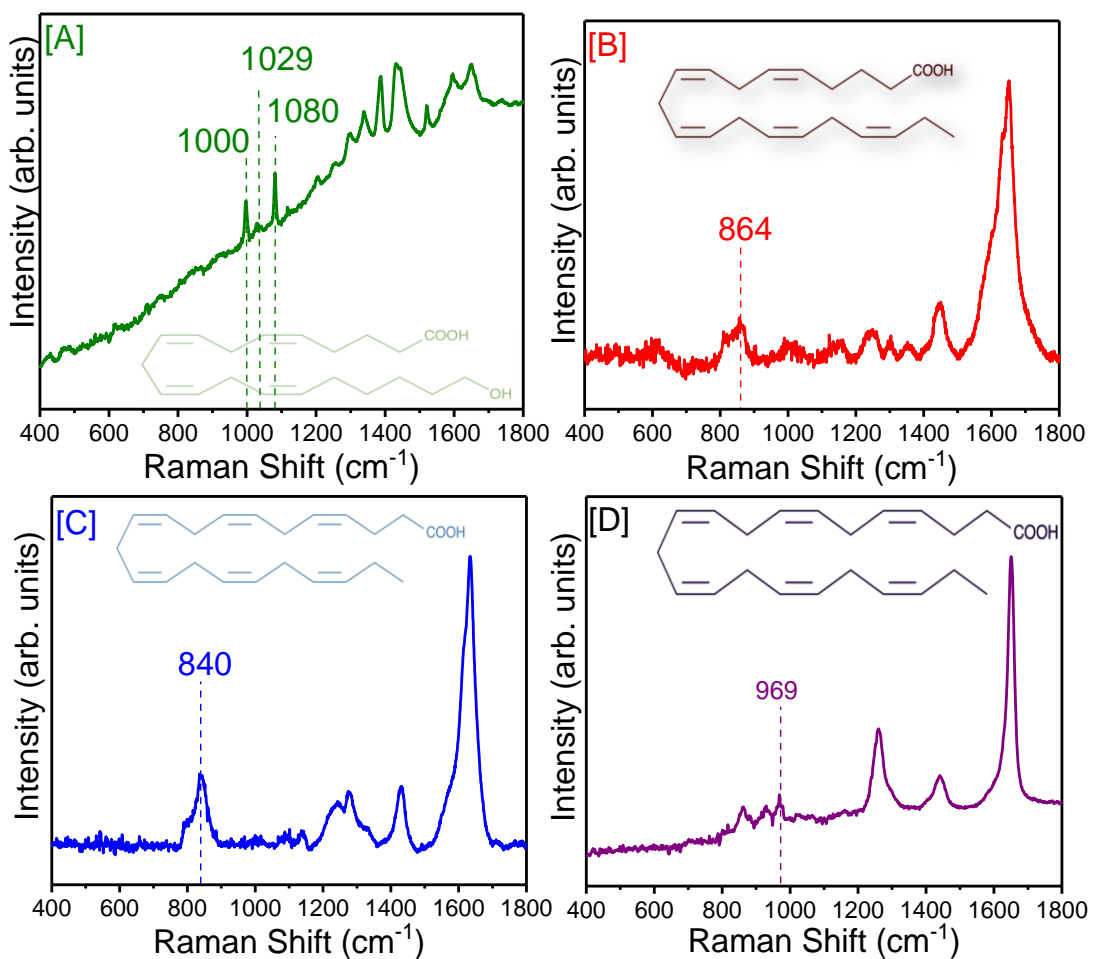


Figure 4.6. Normal Raman spectra of pure lipids and their molecular structures: (A) 20-Hydroxyeicosatetraenoic acid (20-HETE), (B) arachidonic acid (AA), (C) docosahexaenoic acid (DHA), and (D) eicosapentaenoic acid (EPA).

Table 4.1. Raman Peak Assignments of 20-Hydroxyeicosatetraenoic Acid (20-HETE), Arachidonic Acid (AA), Docosahexaenoic Acid (DHA), and Eicosapentaenoic Acid (EPA). Key vibrations Note are α = Scissoring, β = Bending, δ = Deformation, τ = Twisting, and ν = Stretching.

Lipid	Peak Value (cm ⁻¹)	Proposed Associated Vibration
20-HETE	1000	$\beta_{(CH)}$
	1029	$\beta_{(CH)}$
	1080	$\nu_{(C-C)}$
	1295	$\tau_{(CH_2)}$
	1386	$\alpha_{(CH_2/CH_3)}$
	1431	ν_{C-H}
	1521	ν_{C-H}
	1597	ν_{C-H}
	1652	$\nu_{(C=C)}$
AA	864	$\nu_{(C-O)}$
	1450	$\alpha_{(CH_2/CH_3)}$
	1648	$\nu_{(C=C)}$
DHA	840	ν_{C-O}
	1235	$\delta_{(CH)}$
	1283	$\delta_{(CH_2)}$
	1428	$\alpha_{(CH_2/CH_3)}$
	1626	$\nu_{(C=C)}$
EPA	862	$\nu_{(C-O)}$
	928	$\beta_{(CH)}$
	966	$\beta_{(CH)}$
	1262	$\delta_{(CH_2)}$
	1439	$\alpha_{(CH_2/CH_3)}$
	1648	$\nu_{(C=C)}$

For the SERS studies, citrate-capped Ag triangular nanoplatelet substrates drop-cast on glass slides were investigated. Figure 4.7 shows the SERS spectra of four different lipids (20-HETE, AA, DHA, and EPA) collected at different concentrations (1 μ M, 1 nM, and 1 pM) on Ag platelets. Shifting of Raman peaks compared to pure compound spectra was often observed, consistent with prior reports.^{8,96,204,214} It is important to note that all lipids investigated in this

study can be detected down to 1 pM concentrations with citrate-coated Ag triangular nanoplatelets (Figure 4.7 A-D). Interestingly, the highest intensity peaks were visible when spectra were acquired at the lowest concentration studied (1 pM) for all lipids. This increase of the peak intensity and band sharpening is expected to arise from one of two possible phenomena. The first phenomenon arises from the fact that having a lower concentration means that there is a lower probability of direct interactions between analyte molecules, such as dimerization of carboxylic acid groups or crystallization of analyte molecules. These latter situations could lead to heterogeneous environments, with reduced enhancement of specific vibrations arising from isolated molecules.⁸⁶ Furthermore, crystallization can reduce the ability to detect a given analyte. The lower layers of the crystal, which would be in contact with the substrate, can be enhanced, however the Raman scatter might not be able to penetrate upper layers of the lattice, preventing detection.¹⁷⁵ The second possible reason is that lipid micellar structures may be forming in the ethanol-based lipid solution. Since ethanol is a polar protic solvent, entropy considerations will drive the solution to increase interactions between the polar heads while decreasing the interactions between the nonpolar tail of the lipids and the polar solvent.¹³⁸ The structure that best optimizes those interactions would be the formation of micellar structures with the nonpolar tails of the lipids in the center of the aggregate. This aggregation would reduce the probability of lipid molecules finding a hot spot limiting the number of molecules in closed proximity to the substrate surface, leading to minimal analyte being located in a plasmonic hot spot. To mitigate aggregation, vials were vigorously shaken for 30 seconds immediately prior to sample deposition, likely breaking up aggregates and micelles. This produced more uniform spectra throughout a slide, indicating more regular deposition of lipids on the substrate. In contrast, at higher concentrations, the micelles begin to reform nearly instantly due to increased molecular collisions between lipid molecules,

which can likely increase the segregation and lower signal intensity. The unexpected effects on the peak intensity and irregular peak shifting could also be derived from the different SERS enhancement mechanisms at play.

There are two possible mechanisms for enhancement of Raman spectra by NPs. The first, and most commonly discussed is plasmonic enhancement.^{73,84,215,216} Through this avenue of enhancement, the inelastic scattering cross section of the molecules near the roughened surface of plasmonic nanostructures are increased drastically by the electromagnetic field generated by the NPs.^{89,204,205} The free electrons of the metallic nanostructures are collectively excited in a localized surface plasmon resonance (LSPR).²¹⁷ This LSPR creates small, intense electromagnetic fields, which increase the probability of inelastic scattering events, thus increasing the Raman intensity.^{217,218} The second mechanism is charge transfer enhancement (CTE). In CTE, an electron is transferred from the nanostructure to a chemical adsorbed analyte when the Fermi energy level of the NP matches the LUMO energy of the adsorbate and the laser energy.²¹⁹ This induces rapid changes between a lower energy state and a higher energy transfer charge state.^{194,219} This mechanism is not fully understood, but it has been reported to cause enhancement factors (EFs) of up to five orders of magnitude and peak shifting. Both mechanisms can be found in the same system, and both are believed to be present in this study. Plasmonic enhancement does not result in large shifting of peaks. CTE is believed to be present due to the disappearance of the 1652 cm^{-1} peak in the Raman spectra of 20-HETE, the most prominent peak before the NP substrate is introduced. Carboxylic acids tend to deprotonate in ethanol, forming a COO^- terminus on the lipids. It has been previously reported that the COOH of AA binds to silver NPs; thus it is likely that COO^- can bind to the Ag^+ on the surface of the Ag platelets, allowing for CTE.^{91,220}

Identification of 20-HETE in the current study is based on the peaks found at 1000 and 1029 cm^{-1} in the non-enhanced Raman spectrum. The 1000 cm^{-1} Raman peak of 20-HETE is consistently observed in SERS spectra with a three-wavenumber shift to 997 cm^{-1} (Figure 4.7A). The 1029 cm^{-1} peak of 20-HETE is observed in all characteristic spectra without shifting. These peaks likely arise from the $\beta_{(\text{C-H})}$ frequency of 20-HETE. For AA, the $\beta_{(\text{C-H})}$ vibration appears at 974 cm^{-1} in the pure lipid and is red shifted to 930 cm^{-1} in the SERS spectra (Figure 4.7 B). The 1049 cm^{-1} peak of AA can be attributed to C-C vibrations. The 1649 cm^{-1} in the Raman spectrum of DHA likely downshifts to 1597 cm^{-1} in the SERS spectra and the $\beta_{(\text{C-H})}$ band likely shifts from 969 cm^{-1} to 959 cm^{-1} in the SERS spectra (Figure 4.7 C). In EPA, the $\beta_{(\text{C-H})}$ band is observed at 969 cm^{-1} in both the Raman spectrum and the SERS spectra (Figure 4.7 D). The 1442 cm^{-1} peak is likely an $\alpha_{(\text{CH}_2)}$ vibration, which downshifts to 1440 cm^{-1} in the SERS spectra.³⁵ The characteristic peaks of 20-HETE in the aforementioned spectra are discernable in approximately 72% of the collected spectra in this study.

Table 4.2: Quantitate Analysis of Targeted Lipids Detection using Drop-Casted Ag Nanoplatelet Substrates that show the Reproducibility and Statistical Significance.

Lipid	Number of Spectra Taken	Number of Spectra without Human Error, Instrument Error/ Solar Flares	Number of Spectra where the targeted lipid detectible based on biomarker peaks	% Reproducibility
20-HETE	472	446	371	83.1%
Arachidonic Acid	356	340	229	67.4%
Docosahexaenoic Acid	179	162	89	54.9%
Eicosapentaenoic Acid	103	88	57	64.8%
Total Spectra	1110	1036	746	72.0%

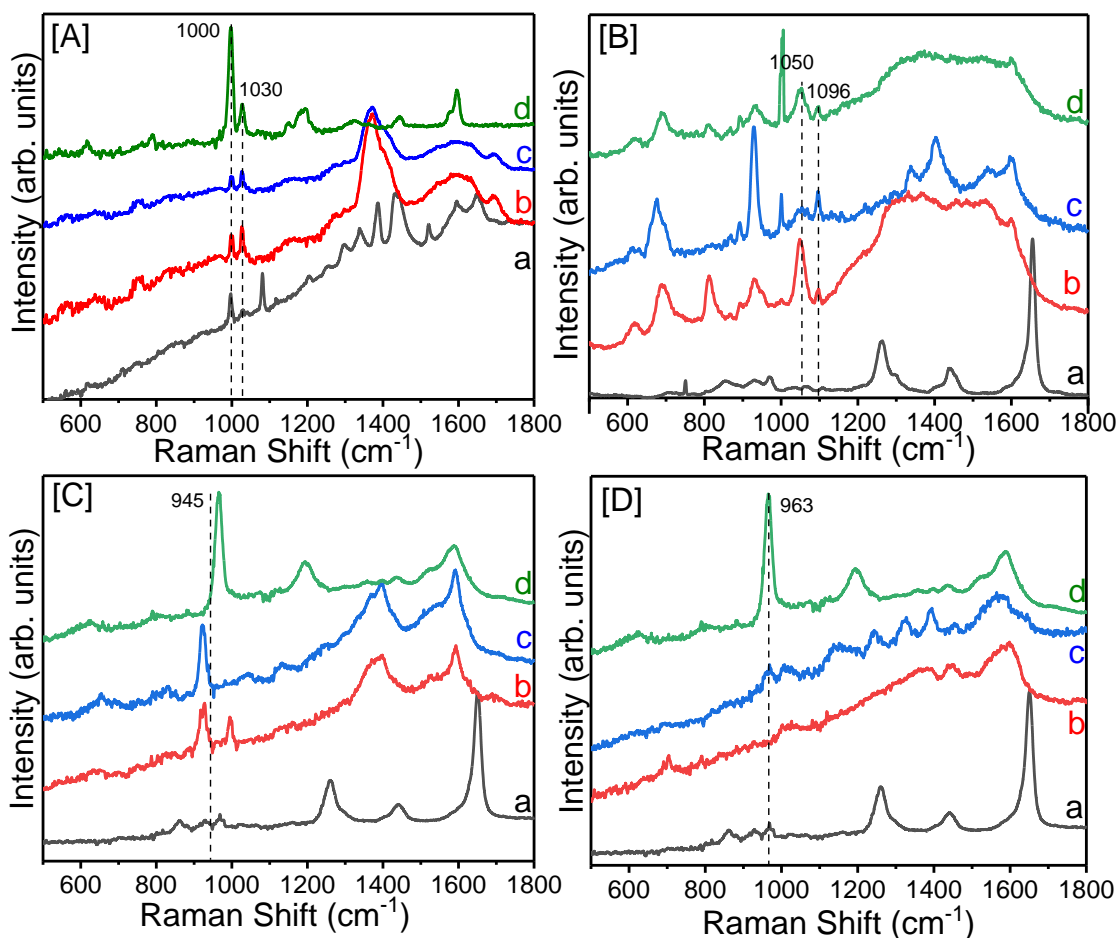


Figure 4.7. (a) Raman spectra and (b) 1 μM SERS, (c) 1 nM SERS, and (d) 1 pM SERS spectra of (A) 20-HETE, (B) AA, (C) DHA and (D) EPA. The dash lines of each spectrum indicate the significant peaks that were used for qualitative analysis corresponding lipids in mixing studies.

To investigate the selective detection of 20-HETE in the presence of other interfering, structurally similar lipids, mixing studies were performed with varying ratios of AA, EPA, DHA, and 20-HETE. Specifically, 1 pM 20-HETE was mixed with the interfering lipids at varying concentrations, with reported values for every three orders of magnitude, starting with 10^{-6} M (1 μM , 1nM, and 1 pM) and SERS spectra were taken on drop-casted Ag triangular nanoplatelets.

The SERS spectra of these four lipids of interest provided further evidence that the peaks near 1000 cm^{-1} and 1029 cm^{-1} for 20-HETE were specific to that lipid. This specificity allowed for selective detection of 20-HETE in mixtures even when the other lipids (AA, EPA, and DHA) were present at significantly higher concentrations (Figure 4.8-10). Though the 1000 cm^{-1} peak can be argued to be due to AA, but the 1029 cm^{-1} peak can only be attributed to 20-HETE, further confirming the presence of 20-HETE. Thus, these mixed lipid studies show that the biomarker peaks for 20-HETE are distinguishable, even with the structurally similar lipid interferences at concentrations three orders of magnitude greater than that of 20-HETE (Figure 4.8-10).

To demonstrate the potential clinical relevance of SERS for selective analysis of targeted lipid, all four lipids were mixed in concentrations similar to their biological levels in plasma (Figure 4.11). The solution consisted of $4.56\text{ }\mu\text{M}$ AA, 821.1 nM DHA, 129 nM EPA, and 86.7 nM 20-HETE in absolute ethanol, based on values from the Human Metabolome Database.²²¹ In the corresponding SERS spectra, characteristic 20-HETE peaks are still distinguishable at 1000 and 1030 cm^{-1} . The broadening of the 20-HETE peaks is likely caused by the intermolecular interactions of the analyte with other lipids, causing variations in the frequency of the molecular vibrations. The intense and broad peaks found from $866\text{-}960\text{ cm}^{-1}$ are a combination of peaks from the substrate, $\beta_{(\text{C-H})}$, and $\nu_{(\text{C-O})}$ vibrations of AA, DHA and EPA. The low intensity, broad region from 1500 to 1750 cm^{-1} is due to amorphous carbon growth that results from the burning of lipids. These carbon peaks can be seen growing in intensity as time elapses during a given spectral collection, indicating burning of lipids due to energy imparted by the laser.

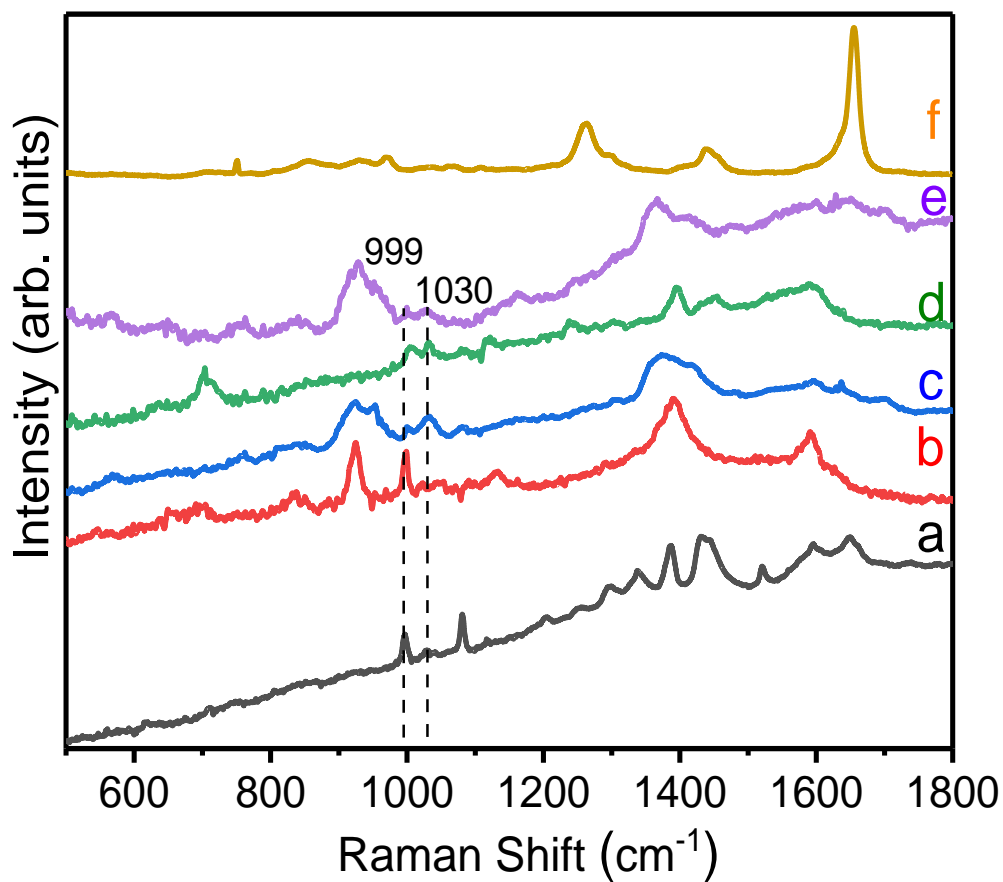


Figure 4.8. (a) Raman spectrum of 20-HETE along with SERS spectra of (b) 1 nM AA and 1 nM 20-HETE, (c) 1 nM AA and 100 pM 20-HETE, (d) 1 nM AA and 10 pM 20-HETE, (e) 1 nM AA and 1 pM 20-HETE and (f) Raman spectrum of AA. These data suggest that 20-HETE is still detectable in the presence of AA with three orders of magnitude higher concentration. The highlighted region indicates the prominent 20-HETE peaks.

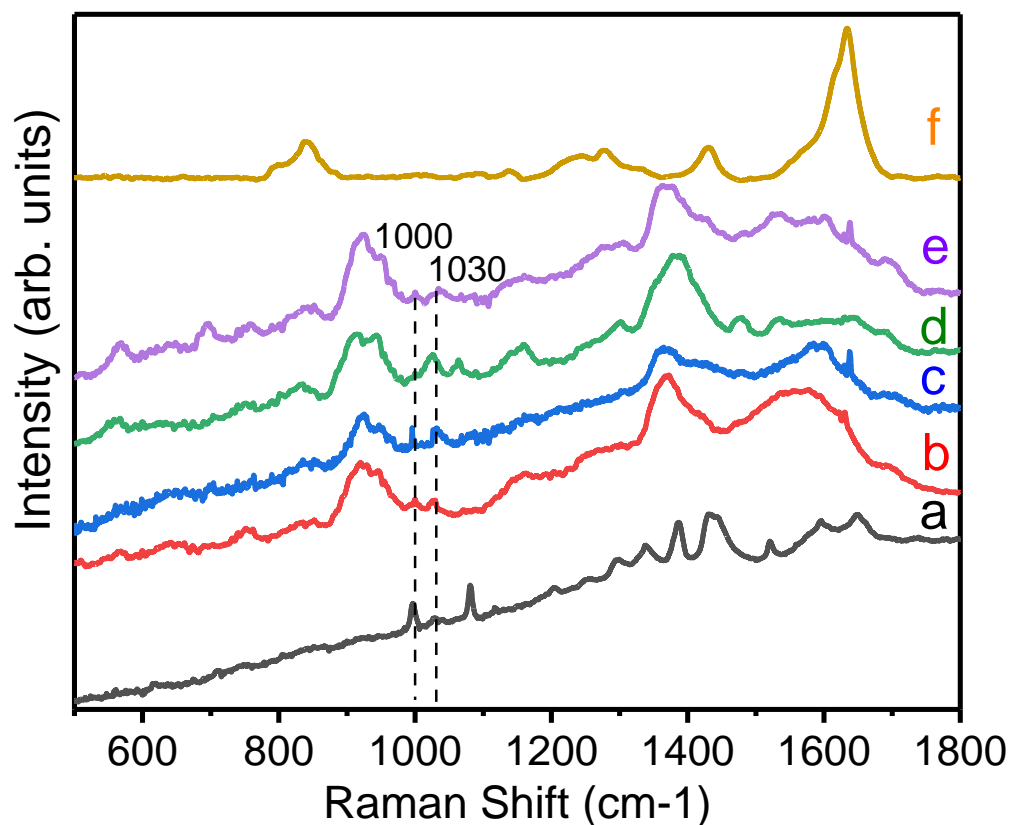


Figure 4.9. (a) Raman spectrum of 20-HETE along with SERS spectra of (b) 1 nM DHA and 1 nM 20-HETE, (c) 1 nM DHA and 100 pM 20-HETE, (d) 1 nM DHA and 10 pM 20-HETE, (e) 1 nM DHA and 1 pM 20-HETE and (f) Raman spectrum of DHA. These data suggest that 20-HETE is detectable in the presence of DHA with three orders of magnitude higher concentration. The highlighted region indicates the prominent 20-HETE peaks.

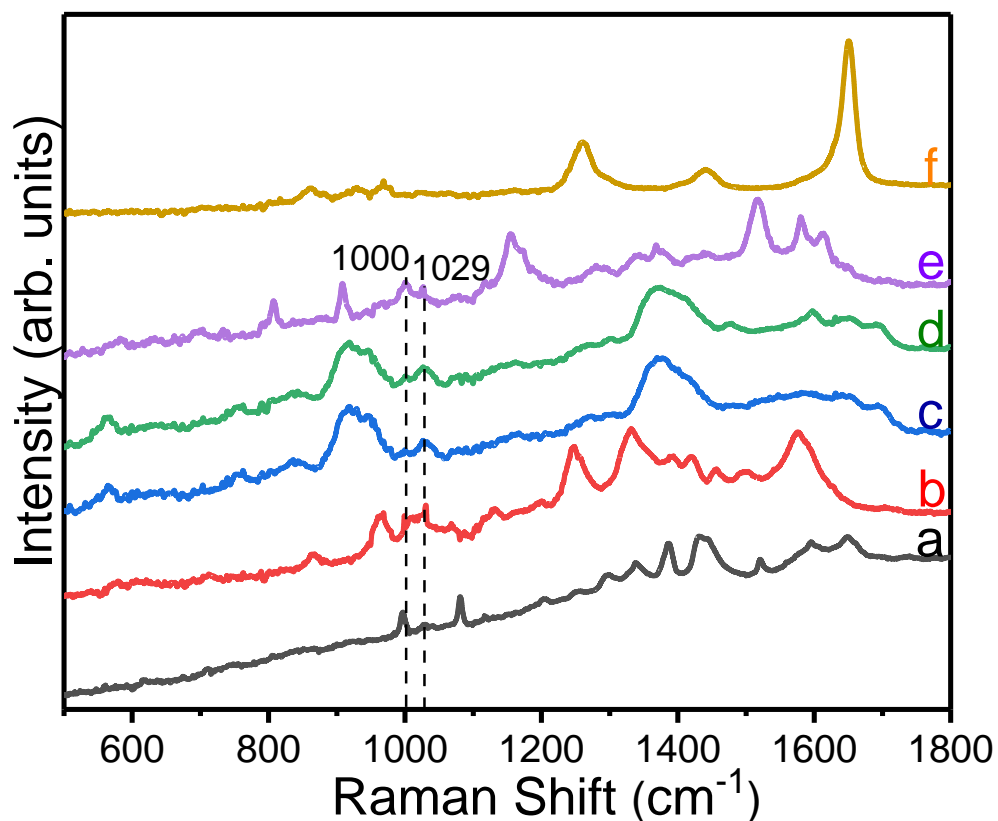


Figure 4.10. (a) Raman spectrum of 20-HETE along with SERS spectra of (b) 1 nM EPA and 1 nM 20-HETE, (c) 1 nM EPA and 100 pM 20-HETE, (d) 1 nM EPA and 10 pM 20-HETE, (e) 1 nM EPA and 1 pM 20-HETE and (f) Raman spectrum of EPA. This data suggests that 20-HETE is detectable in the presence of EPA with three orders of magnitude higher concentration. The highlighted region indicates the prominent 20-HETE peaks.

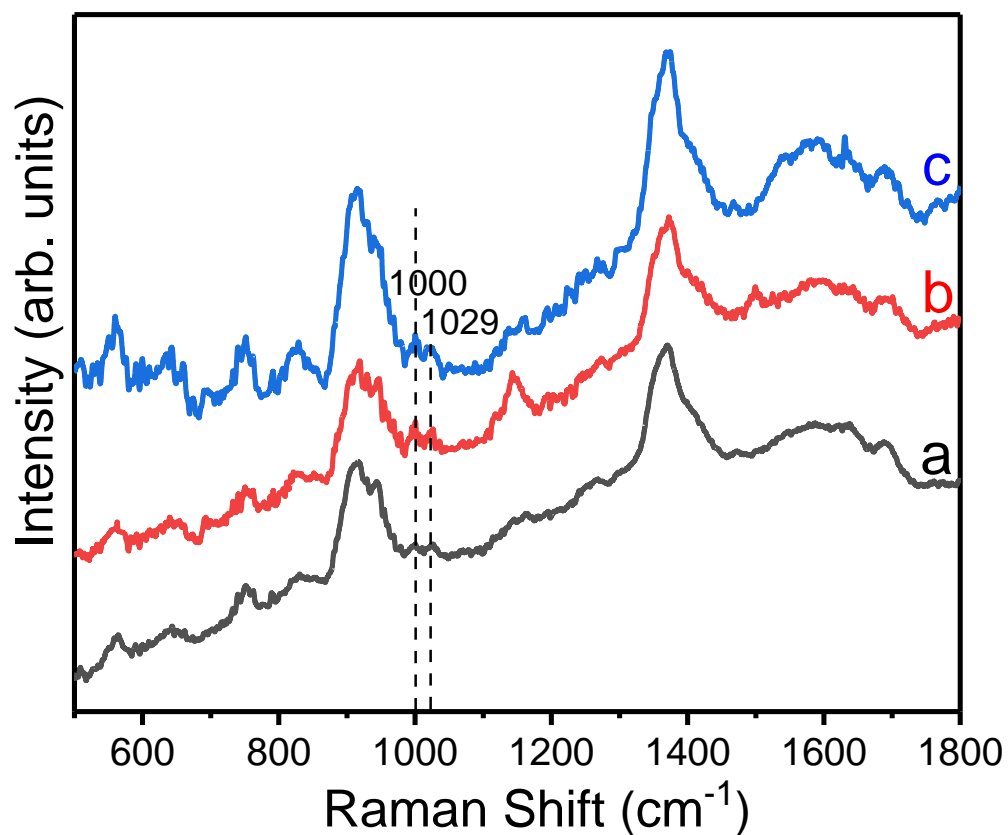


Figure 4.11. (a-c) SERS spectra of a mixture of 4.56 μM AA, 821.1 nM DHA, 129 nM EPA, and 86.7 nM 20-HETE, demonstrating that at biologically relevant concentrations of these lipids, 20-HETE can still be reproducibly detected and differentiated from other lipids. The highlighted region indicates the prominent 20-HETE peaks.

Chapter 5: Conclusions

Initial studies provided several valuable insights into SERS detection of the lipids associated with preeclampsia development. The characteristic SERS peaks of 6-keto prostaglandin- $f_{1\alpha}$ are found in different regions of the spectrum with octanethiol-coated Au nanoparticles, as compared to citrate-coated Ag nanoplatelets. It was believed that the hydrophobic interactions between the lipids and octanethiol would increase the likelihood of the nonpolar tails of the lipids to be drawn into the hot spots when compared to the hydrophilic interactions between the lipid and citrate-covered particles. Conversely, it was observed that silver nanoplatelets were still more advantageous for this application because enhancement from the sharp angles outweighed the potential detriment of having a polar capping ligand. Furthermore, one can observe that the shape of the lipid associated peaks at 1 nM and 1 pM concentrations are drastically different from those at 1 μ M and 1 mM concentrations. This is believed to be due to the ability of lipids to aggregate and crystalize. In more dilute samples, it is assumed that the molecules are not interacting with each other as much and cannot crystalize as easily, leading to individual molecules being detected as opposed to aggregated crystals interacting with the hot spots in higher concentrations. Later, a hypothesis concerning micelle formation was developed, giving more insight into the different peak shapes and intensities at varying concentrations. Additionally, it was observed that TXB2 does not generate distinguishing peaks with the citrate-coated Ag platelets. This may be due to interactions between the lipid and the substrate itself. Based on this study, both 6-keto and 20-HETE can be detected down to 1 pM levels using Ag nanoplatelets with high a low enough limit of detection to be clinically prevalent.

Surface enhanced Raman spectroscopy further demonstrated its potential to be a diagnostic tool for clinicians to use for detection of hypertensive disorders, such as preeclampsia

development, which was further evidenced by more meticulous 20-HETE studies. The low limit of detection makes it ideal for studies of analytes at biologically relevant concentrations, having demonstrated the ability to detect 1 pM concentrations of relevant lipids. In being a “fingerprinting technique,” it provides sufficiently unique patterns for the differentiation of various biomolecules to allow sensitive instruments to differentiate between structurally similar metabolites. It was demonstrated that 20-HETE, AA, DHA and EPA can be reproducibly detected down to 1 pM level using drop cast Ag nanoplatelet SERS substrates. Moreover, selective identification of 20-HETE can be done even in the presence of structurally similar lipid interferences (*i.e.* AA, DHA, and EPA) with concentrations three orders of magnitude greater than that of 20-HETE. In biological concentrations, 20-HETE can be distinguished from AA, DHA, and EPA, the three structurally similar lipids found in greater native concentration than the target analyte in human plasma. It should also be noted that these data were collected with multiple individually prepared SERS substrates and spectra were collected on different times of the day to validate the reproducibility of results. To improve the system for medical diagnostic analysis, the substrate should be made monodisperse to give quantitative analysis capabilities, ideally through lithography. This study has shown the viability of SERS as a potential diagnostic technique for detection of the increased 20-HETE levels associated with blood pressure related conditions, showing viability for this technique to be used to diagnose hypertension disorders.

To carry this work forward toward clinical applications, several steps must still be taken. First, a monodisperse substrate should be made. Second, all lipids found in human plasma should be investigated, both individual and mixed together. Key lipids would include the eicosanoids, eicosatetraenoic acids and the other hydroxyeicosatetraenoic acids. After that, human plasma would need to be investigated, and a method of removing interferences, such as the carotenoid

proteins, would be desired. Additionally, other laser wavelengths should be investigated to see if shorter wavelengths can increase scattering and decrease luminescence further. A 380 nm InGaN diode would be interesting to contrast to 532.11 nm, green diode laser. Lastly, an inclusive device would need to be developed for clinical simplicity.

Theoretically, an instrument in which blood samples could be directly added would reduce the risk of misdiagnosis. This device would need to include an apparatus for doing an ethanol extraction from blood, removing the lipids and removing any platelets, cells and non-ethanol soluble proteins. The solution could then use size exclusion high performance liquid chromatography (SE-HPLC), allowing lipids to pass through while removing any remain proteins. At this point, a perfect system would inject an internal standard and mix it in to verify quantification by the system. After this, two possible methods of automated SERS detection seem plausible. The first involves a system of using an autosampler to deposit the sample onto the substrate. After analysis, the substrate would be cleaned by either a high-pressure solvent washing or else must be replaced. Another option would be to develop a through flow SERS system with a uniform substrate coating inside of tubing with a reflective interior. This would allow a beam to be passed through the sample and gather scattering data. After the sample is analyzed, a solvent flush would have to be done to remove any analytes on the substrate. Though the first system would be simpler, the second should allow for superior reproducibility because the same substrate would be used for a greater period. Finally, the analysis software would have to be programmed to calculate the concentration of each lipid in the sample.

References

- (1) Bergou, J. A.; Englert, B.-G. Heisenberg's Dog and Quantum Computing. *J. Mod. Opt.* **1998**, *45* (4), 701–711.
- (2) Stix, G. Little Big Science. *Sci. Am.* **2001**, *285* (3), 32–37.
- (3) Aragay, G.; Pons, J.; Merkoçi, A. Recent Trends in Macro-, Micro-, and Nanomaterial-Based Tools and Strategies for Heavy-Metal Detection. *Chem. Rev.* **2011**, *111* (5), 3433–3458.
- (4) Jin, R.; Cao, Y. C.; Hao, E.; Métraux, G. S.; Schatz, G. C.; Mirkin, C. A. Controlling Anisotropic Nanoparticle Growth through Plasmon Excitation. *Nature* **2003**, *425* (6957), 487.
- (5) Baffou, G.; Quidant, R.; Girard, C. Heat Generation in Plasmonic Nanostructures: Influence of Morphology. *Appl. Phys. Lett.* **2009**, *94* (15), 153109.
- (6) He, J.; Ichinose, I.; Kunitake, T.; Nakao, A.; Shiraishi, Y.; Toshima, N. Facile Fabrication of Ag–Pd Bimetallic Nanoparticles in Ultrathin TiO₂-Gel Films: Nanoparticle Morphology and Catalytic Activity. *J. Am. Chem. Soc.* **2003**, *125* (36), 11034–11040.
- (7) Joo, S. H.; Park, J. Y.; Tsung, C.-K.; Yamada, Y.; Yang, P.; Somorjai, G. A. Thermally Stable Pt/Mesoporous Silica Core–Shell Nanocatalysts for High-Temperature Reactions. *Nat. Mater.* **2009**, *8* (2), 126.
- (8) Joo, T. H.; Kim, K.; Kim, M. S. Surface-Enhanced Raman Scattering (SERS) of 1-Propanethiol in Silver Sol. *J. Phys. Chem.* **1986**, *90* (22), 5816–5819.
- (9) Zhang, S.; Zhang, X.; Jiang, G.; Zhu, H.; Guo, S.; Su, D.; Lu, G.; Sun, S. Tuning Nanoparticle Structure and Surface Strain for Catalysis Optimization. *J. Am. Chem. Soc.* **2014**, *136* (21), 7734–7739.

- (10) Gilbert, B.; Huang, F.; Zhang, H.; Waychunas, G. A.; Banfield, J. F. Nanoparticles: Strained and Stiff. *Science* **2004**, *305* (5684), 651–654.
- (11) Pettibone, J. M.; Cwiertny, D. M.; Scherer, M.; Grassian, V. H. Adsorption of Organic Acids on TiO₂ Nanoparticles: Effects of PH, Nanoparticle Size, and Nanoparticle Aggregation. *Langmuir* **2008**, *24* (13), 6659–6667.
- (12) Albanese, A.; Chan, W. C. Effect of Gold Nanoparticle Aggregation on Cell Uptake and Toxicity. *ACS Nano* **2011**, *5* (7), 5478–5489.
- (13) Alivisatos, A. P. Semiconductor Clusters, Nanocrystals, and Quantum Dots. *science* **1996**, *271* (5251), 933–937.
- (14) Michalet, X.; Pinaud, F. F.; Bentolila, L. A.; Tsay, J. M.; Doose, S.; Li, J. J.; Sundaresan, G.; Wu, A. M.; Gambhir, S. S.; Weiss, S. Quantum Dots for Live Cells, in Vivo Imaging, and Diagnostics. *science* **2005**, *307* (5709), 538–544.
- (15) Takagahara, T.; Takeda, K. Theory of the Quantum Confinement Effect on Excitons in Quantum Dots of Indirect-Gap Materials. *Phys. Rev. B* **1992**, *46* (23), 15578.
- (16) Wilson, W. L.; Szajowski, P. F.; Brus, L. E. Quantum Confinement in Size-Selected, Surface-Oxidized Silicon Nanocrystals. *Science* **1993**, *262* (5137), 1242–1244.
- (17) Wise, F. W. Lead Salt Quantum Dots: The Limit of Strong Quantum Confinement. *Acc. Chem. Res.* **2000**, *33* (11), 773–780.
- (18) Astratov, V. N.; Bogomolov, V. N.; Kaplyanskii, A. A.; Prokofiev, A. V.; Samoilovich, L. A.; Samoilovich, S. M.; Vlasov, Y. A. Optical Spectroscopy of Opal Matrices with CdS Embedded in Its Pores: Quantum Confinement and Photonic Band Gap Effects. *Il Nuovo Cimento D* **1995**, *17* (11–12), 1349–1354.

- (19) Miller, D. A. B.; Chemla, D. S.; Damen, T. C.; Gossard, A. C.; Wiegmann, W.; Wood, T. H.; Burrus, C. A. Electric Field Dependence of Optical Absorption near the Band Gap of Quantum-Well Structures. *Phys. Rev. B* **1985**, *32* (2), 1043.
- (20) Antonov, L.; Nedeltcheva, D. Resolution of Overlapping UV–Vis Absorption Bands and Quantitative Analysis. *Chem. Soc. Rev.* **2000**, *29* (3), 217–227.
- (21) Arakawa, Y.; Sakaki, H. Multidimensional Quantum Well Laser and Temperature Dependence of Its Threshold Current. *Appl. Phys. Lett.* **1982**, *40* (11), 939–941.
- (22) Anderson, B. P.; Kasevich, M. A. Macroscopic Quantum Interference from Atomic Tunnel Arrays. *Science* **1998**, *282* (5394), 1686–1689.
- (23) Bryant, G. W. Excitons in Quantum Boxes: Correlation Effects and Quantum Confinement. *Phys. Rev. B* **1988**, *37* (15), 8763.
- (24) Miller, D. A.; Chemla, D. S.; Damen, T. C.; Gossard, A. C.; Wiegmann, W.; Wood, T. H.; Burrus, C. A. Band-Edge Electroabsorption in Quantum Well Structures: The Quantum-Confined Stark Effect. *Phys. Rev. Lett.* **1984**, *53* (22), 2173.
- (25) Eidelman, S.; Hayes, K. G.; Olive, K. ea; Aguilar-Benitez, M.; Amsler, C.; Asner, D.; Babu, K. S.; Barnett, R. M.; Beringer, J.; Burchat, P. R. Review of Particle Physics. *Phys. Lett. B* **2004**, *592* (1–4), 1–5.
- (26) Zumbusch, A.; Holtom, G. R.; Xie, X. S. Three-Dimensional Vibrational Imaging by Coherent Anti-Stokes Raman Scattering. *Phys. Rev. Lett.* **1999**, *82* (20), 4142.
- (27) Katsnelson, M. I. Graphene: Carbon in Two Dimensions. *Mater. Today* **2007**, *10* (1–2), 20–27.
- (28) Green, M. A. Third Generation Photovoltaics: Solar Cells for 2020 and Beyond. *Phys. E Low-Dimens. Syst. Nanostructures* **2002**, *14* (1–2), 65–70.

- (29) Im, J.-H.; Lee, C.-R.; Lee, J.-W.; Park, S.-W.; Park, N.-G. 6.5% Efficient Perovskite Quantum-Dot-Sensitized Solar Cell. *Nanoscale* **2011**, *3* (10), 4088–4093.
- (30) Arachchige, I. U.; Brock, S. L. Highly Luminescent Quantum-Dot Monoliths. *J. Am. Chem. Soc.* **2007**, *129* (7), 1840–1841.
- (31) Arachchige, I. U.; Brock, S. L. Sol–Gel Methods for the Assembly of Metal Chalcogenide Quantum Dots. *Acc. Chem. Res.* **2007**, *40* (9), 801–809.
- (32) Nahar, L.; Farghaly, A. A.; Esteves, R. J. A.; Arachchige, I. U. Shape Controlled Synthesis of Au/Ag/Pd Nanoalloys and Their Oxidation-Induced Self-Assembly into Electrocatalytically Active Aerogel Monoliths. *Chem. Mater.* **2017**, *29* (18), 7704–7715.
- (33) Canham, L. T. Silicon Quantum Wire Array Fabrication by Electrochemical and Chemical Dissolution of Wafers. *Appl. Phys. Lett.* **1990**, *57* (10), 1046–1048.
- (34) Grätzel, M. Photoelectrochemical Cells. *nature* **2001**, *414* (6861), 338.
- (35) Chun, W.-J.; Ishikawa, A.; Fujisawa, H.; Takata, T.; Kondo, J. N.; Hara, M.; Kawai, M.; Matsumoto, Y.; Domen, K. Conduction and Valence Band Positions of Ta₂O₅, TaON, and Ta₃N₅ by UPS and Electrochemical Methods. *J. Phys. Chem. B* **2003**, *107* (8), 1798–1803.
- (36) Koffyberg, F. P.; Benko, F. A. A Photoelectrochemical Determination of the Position of the Conduction and Valence Band Edges of P-type CuO. *J. Appl. Phys.* **1982**, *53* (2), 1173–1177.
- (37) Brus, L. Electronic Wave Functions in Semiconductor Clusters: Experiment and Theory. *J. Phys. Chem.* **1986**, *90* (12), 2555–2560.
- (38) Bruchez, M.; Moronne, M.; Gin, P.; Weiss, S.; Alivisatos, A. P. Semiconductor Nanocrystals as Fluorescent Biological Labels. *science* **1998**, *281* (5385), 2013–2016.

- (39) Dannhauser, T.; O'neil, M.; Johansson, K.; Whitten, D.; McLendon, G. Photophysics of Quantized Colloidal Semiconductors. Dramatic Luminescence Enhancement by Binding of Simple Amines. *J. Phys. Chem.* **1986**, *90* (23), 6074–6076.
- (40) Peng, X.; Wei, Q.; Copple, A. Strain-Engineered Direct-Indirect Band Gap Transition and Its Mechanism in Two-Dimensional Phosphorene. *Phys. Rev. B* **2014**, *90* (8), 085402.
- (41) Tongay, S.; Zhou, J.; Ataca, C.; Lo, K.; Matthews, T. S.; Li, J.; Grossman, J. C.; Wu, J. Thermally Driven Crossover from Indirect toward Direct Bandgap in 2D Semiconductors: MoSe₂ versus MoS₂. *Nano Lett.* **2012**, *12* (11), 5576–5580.
- (42) Demchenko, D. O.; Tallapally, V.; Esteves, R. J. A.; Hafiz, S.; Nakagawara, T. A.; Arachchige, I. U.; Özgür, Ü. Optical Transitions and Excitonic Properties of Ge_{1-x}Sn_x Alloy Quantum Dots. *J. Phys. Chem. C* **2017**, *121* (33), 18299–18306.
- (43) Hafiz, S. A.; Esteves, R. J. A.; Demchenko, D. O.; Arachchige, I. U.; Özgür, Ü. Energy Gap Tuning and Carrier Dynamics in Colloidal Ge_{1-x}Sn_x Quantum Dots. *J. Phys. Chem. Lett.* **2016**, *7* (17), 3295–3301.
- (44) Graham, A. P.; Bertino, M. F.; Hofmann, F.; Toennies, J. P. Structure and Dynamics of C₂H₄ at Submonolayer Coverages on a Copper (001) Surface Studied by Helium Atom Scattering. *J. Phys. Chem.* **1996**, *100* (49), 19136–19140.
- (45) Khalid, F. A.; Bertino, M. F.; Khan, T. I. New Developments in Nanotechnology and Nanomaterials.
- (46) Butler, M. A. Photoelectrolysis and Physical Properties of the Semiconducting Electrode WO₂. *J. Appl. Phys.* **1977**, *48* (5), 1914–1920.
- (47) Jordan, A.; Scholz, R.; Maier-Hauff, K.; van Landeghem, F. K.; Waldoefner, N.; Teichgraeber, U.; Pinkernelle, J.; Bruhn, H.; Neumann, F.; Thiesen, B. The Effect of

- Thermotherapy Using Magnetic Nanoparticles on Rat Malignant Glioma. *J. Neurooncol.* **2006**, *78* (1), 7–14.
- (48) Maier-Hauff, K.; Ulrich, F.; Nestler, D.; Niehoff, H.; Wust, P.; Thiesen, B.; Orawa, H.; Budach, V.; Jordan, A. Efficacy and Safety of Intratumoral Thermotherapy Using Magnetic Iron-Oxide Nanoparticles Combined with External Beam Radiotherapy on Patients with Recurrent Glioblastoma Multiforme. *J. Neurooncol.* **2011**, *103* (2), 317–324.
- (49) Sawyer, C. A.; Habib, A. H.; Miller, K.; Collier, K. N.; Ondeck, C. L.; McHenry, M. E. Modeling of Temperature Profile during Magnetic Thermotherapy for Cancer Treatment. *J. Appl. Phys.* **2009**, *105* (7), 07B320.
- (50) Johannsen, M.; Gneveckow, U.; Thiesen, B.; Taymoorian, K.; Cho, C. H.; Waldöfner, N.; Scholz, R.; Jordan, A.; Loening, S. A.; Wust, P. Thermotherapy of Prostate Cancer Using Magnetic Nanoparticles: Feasibility, Imaging, and Three-Dimensional Temperature Distribution. *Eur. Urol.* **2007**, *52* (6), 1653–1662.
- (51) Jordan, A.; Maier-Hauff, K. Magnetic Nanoparticles for Intracranial Thermotherapy. *J. Nanosci. Nanotechnol.* **2007**, *7* (12), 4604–4606.
- (52) Maier, S. A.; Kik, P. G.; Atwater, H. A.; Meltzer, S.; Harel, E.; Koel, B. E.; Requicha, A. A. Local Detection of Electromagnetic Energy Transport below the Diffraction Limit in Metal Nanoparticle Plasmon Waveguides. *Nat. Mater.* **2003**, *2* (4), 229.
- (53) Peng, G.; Tisch, U.; Adams, O.; Hakim, M.; Shehada, N.; Broza, Y. Y.; Billan, S.; Abdah-Bortnyak, R.; Kuten, A.; Haick, H. Diagnosing Lung Cancer in Exhaled Breath Using Gold Nanoparticles. *Nat. Nanotechnol.* **2009**, *4* (10), 669.
- (54) Fang, C.; Agarwal, A.; Buddharaju, K. D.; Khalid, N. M.; Salim, S. M.; Widjaja, E.; Garland, M. V.; Balasubramanian, N.; Kwong, D.-L. DNA Detection Using

- Nanostructured SERS Substrates with Rhodamine B as Raman Label. *Biosens. Bioelectron.* **2008**, *24* (2), 216–221.
- (55) Guo, S.; Wang, E. Noble Metal Nanomaterials: Controllable Synthesis and Application in Fuel Cells and Analytical Sensors. *Nano Today* **2011**, *6* (3), 240–264.
- (56) McFarland, A. D.; Van Duyne, R. P. Single Silver Nanoparticles as Real-Time Optical Sensors with Zeptomole Sensitivity. *Nano Lett.* **2003**, *3* (8), 1057–1062.
- (57) Yuan, L.; Dai, J.; Fan, X.; Song, T.; Tao, Y. T.; Wang, K.; Xu, Z.; Zhang, J.; Bai, X.; Lu, P. Self-Cleaning Flexible Infrared Nanosensor Based on Carbon Nanoparticles. *ACS Nano* **2011**, *5* (5), 4007–4013.
- (58) Tam, J. M.; Murthy, A. K.; Ingram, D. R.; Nguyen, R.; Sokolov, K. V.; Johnston, K. P. Kinetic Assembly of Near-IR-Active Gold Nanoclusters Using Weakly Adsorbing Polymers to Control the Size. *Langmuir* **2010**, *26* (11), 8988–8999.
- (59) Sudarsan, V.; Van Veggel, F. C.; Herring, R. A.; Raudsepp, M. Surface Eu 3+ Ions Are Different than “Bulk” Eu 3+ Ions in Crystalline Doped LaF₃ Nanoparticles. *J. Mater. Chem.* **2005**, *15* (13), 1332–1342.
- (60) Sivakumar, S.; van Veggel, F. C. M.; Raudsepp, M. Bright White Light through Up-Conversion of a Single NIR Source from Sol–Gel-Derived Thin Film Made with Ln³⁺-Doped LaF₃ Nanoparticles. *J. Am. Chem. Soc.* **2005**, *127* (36), 12464–12465.
- (61) Watanabe, Y.; Bednorz, J.; Bietsch, A.; Gerber, C.; Widmer, D.; Beck, A.; Wind, S. J. Current-Driven Insulator–Conductor Transition and Nonvolatile Memory in Chromium-Doped SrTiO₃ Single Crystals. *Appl. Phys. Lett.* **2001**, *78* (23), 3738–3740.
- (62) Haddad, M. F.; Goiato, M. C.; dos Santos, D. M.; Moreno, A.; Pesqueira, A. A.; D'almeida, N. F. Color Stability of Maxillofacial Silicone with Nanoparticle Pigment and

- Opacifier Submitted to Disinfection and Artificial Aging. *J. Biomed. Opt.* **2011**, *16* (9), 095004.
- (63) Ogihara, H.; Okagaki, J.; Saji, T. Facile Fabrication of Colored Superhydrophobic Coatings by Spraying a Pigment Nanoparticle Suspension. *Langmuir* **2011**, *27* (15), 9069–9072.
- (64) Duncan, K. A.; Johnson, C.; McElhinny, K.; Ng, S.; Cadwell, K. D.; Zenner Petersen, G. M.; Johnson, A.; Horoszewski, D.; Gentry, K.; Lisensky, G. Art as an Avenue to Science Literacy: Teaching Nanotechnology through Stained Glass. *J. Chem. Educ.* **2010**, *87* (10), 1031–1038.
- (65) Jembrih-Simbürger, D.; Neelmeijer, C.; Schalm, O.; Fredrickx, P.; Schreiner, M.; De Vis, K.; Mäder, M.; Schryvers, D.; Caen, J. The Colour of Silver Stained Glass—Analytical Investigations Carried out with XRF, SEM/EDX, TEM, and IBA. *J. Anal. At. Spectrom.* **2002**, *17* (4), 321–328.
- (66) Hell, S. W.; Wichmann, J. Breaking the Diffraction Resolution Limit by Stimulated Emission: Stimulated-Emission-Depletion Fluorescence Microscopy. *Opt. Lett.* **1994**, *19* (11), 780–782.
- (67) Ghosh, S. K.; Nath, S.; Kundu, S.; Esumi, K.; Pal, T. Solvent and Ligand Effects on the Localized Surface Plasmon Resonance (LSPR) of Gold Colloids. *J. Phys. Chem. B* **2004**, *108* (37), 13963–13971.
- (68) Hao, F.; Sonnefraud, Y.; Dorpe, P. V.; Maier, S. A.; Halas, N. J.; Nordlander, P. Symmetry Breaking in Plasmonic Nanocavities: Subradiant LSPR Sensing and a Tunable Fano Resonance. *Nano Lett.* **2008**, *8* (11), 3983–3988.

- (69) Sepúlveda, B.; Angelomé, P. C.; Lechuga, L. M.; Liz-Marzán, L. M. LSPR-Based Nanobiosensors. *Nano Today* **2009**, *4* (3), 244–251.
- (70) Kneipp, K.; Kneipp, H.; Kartha, V. B.; Manoharan, R.; Deinum, G.; Itzkan, I.; Dasari, R. R.; Feld, M. S. Detection and Identification of a Single DNA Base Molecule Using Surface-Enhanced Raman Scattering (SERS). *Phys. Rev. E* **1998**, *57* (6), R6281.
- (71) Kudelski, A. Raman Studies of Rhodamine 6G and Crystal Violet Sub-Monolayers on Electrochemically Roughened Silver Substrates: Do Dye Molecules Adsorb Preferentially on Highly SERS-Active Sites? *Chem. Phys. Lett.* **2005**, *414* (4–6), 271–275.
- (72) Allen, W. A.; Richardson, A. J. Interaction of Light with a Plant Canopy. *JOSA* **1968**, *58* (8), 1023–1028.
- (73) El-Sayed, I. H.; Huang, X.; El-Sayed, M. A. Surface Plasmon Resonance Scattering and Absorption of Anti-EGFR Antibody Conjugated Gold Nanoparticles in Cancer Diagnostics: Applications in Oral Cancer. *Nano Lett.* **2005**, *5* (5), 829–834.
- (74) Bohren, C. F.; Huffman, D. R. *Absorption and Scattering of Light by Small Particles*; John Wiley & Sons, 2008.
- (75) Tuchin, V. V.; Utz, S. R.; Yaroslavsky, I. V. Tissue Optics, Light Distribution, and Spectroscopy. *Opt. Eng.* **1994**, *33* (10), 3178–3189.
- (76) Farrell, T. J.; Patterson, M. S.; Wilson, B. A Diffusion Theory Model of Spatially Resolved, Steady-state Diffuse Reflectance for the Noninvasive Determination of Tissue Optical Properties in Vivo. *Med. Phys.* **1992**, *19* (4), 879–888.
- (77) Rossel, R. V.; Walvoort, D. J. J.; McBratney, A. B.; Janik, L. J.; Skjemstad, J. O. Visible, near Infrared, Mid Infrared or Combined Diffuse Reflectance Spectroscopy for Simultaneous Assessment of Various Soil Properties. *Geoderma* **2006**, *131* (1–2), 59–75.

- (78) Henke, B. L.; Gullikson, E. M.; Davis, J. C. X-Ray Interactions: Photoabsorption, Scattering, Transmission, and Reflection at $E= 50\text{-}30,000$ EV, $Z= 1\text{-}92$. *At. Data Nucl. Data Tables* **1993**, *54* (2), 181–342.
- (79) KUCHII-SU, K.; FUKCWAMA, T.; Morino, Y. *NJ HARRICK, Internal Reflection Spectroscopy*, Interscience Publishers, London, 1967, Pp. Xiv+ 327. Price g 6.12 S.; 1967.
- (80) Thrane, L.; Jacobsen, R. H.; Jepsen, P. U.; Keiding, S. R. THz Reflection Spectroscopy of Liquid Water. *Chem. Phys. Lett.* **1995**, *240* (4), 330–333.
- (81) Wendlandt, W. W.; Hecht, H. G. *Reflectance Spectroscopy*; Interscience New York, 1966.
- (82) Haiss, W.; Thanh, N. T.; Aveyard, J.; Fernig, D. G. Determination of Size and Concentration of Gold Nanoparticles from UV– Vis Spectra. *Anal. Chem.* **2007**, *79* (11), 4215–4221.
- (83) Stejskal, J.; Kratochvil, P.; Radhakrishnan, N. Polyaniline Dispersions 2. UV—Vis Absorption Spectra. *Synth. Met.* **1993**, *61* (3), 225–231.
- (84) Belotelov, V. I.; Doskolovich, L. L.; Zvezdin, A. K. Extraordinary Magneto-Optical Effects and Transmission through Metal-Dielectric Plasmonic Systems. *Phys. Rev. Lett.* **2007**, *98* (7), 077401.
- (85) Knutson, H. A.; Dragomir, D.; Kreidberg, L.; Kempton, E. M.-R.; McCullough, P. R.; Fortney, J. J.; Bean, J. L.; Gillon, M.; Homeier, D.; Howard, A. W. Hubble Space Telescope Near-IR Transmission Spectroscopy of the Super-Earth HD 97658b. *Astrophys. J.* **2014**, *794* (2), 155.
- (86) Wong, S. W.; Kwon, M.-J.; Choi, A. M.; Kim, H.-P.; Nakahira, K.; Hwang, D. H. Fatty Acids Modulate Toll-like Receptor 4 Activation through Regulation of Receptor

- Dimerization and Recruitment into Lipid Rafts in a Reactive Oxygen Species-Dependent Manner. *J. Biol. Chem.* **2009**, *284* (40), 27384–27392.
- (87) Sherazi, S. T. H.; Ali, M.; Mahesar, S. A. Application of Fourier-Transform Infrared (FT-IR) Transmission Spectroscopy for the Estimation of Roxithromycin in Pharmaceutical Formulations. *Vib. Spectrosc.* **2011**, *55* (1), 115–118.
- (88) Stuart, B. *Infrared Spectroscopy*; Wiley Online Library, 2005.
- (89) Osawa, M.; Matsuda, N.; Yoshii, K.; Uchida, I. Charge Transfer Resonance Raman Process in Surface-Enhanced Raman Scattering from p-Aminothiophenol Adsorbed on Silver: Herzberg-Teller Contribution. *J. Phys. Chem.* **1994**, *98* (48), 12702–12707.
- (90) Kneipp, K.; Wang, Y.; Kneipp, H.; Perelman, L. T.; Itzkan, I.; Dasari, R. R.; Feld, M. S. Single Molecule Detection Using Surface-Enhanced Raman Scattering (SERS). *Phys. Rev. Lett.* **1997**, *78* (9), 1667.
- (91) Grochala, W.; Kudelski, A.; Bukowska, J. Anion-Induced Charge-Transfer Enhancement in and Spectra of on a SERS SERRS Rhodamine 6G Silver Electrode: How Important Is It? *J Raman Spectrosc* **1998**, *29*, 681–685.
- (92) Pristiniski, D.; Tan, S.; Erol, M.; Du, H.; Sukhishvili, S. In Situ SERS Study of Rhodamine 6G Adsorbed on Individually Immobilized Ag Nanoparticles. *J. Raman Spectrosc.* **2006**, *37* (7), 762–770.
- (93) Kneipp, K.; Kneipp, H.; Bohr, H. G. Single-Molecule SERS Spectroscopy. In *Surface-Enhanced Raman Scattering*; Springer, 2006; pp 261–277.
- (94) Bell, S. E.; Sirimuthu, N. M. Surface-Enhanced Raman Spectroscopy (SERS) for Sub-Micromolar Detection of DNA/RNA Mononucleotides. *J. Am. Chem. Soc.* **2006**, *128* (49), 15580–15581.

- (95) Chourpa, I.; Manfait, M. Specific Molecular Interactions of Acridine Drugs in Complexes with Topoisomerase II and DNA. SERS and Resonance Raman Study of M-AMSA in Comparison with O-AMSA. *J. Raman Spectrosc.* **1995**, *26* (8-9), 813–819.
- (96) Tian, S.; Neumann, O.; McClain, M. J.; Yang, X.; Zhou, L.; Zhang, C.; Nordlander, P.; Halas, N. J. Aluminum Nanocrystals: A Sustainable Substrate for Quantitative SERS-Based DNA Detection. *Nano Lett.* **2017**, *17* (8), 5071–5077.
- (97) Zhao, Y.; Liu, L.; Kuang, H.; Wang, L.; Xu, C. SERS-Active Ag@ Au Core–Shell NP Assemblies for DNA Detection. *Rsc Adv.* **2014**, *4* (99), 56052–56056.
- (98) Beljebbar, A.; Sockalingum, G. D.; Morjani, H.; Manfait, M. Raman and SERS Microspectroscopy on Living Cells: A Promising Tool toward Cellular Drug Response and Medical Diagnosis. In *Biomedical Applications of Raman Spectroscopy*; International Society for Optics and Photonics, 1999; Vol. 3608, pp 175–185.
- (99) Vo-Dinh, T.; Yan, F.; Wabuyele, M. B. Surface-enhanced Raman Scattering for Medical Diagnostics and Biological Imaging. *J. Raman Spectrosc.* **2005**, *36* (6-7), 640–647.
- (100) Hudson, S. D.; Chumanov, G. Bioanalytical Applications of SERS (Surface-Enhanced Raman Spectroscopy). *Anal. Bioanal. Chem.* **2009**, *394* (3), 679–686.
- (101) Chao, Y.; Zhang, T. Surface-Enhanced Raman Scattering (SERS) Revealing Chemical Variation during Biofilm Formation: From Initial Attachment to Mature Biofilm. *Anal. Bioanal. Chem.* **2012**, *404* (5), 1465–1475.
- (102) Gebremedhin, D.; Lange, A. R.; Narayanan, J.; Aebly, M. R.; Jacobs, E. R.; Harder, D. R. Cat Cerebral Arterial Smooth Muscle Cells Express Cytochrome P450 4A2 Enzyme and Produce the Vasoconstrictor 20-HETE Which Enhances L-type Ca²⁺ Current. *J. Physiol.* **1998**, *507* (3), 771–781.

- (103) Gurtner, G. H.; Knoblauch, A.; Smith, P. L.; Sies, H.; Adkinson, N. F. Oxidant-and Lipid-Induced Pulmonary Vasoconstriction Mediated by Arachidonic Acid Metabolites. *J. Appl. Physiol.* **1983**, *55* (3), 949–954.
- (104) Lasker, J. M.; Chen, W. B.; Wolf, I.; Blosswick, B. P.; Wilson, P. D.; Powell, P. K. Formation of 20-Hydroxyeicosatetraenoic Acid, a Vasoactive and Natriuretic Eicosanoid, in Human Kidney Role of Cyp4F2 and Cyp4A11. *J. Biol. Chem.* **2000**, *275* (6), 4118–4126.
- (105) Sakai, A.; Chang, S. W.; Voelkel, N. F. Importance of Vasoconstriction in Lipid Mediator-Induced Pulmonary Edema. *J. Appl. Physiol.* **1989**, *66* (6), 2667–2674.
- (106) Catella, F.; Lawson, J. A.; Fitzgerald, D. J.; FitzGerald, G. A. Endogenous Biosynthesis of Arachidonic Acid Epoxides in Humans: Increased Formation in Pregnancy-Induced Hypertension. *Proc. Natl. Acad. Sci.* **1990**, *87* (15), 5893–5897.
- (107) Dunn, K. M.; Renic, M.; Flasch, A. K.; Harder, D. R.; Falck, J.; Roman, R. J. Elevated Production of 20-HETE in the Cerebral Vasculature Contributes to Severity of Ischemic Stroke and Oxidative Stress in Spontaneously Hypertensive Rats. *Am. J. Physiol.-Heart Circ. Physiol.* **2008**, *295* (6), H2455–H2465.
- (108) Hoagland, K. M.; Flasch, A. K.; Roman, R. J. Inhibitors of 20-HETE Formation Promote Salt-Sensitive Hypertension in Rats. *Hypertension* **2003**, *42* (4), 669–673.
- (109) Makita, K.; Falck, J. R.; Capdevila, J. H. Cytochrome P450, the Arachidonic Acid Cascade, and Hypertension: New Vistas for an Old Enzyme System. *FASEB J.* **1996**, *10* (13), 1456–1463.
- (110) Mitka, M. Aggressive Lipid, Hypertension Targeting Yields No Benefit for Some with Diabetes. *JAMA* **2010**, *303* (17), 1681–1683.

- (111) Sjöström, C. D.; Lissner, L.; Wedel, H.; Sjöström, L. Reduction in Incidence of Diabetes, Hypertension and Lipid Disturbances after Intentional Weight Loss Induced by Bariatric Surgery: The SOS Intervention Study. *Obesity* **1999**, 7 (5), 477–484.
- (112) Ward, N. C.; Tsai, I.-J.; Barden, A.; van Bockxmeer, F. M.; Puddey, I. B.; Hodgson, J. M.; Croft, K. D. A Single Nucleotide Polymorphism in the CYP4F2 but Not CYP4A11 Gene Is Associated with Increased 20-HETE Excretion and Blood Pressure. *Hypertension* **2008**, 51 (5), 1393–1398.
- (113) Williams, J. M.; Murphy, S.; Burke, M.; Roman, R. J. 20-HETE: A New Target for the Treatment of Hypertension. *J. Cardiovasc. Pharmacol.* **2010**, 56 (4), 336.
- (114) Redman, C. W.; Sargent, I. L. Latest Advances in Understanding Preeclampsia. *Science* **2005**, 308 (5728), 1592–1594.
- (115) Nzelu, D.; Dumitrascu-Biris, D.; Hunt, K. F.; Cordina, M.; Kametas, N. A. Pregnancy Outcomes in Women with Previous Gestational Hypertension: A Cohort Study to Guide Counselling and Management. *Pregnancy Hypertens.* **2017**.
- (116) Porreco, R. P.; Heyborne, K. D. Immunogenesis of Preeclampsia: Lessons from Donor Gametes. *J. Matern. Fetal Neonatal Med.* **2018**, 31 (9), 1220–1226.
- (117) Thathagari, V.; Kumar, V. Evaluation of Serum Lipids in Preeclampsia: A Comparative Study. *Int. J. Reprod. Contracept. Obstet. Gynecol.* **2018**, 7 (4), 1372–1375.
- (118) Mayoral-Andrade, G.; Pérez-Campos-Mayoral, L.; Majluf-Cruz, A.; Perez-Campos Mayoral, E.; Perezcampos Mayoral, C.; Rocha-Núñez, A.; Martinez, M.; Zenteno, E.; Hernandez-Gonzalez, L.; Juan, L. Reduced Platelet Aggregation in Women after Intercourse: A Possible Role for the Cyclooxygenase Pathway. *Clin. Exp. Pharmacol. Physiol.* **2017**.

- (119) Panzenbeck, M. J.; Hintze, T. H.; Kaley, G. 6-Keto-Prostaglandin E1 Is a Potent Coronary Vasodilator and Stimulates a Vagal Reflex in Dogs. *J. Pharmacol. Exp. Ther.* **1988**, *244* (3), 814–819.
- (120) Rosolowsky, M.; Campbell, W. B. Role of PGI₂ and Epoxyeicosatrienoic Acids in Relaxation of Bovine Coronary Arteries to Arachidonic Acid. *Am. J. Physiol.-Heart Circ. Physiol.* **1993**, *264* (2), H327–H335.
- (121) Robertson, S. A.; Mau, V. J.; Tremellen, K. P.; Seamark, R. F. Role of High Molecular Weight Seminal Vesicle Proteins in Eliciting the Uterine Inflammatory Response to Semen in Mice. *J. Reprod. Fertil.* **1996**, *107* (2), 265–277.
- (122) Kurzrok, R.; Lieb, C. C. Biochemical Studies of Human Semen. II. The Action of Semen on the Human Uterus. *Proc. Soc. Exp. Biol. Med.* **1930**, *28* (3), 268–272.
- (123) Pandya, I. J.; Cohen, J. The Leukocytic Reaction of the Human Uterine Cervix to Spermatozoa. *Fertil. Steril.* **1985**, *43* (3), 417–421.
- (124) Kotilainen, T.; Huhtinen, M.; Katila, T. Sperm-Induced Leukocytosis in the Equine Uterus. *Theriogenology* **1994**, *41* (3), 629–636.
- (125) Thompson, L. A.; Barratt, C. L. R.; Bolton, A. E.; Cooke, I. D. The Leukocytic Reaction of the Human Uterine Cervix. *Am. J. Reprod. Immunol.* **1992**, *28* (2), 85–89.
- (126) Woelkers, D.; Barton, J.; von Dadelszen, P.; Sibai, B. [71-OR]: The Revised 2013 ACOG Definitions of Hypertensive Disorders of Pregnancy Significantly Increase the Diagnostic Prevalence of Preeclampsia. *Pregnancy Hypertens. Int. J. Womens Cardiovasc. Health* **2015**, *5* (1), 38.

- (127) Murphy, S.; Lee, N.; Faulkner, J.; Spencer, S.-K.; Wallace, K.; LaMarca, B. 20-HETE Impedes Trophoblast Migration and Contributes to Hypertension in the RUPP Rat Model of Placental Ischemia. *FASEB J.* **2017**, *31* (1 Supplement), 1033.6-1033.6.
- (128) Cotton, J.; Wu, W.; Murphy, S. Increases in Cytochrome P450 Expression and 20-HETE Production Reduce Mean Arterial Pressure in an Animal Model of Preeclampsia. *FASEB J.* **2017**, *31* (1 Supplement), 692.1-692.1.
- (129) Czamara, K.; Majzner, K.; Pacia, M. Z.; Kochan, K.; Kaczor, A.; Baranska, M. Raman Spectroscopy of Lipids: A Review. *J. Raman Spectrosc.* **2015**, *46* (1), 4–20.
- (130) Kundu, J.; Levin, C. S.; Halas, N. J. Real-Time Monitoring of Lipid Transfer between Vesicles and Hybrid Bilayers on Au Nanoshells Using Surface Enhanced Raman Scattering (SERS). *Nanoscale* **2009**, *1* (1), 114–117.
- (131) Severcan, F.; Gorgulu, G.; Gorgulu, S. T.; Guray, T. Rapid Monitoring of Diabetes-Induced Lipid Peroxidation by Fourier Transform Infrared Spectroscopy: Evidence from Rat Liver Microsomal Membranes. *Anal. Biochem.* **2005**, *339* (1), 36–40.
- (132) Dersch, H.; Stuke, J.; Beichler, J. Light-induced Dangling Bonds in Hydrogenated Amorphous Silicon. *Appl. Phys. Lett.* **1981**, *38* (6), 456–458.
- (133) Lawson, A.; Ellis, C.; Tischler, J.; Rabin, O. Infrared Resonances in Plasmonic Nanorod and Nanoarc Antennas. In *APS Meeting Abstracts*; 2016.
- (134) Berry, E.; John, R.; Tang, S.; Guo, A. M. Role of Inflammation in 20-HETE Regulation of Ischemia-Induced Angiogenesis. **2017**.
- (135) Seelig, J.; Nebel, S.; Ganz, P.; Bruns, C. Electrostatic and Nonpolar Peptide-Membrane Interactions. Lipid Binding and Functional Properties of Somatostatin Analogs of Charge $Z=+1$ to $Z=+3$. *Biochemistry (Mosc.)* **1993**, *32* (37), 9714–9721.

- (136) Rowe, E. S. Lipid Chain Length and Temperature Dependence of Ethanol-Phosphatidylcholine Interactions. *Biochemistry (Mosc.)* **1983**, 22 (14), 3299–3305.
- (137) Balasubramanian, S. V.; Straubinger, R. M. Taxol-Lipid Interactions: Taxol-Dependent Effects on the Physical Properties of Model Membranes. *Biochemistry (Mosc.)* **1994**, 33 (30), 8941–8947.
- (138) Mazer, N. A.; Benedek, G. B.; Carey, M. C. Quasielastic Light-Scattering Studies of Aqueous Biliary Lipid Systems. Mixed Micelle Formation in Bile Salt-Lecithin Solutions. *Biochemistry (Mosc.)* **1980**, 19 (4), 601–615.
- (139) Jiang, J.; Tong, X.; Zhao, Y. A New Design for Light-Breakable Polymer Micelles. *J. Am. Chem. Soc.* **2005**, 127 (23), 8290–8291.
- (140) Grebe, S. K.; Singh, R. J. LC-MS/MS in the Clinical Laboratory—Where to from Here? *Clin. Biochem. Rev.* **2011**, 32 (1), 5.
- (141) Krone, N.; Hughes, B. A.; Lavery, G. G.; Stewart, P. M.; Arlt, W.; Shackleton, C. H. Gas Chromatography/Mass Spectrometry (GC/MS) Remains a Pre-Eminent Discovery Tool in Clinical Steroid Investigations Even in the Era of Fast Liquid Chromatography Tandem Mass Spectrometry (LC/MS/MS). *J. Steroid Biochem. Mol. Biol.* **2010**, 121 (3–5), 496–504.
- (142) Snyder, L. R.; Kirkland, J. J.; Dolan, J. W. *Introduction to Modern Liquid Chromatography*; John Wiley & Sons, 2011.
- (143) MESBAH, M.; PREMACHANDRAN, U.; WHITMAN, W. B. Precise Measurement of the G+ C Content of Deoxyribonucleic Acid by High-Performance Liquid Chromatography. *Int. J. Syst. Evol. Microbiol.* **1989**, 39 (2), 159–167.

- (144) Tanaka, N.; Kobayashi, H.; Nakanishi, K.; Minakuchi, H.; Ishizuka, N. *Peer Reviewed: Monolithic LC Columns*; ACS Publications, 2001.
- (145) Cole, R. B. *Electrospray Ionization Mass Spectrometry: Fundamentals, Instrumentation, and Applications*; 1997.
- (146) Fenn, J. B.; Mann, M.; Meng, C. K.; Wong, S. F.; Whitehouse, C. M. Electrospray Ionization for Mass Spectrometry of Large Biomolecules. *Science* **1989**, *246* (4926), 64–71.
- (147) Takats, Z.; Wiseman, J. M.; Gologan, B.; Cooks, R. G. Mass Spectrometry Sampling under Ambient Conditions with Desorption Electrospray Ionization. *Science* **2004**, *306* (5695), 471–473.
- (148) Cohen, A. S.; Waters, F. G. Separation of Osmium from Geological Materials by Solvent Extraction for Analysis by Thermal Ionisation Mass Spectrometry. *Anal. Chim. Acta* **1996**, *332* (2–3), 269–275.
- (149) Swortwood, M. J.; Boland, D. M.; DeCaprio, A. P. Determination of 32 Cathinone Derivatives and Other Designer Drugs in Serum by Comprehensive LC-QQQ-MS/MS Analysis. *Anal. Bioanal. Chem.* **2013**, *405* (4), 1383–1397.
- (150) Dang, L.; White, D. W.; Gross, S.; Bennett, B. D.; Bittinger, M. A.; Driggers, E. M.; Fantin, V. R.; Jang, H. G.; Jin, S.; Keenan, M. C. Cancer-Associated IDH1 Mutations Produce 2-Hydroxyglutarate. *Nature* **2009**, *462* (7274), 739.
- (151) Fiehn, O.; Kopka, J.; Trethewey, R. N.; Willmitzer, L. Identification of Uncommon Plant Metabolites Based on Calculation of Elemental Compositions Using Gas Chromatography and Quadrupole Mass Spectrometry. *Anal. Chem.* **2000**, *72* (15), 3573–3580.

- (152) Morris, H. R.; Paxton, T.; Dell, A.; Langhorne, J.; Berg, M.; Bordoli, R. S.; Hoyes, J.; Bateman, R. H. High Sensitivity Collisionally-activated Decomposition Tandem Mass Spectrometry on a Novel Quadrupole/Orthogonal-acceleration Time-of-flight Mass Spectrometer. *Rapid Commun. Mass Spectrom.* **1996**, *10* (8), 889–896.
- (153) Yost, R. A.; Enke, C. G. Triple Quadrupole Mass Spectrometry for Direct Mixture Analysis and Structure Elucidation. *Anal. Chem.* **1979**, *51* (12), 1251–1264.
- (154) Mirnaghi, F. S.; Pawliszyn, J. Reusable Solid-Phase Microextraction Coating for Direct Immersion Whole-Blood Analysis and Extracted Blood Spot Sampling Coupled with Liquid Chromatography–Tandem Mass Spectrometry and Direct Analysis in Real Time–Tandem Mass Spectrometry. *Anal. Chem.* **2012**, *84* (19), 8301–8309.
- (155) Partridge, S. M. Filter-Paper Partition Chromatography of Sugars: 1. General Description and Application to the Qualitative Analysis of Sugars in Apple Juice, Egg White and Foetal Blood of Sheep. with a Note by RG Westall. *Biochem. J.* **1948**, *42* (2), 238.
- (156) Jones, C. M.; Bernier, M.; Carson, E.; Colyer, K. E.; Metz, R.; Pawlow, A.; Wischow, E. D.; Webb, I.; Andriole, E. J.; Poutsma, J. C. Gas-Phase Acidities of the 20 Protein Amino Acids. *Int. J. Mass Spectrom.* **2007**, *267* (1–3), 54–62.
- (157) Yoon, S. H.; Chamot-Rooke, J.; Perkins, B. R.; Hilderbrand, A. E.; Poutsma, J. C.; Wysocki, V. H. IRMPD Spectroscopy Shows That AGG Forms an Oxazolone B₂⁺ Ion. *J. Am. Chem. Soc.* **2008**, *130* (52), 17644–17645.
- (158) Nakamura, T.; Bratton, D. L.; Murphy, R. C. Analysis of Epoxyeicosatrienoic and Monohydroxyeicosatetraenoic Acids Esterified to Phospholipids in Human Red Blood Cells by Electrospray Tandem Mass Spectrometry. *J. Mass Spectrom.* **1997**, *32* (8), 888–896.

- (159) Wong, S. F.; Meng, C. K.; Fenn, J. B. Multiple Charging in Electrospray Ionization of Poly (Ethylene Glycols). *J. Phys. Chem.* **1988**, *92* (2), 546–550.
- (160) Petrović, M.; Hernando, M. D.; Díaz-Cruz, M. S.; Barceló, D. Liquid Chromatography–Tandem Mass Spectrometry for the Analysis of Pharmaceutical Residues in Environmental Samples: A Review. *J. Chromatogr. A* **2005**, *1067* (1–2), 1–14.
- (161) Sommer, U.; Herscovitz, H.; Welty, F. K.; Costello, C. E. LC-MS-Based Method for the Qualitative and Quantitative Analysis of Complex Lipid Mixtures. *J. Lipid Res.* **2006**, *47* (4), 804–814.
- (162) Lanza, I. R.; Zhang, S.; Ward, L. E.; Karakelides, H.; Raftery, D.; Nair, K. S. Quantitative Metabolomics by ¹H-NMR and LC-MS/MS Confirms Altered Metabolic Pathways in Diabetes. *PloS One* **2010**, *5* (5), e10538.
- (163) Baggari, I. E.; Savitzky, B. H.; Admasu, A. S.; Kim, J.; Cheong, S.-W.; Hovden, R.; Kourkoutis, L. F. Commensurate Stripes and Phase Coherence in Manganites Revealed with Cryogenic Scanning Transmission Electron Microscopy. *ArXiv Prepr. ArXiv170808871* **2017**.
- (164) Kondo, T.; Chen, W. J.; Schlau-Cohen, G. S. Single-Molecule Fluorescence Spectroscopy of Photosynthetic Systems. *Chem. Rev.* **2017**, *117* (2), 860–898.
- (165) Breadmore, M. C.; Wuethrich, A.; Li, F.; Phung, S. C.; Kalsoom, U.; Cabot, J. M.; Tehranirokh, M.; Shallan, A. I.; Abdul Keyon, A. S.; See, H. H. Recent Advances in Enhancing the Sensitivity of Electrophoresis and Electrochromatography in Capillaries and Microchips (2014–2016). *Electrophoresis* **2017**, *38* (1), 33–59.

- (166) Mukanova, Z.; Gudun, K.; Elemessova, Z.; Khamkhash, L.; Ralchenko, E.; Bukasov, R. Detection of Paracetamol in Water and Urea in Artificial Urine with Gold Nanoparticle@Al Foil Cost-Efficient SERS Substrate. *Anal. Sci.* **2018**, *34* (2), 183–187.
- (167) Aherne, D.; Ledwith, D. M.; Gara, M.; Kelly, J. M. Optical Properties and Growth Aspects of Silver Nanoplatelets Produced by a Highly Reproducible and Rapid Synthesis at Room Temperature. *Adv. Funct. Mater.* **2008**, *18* (14), 2005–2016.
- (168) Crozier, K. B.; Sundaramurthy, A.; Kino, G. S.; Quate, C. F. Optical Antennas: Resonators for Local Field Enhancement. *J. Appl. Phys.* **2003**, *94* (7), 4632–4642.
- (169) Stipe, B. C.; Strand, T. C.; Poon, C. C.; Balamane, H.; Boone, T. D.; Katine, J. A.; Li, J.-L.; Rawat, V.; Nemoto, H.; Hirotsume, A. Magnetic Recording at 1.5 Pb M⁻² Using an Integrated Plasmonic Antenna. *Nat. Photonics* **2010**, *4* (7), 484.
- (170) Yaseen, T.; Pu, H.; Sun, D.-W. Functionalization Techniques for Improving SERS Substrates and Their Applications in Food Safety Evaluation: A Review of Recent Research Trends. *Trends Food Sci. Technol.* **2018**.
- (171) Armas, L. E. G.; Menezes, J. W.; Huila, M. G.; Araki, K.; Toma, H. E. Gold Nanohole Arrays Fabricated by Interference Lithography Technique as SERS Probes for Chemical Species Such As Rhodamine 6G and 4, 4'-Bipyridine. *Plasmonics* **2017**, *12* (4), 1015–1020.
- (172) Zhao, X.; Wen, J.; Zhang, M.; Wang, D.; Wang, Y.; Chen, L.; Zhang, Y.; Yang, J.; Du, Y. Design of Hybrid Nanostructural Arrays to Manipulate SERS-Active Substrates by Nanosphere Lithography. *ACS Appl. Mater. Interfaces* **2017**, *9* (8), 7710–7716.

- (173) Siddique, R. H.; Mertens, J.; Hölscher, H.; Vignolini, S. Scalable and Controlled Self-Assembly of Aluminum-Based Random Plasmonic Metasurfaces. *Light Sci. Appl.* **2017**, *6* (7), e17015.
- (174) Perez, N. P.; Alvarez-Puebla, R. Fabrication of Continuous and Isolated 3D Plasmonic Micro-Structured Super-Crystals Arrays for SERS Sensing (Conference Presentation). In *Colloidal Nanoparticles for Biomedical Applications XIII*; International Society for Optics and Photonics, 2018; Vol. 10507, p 105070L.
- (175) Canamares, M. V.; Chenal, C.; Birke, R. L.; Lombardi, J. R. DFT, SERS, and Single-Molecule SERS of Crystal Violet. *J. Phys. Chem. C* **2008**, *112* (51), 20295–20300.
- (176) Milliken, S.; Fraser, J.; Poirier, S.; Hulse, J.; Tay, L.-L. Self-Assembled Vertically Aligned Au Nanorod Arrays for Surface-Enhanced Raman Scattering (SERS) Detection of Cannabinol. *Spectrochim. Acta. A. Mol. Biomol. Spectrosc.* **2018**.
- (177) Kovacs, G. J.; Loutfy, R. O.; Vincett, P. S.; Jennings, C.; Aroca, R. Distance Dependence of SERS Enhancement Factor from Langmuir-Blodgett Monolayers on Metal Island Films: Evidence for the Electromagnetic Mechanism. *Langmuir* **1986**, *2* (6), 689–694.
- (178) Raman, C. V. A New Radiation. **1928**.
- (179) Efremov, E. V.; Ariese, F.; Gooijer, C. Achievements in Resonance Raman Spectroscopy: Review of a Technique with a Distinct Analytical Chemistry Potential. *Anal. Chim. Acta* **2008**, *606* (2), 119–134.
- (180) Clays, K.; Persoons, A. Hyper-Rayleigh Scattering in Solution. *Phys. Rev. Lett.* **1991**, *66* (23), 2980.

- (181) Inouye, S.; Chikkatur, A. P.; Stamper-Kurn, D. M.; Stenger, J.; Pritchard, D. E.; Ketterle, W. Superradiant Rayleigh Scattering from a Bose-Einstein Condensate. *Science* **1999**, 285 (5427), 571–574.
- (182) Kneipp, K.; Kneipp, H.; Corio, P.; Brown, S. D. M.; Shafer, K.; Motz, J.; Perelman, L. T.; Hanlon, E. B.; Marucci, A.; Dresselhaus, G. Surface-Enhanced and Normal Stokes and Anti-Stokes Raman Spectroscopy of Single-Walled Carbon Nanotubes. *Phys. Rev. Lett.* **2000**, 84 (15), 3470.
- (183) Hellerer, T.; Axäng, C.; Brackmann, C.; Hillertz, P.; Pilon, M.; Enejder, A. Monitoring of Lipid Storage in *Caenorhabditis Elegans* Using Coherent Anti-Stokes Raman Scattering (CARS) Microscopy. *Proc. Natl. Acad. Sci.* **2007**, 104 (37), 14658–14663.
- (184) Kneipp, K.; Wang, Y.; Kneipp, H.; Itzkan, I.; Dasari, R. R.; Feld, M. S. Population Pumping of Excited Vibrational States by Spontaneous Surface-Enhanced Raman Scattering. *Phys. Rev. Lett.* **1996**, 76 (14), 2444.
- (185) Haynes, C. L.; McFarland, A. D.; Duyne, R. P. V. *Surface-Enhanced Raman Spectroscopy*; ACS Publications, 2005.
- (186) Flegler, Y.; Nagli, L.; Gaft, M.; Rosenbluh, M. Narrow Gated Raman and Luminescence of Explosives. *J. Lumin.* **2009**, 129 (9), 979–983.
- (187) Garrell, R. L. Surface-Enhanced Raman Spectroscopy. *Anal. Chem.* **1989**, 61 (6), 401A-411A.
- (188) Nie, S.; Emory, S. R. Probing Single Molecules and Single Nanoparticles by Surface-Enhanced Raman Scattering. *science* **1997**, 275 (5303), 1102–1106.
- (189) Willets, K. A.; Van Duyne, R. P. Localized Surface Plasmon Resonance Spectroscopy and Sensing. *Annu Rev Phys Chem* **2007**, 58, 267–297.

- (190) Sherry, L. J.; Chang, S.-H.; Schatz, G. C.; Van Duyne, R. P.; Wiley, B. J.; Xia, Y. Localized Surface Plasmon Resonance Spectroscopy of Single Silver Nanocubes. *Nano Lett.* **2005**, *5* (10), 2034–2038.
- (191) Brown, A. M.; Sundararaman, R.; Narang, P.; Goddard III, W. A.; Atwater, H. A. Ab Initio Phonon Coupling and Optical Response of Hot Electrons in Plasmonic Metals. *Phys. Rev. B* **2016**, *94* (7), 075120.
- (192) Gérard, D.; Wenger, J.; Bonod, N.; Popov, E.; Rigneault, H.; Mahdavi, F.; Blair, S.; Dintinger, J.; Ebbesen, T. W. Nanoaperture-Enhanced Fluorescence: Towards Higher Detection Rates with Plasmonic Metals. *Phys. Rev. B* **2008**, *77* (4), 045413.
- (193) Zeman, E. J.; Schatz, G. C. An Accurate Electromagnetic Theory Study of Surface Enhancement Factors for Silver, Gold, Copper, Lithium, Sodium, Aluminum, Gallium, Indium, Zinc, and Cadmium. *J. Phys. Chem.* **1987**, *91* (3), 634–643.
- (194) Wu, D.-Y.; Liu, X.-M.; Duan, S.; Xu, X.; Ren, B.; Lin, S.-H.; Tian, Z.-Q. Chemical Enhancement Effects in SERS Spectra: A Quantum Chemical Study of Pyridine Interacting with Copper, Silver, Gold and Platinum Metals. *J. Phys. Chem. C* **2008**, *112* (11), 4195–4204.
- (195) Krause, D.; Teplin, C. W.; Rogers, C. T. Optical Surface Second Harmonic Measurements of Isotropic Thin-Film Metals: Gold, Silver, Copper, Aluminum, and Tantalum. *J. Appl. Phys.* **2004**, *96* (7), 3626–3634.
- (196) Luechinger, N. A.; Athanassiou, E. K.; Stark, W. J. Graphene-Stabilized Copper Nanoparticles as an Air-Stable Substitute for Silver and Gold in Low-Cost Ink-Jet Printable Electronics. *Nanotechnology* **2008**, *19* (44), 445201.

- (197) Nagpal, P.; Lindquist, N. C.; Oh, S.-H.; Norris, D. J. Ultrasmooth Patterned Metals for Plasmonics and Metamaterials. *Science* **2009**, *325* (5940), 594–597.
- (198) Haynes, C. L.; Van Duyne, R. P. Plasmon-Sampled Surface-Enhanced Raman Excitation Spectroscopy. *J. Phys. Chem. B* **2003**, *107* (30), 7426–7433.
- (199) Radziuk, D.; Moehwald, H. Prospects for Plasmonic Hot Spots in Single Molecule SERS towards the Chemical Imaging of Live Cells. *Phys. Chem. Chem. Phys.* **2015**, *17* (33), 21072–21093.
- (200) Alonso-González, P.; Albella, P.; Schnell, M.; Chen, J.; Huth, F.; García-Etxarri, A.; Casanova, F.; Golmar, F.; Arzubiaga, L.; Hueso, L. E. Resolving the Electromagnetic Mechanism of Surface-Enhanced Light Scattering at Single Hot Spots. *Nat. Commun.* **2012**, *3*, 684.
- (201) Harutyunyan, H.; Martinson, A. B.; Rosenmann, D.; Khorashad, L. K.; Besteiro, L. V.; Govorov, A. O.; Wiederrecht, G. P. Anomalous Ultrafast Dynamics of Hot Plasmonic Electrons in Nanostructures with Hot Spots. *Nat. Nanotechnol.* **2015**, *10* (9), 770.
- (202) Lahiri, B.; Holland, G.; Aksyuk, V.; Centrone, A. Nanoscale Imaging of Plasmonic Hot Spots and Dark Modes with the Photothermal-Induced Resonance Technique. *Nano Lett.* **2013**, *13* (7), 3218–3224.
- (203) Lombardi, J. R.; Birke, R. L. A Unified Approach to Surface-Enhanced Raman Spectroscopy. *J. Phys. Chem. C* **2008**, *112* (14), 5605–5617.
- (204) Kambhampati, P.; Campion, A. Surface Enhanced Raman Scattering as a Probe of Adsorbate–Substrate Charge-Transfer Excitations. *Surf. Sci.* **1999**, *427*, 115–125.

- (205) Lombardi, J. R.; Birke, R. L.; Lu, T.; Xu, J. Charge-transfer Theory of Surface Enhanced Raman Spectroscopy: Herzberg–Teller Contributions. *J. Chem. Phys.* **1986**, *84* (8), 4174–4180.
- (206) Perkampus, H.-H. *UV-VIS Spectroscopy and Its Applications*; Springer Science & Business Media, 2013.
- (207) Ohlhaver, C.; Bertino, M.; Rutan, S.; Wijesinghe, D.; Arachchige, I. U. Applications of Surface Enhanced Raman Scattering Towards the Detection of the Bioactive Lipid: 20-HETE. *ACS Appl. Nanomater.* **2018**, *1* (7).
- (208) Gate, L. F. Comparison of the Photon Diffusion Model and Kubelka-Munk Equation with the Exact Solution of the Radiative Transport Equation. *Appl. Opt.* **1974**, *13* (2), 236–238.
- (209) Xu, G.; Tazawa, M.; Jin, P.; Nakao, S.; Yoshimura, K. Wavelength Tuning of Surface Plasmon Resonance Using Dielectric Layers on Silver Island Films. *Appl. Phys. Lett.* **2003**, *82* (22), 3811–3813.
- (210) Mock, J. J.; Barbic, M.; Smith, D. R.; Schultz, D. A.; Schultz, S. Shape Effects in Plasmon Resonance of Individual Colloidal Silver Nanoparticles. *J. Chem. Phys.* **2002**, *116* (15), 6755–6759.
- (211) Evanoff, D. D.; Chumanov, G. Size-Controlled Synthesis of Nanoparticles. 2. Measurement of Extinction, Scattering, and Absorption Cross Sections. *J. Phys. Chem. B* **2004**, *108* (37), 13957–13962.
- (212) Tejamaya, M.; Römer, I.; Merrifield, R. C.; Lead, J. R. Stability of Citrate, PVP, and PEG Coated Silver Nanoparticles in Ecotoxicology Media. *Environ. Sci. Technol.* **2012**, *46* (13), 7011–7017.

- (213) Minnikin, D. E.; Collins, M. D.; Goodfellow, M. Fatty Acid and Polar Lipid Composition in the Classification of Cellulomonas, Oerskovia and Related Taxa. *J. Appl. Microbiol.* **1979**, *47* (1), 87–95.
- (214) Kerker, M.; Wang, D.-S.; Chew, H. Surface Enhanced Raman Scattering (SERS) by Molecules Adsorbed at Spherical Particles: Errata. *Appl. Opt.* **1980**, *19* (24), 4159–4174.
- (215) Aroca, R. *Surface-Enhanced Vibrational Spectroscopy*; John Wiley & Sons, 2006.
- (216) Champion, A.; Kambhampati, P. Surface-Enhanced Raman Scattering. *Chem. Soc. Rev.* **1998**, *27* (4), 241–250.
- (217) Mueller, N. S.; Heeg, S.; Kusch, P.; Gaufrès, E.; Tang, N. Y.-W.; Hübner, U.; Martel, R.; Vijayaraghavan, A.; Reich, S. Plasmonic Enhancement of SERS Measured on Molecules in Carbon Nanotubes. *Faraday Discuss.* **2017**, *205*, 85–103.
- (218) Arenas, J. F.; Woolley, M. S.; Otero, J. C.; Marcos, J. I. Charge-Transfer Processes in Surface-Enhanced Raman Scattering. Franck–Condon Active Vibrations of Pyrazine. *J. Phys. Chem.* **1996**, *100* (8), 3199–3206.
- (219) Keller, C.; Stichler, M.; Comelli, G.; Esch, F.; Lizzit, S.; Wurth, W.; Menzel, D. Ultrafast Charge Transfer Times of Chemisorbed Species from Auger Resonant Raman Studies. *Phys. Rev. Lett.* **1998**, *80* (8), 1774.
- (220) Bala, T.; Prasad, B. L. V.; Sastry, M.; Kahaly, M. U.; Waghmare, U. V. Interaction of Different Metal Ions with Carboxylic Acid Group: A Quantitative Study. *J. Phys. Chem. A* **2007**, *111* (28), 6183–6190.
- (221) Human Metabolome Database. Canadian Institutes of Health Research.

Christopher M. Ohlhaber

Email: ohlhabercm@mymail.vcu.edu

EDUCATION

- Master of Science in Chemistry, May 2017 (expected)
Virginia Commonwealth University, Richmond, VA
Thesis: Applications of Surface Enhanced Raman Scattering Towards the Detection of the Bioactive Lipid: 20-HETE
Advisor: Dr. Indika U. Arachchige
- B. S. in Chemistry
College of William and Mary, Williamsburg, VA
Research: Crystallography of Cu(I)-pyridine complexes
Advisor: Dr. Robert D. Pike

RESEARCH EXPERIENCE

2017-2018 Graduate Research Assistant, Virginia Commonwealth University

- Designed and developed a substrate for Surface Enhanced Raman Spectroscopy
- Applied SERS toward the detection of bioactive lipids
- Investigated silicon-tin quantum dots
- Investigated germanium quantum dots

2015-2017 Undergraduate Researcher at the College of William and Mary

- Investigated the crystallographic structure of copper (I) pyridine complexes

TECHNICAL EXPERTISE

Spectroscopy and Microscopy

- Surface Enhanced Raman Spectroscopy (SERS)
- Raman Spectroscopy
- Single Crystal X-ray Diffraction
- Powder X-ray Diffraction (PXRD)
- Energy Dispersive Spectroscopy (EDS)
- Diffuse Reflectance Spectroscopy (DRA)
- Nuclear Magnetic Resonance (NMR)
- Fourier Transform Infrared Spectroscopy (FTIR)
- Attenuated Total Reflectance Fourier Transform Infrared Spectroscopy (ATR-FTIR)
- Near Infrared, Ultraviolet, Visible Spectroscopy (NIR-UV-Vis Spectroscopy)
- Transmission Electron Spectroscopy (TEM)
- Scanning Electron Microscopy (SEM)
- Gas Chromatography Mass Spectroscopy (GC-MS)

Data Analysis

- Origin Lab, Microsoft Excel, ChemBio Draw 17, LabSpec 4.0, LabSpec 5.0

PEER REVIEWED JOURNAL ARTICLE

Ohlhaber, C.; Bertino, M.; Rutan, S.; Wijesinghe, D.; Arachchige, I. U. Applications of Surface Enhanced Raman Scattering Towards the Detection of the Bioactive Lipid: 20-HETE. *ACS Appl. Nanomater.* **2018**, *1* (7). DOI: 10.1021/acsanm.8b00840.

FUTURE PLANS

Starting in August 2018, I will be interested a Ph. D. Program in Materials Science and Engineering at the University of Maryland in College Park Maryland, studying under the tutelage of Dr. Oded Rabin.